A Study of Lead Tungstate Crystals and Improvement of Radiation Hardness

Thesis by

Qu, Xiangdong

for the Degree of
Doctor of Philosophy

Shanghai Institute of Ceramics
The Chinese Academy of Sciences
Shanghai, China

January 16, 2001

Acknowledgment

This work has its roots in the teaching, help, patience, and inspiration of a number of people, to whom I wish to express my heartfelt gratitude.

I would like to thank my adviser Prof. Yin Zhiwen at Shanghai Institute of Ceramics. I am delighted to have Prof. Yin Zhiwen as my adviser. Prof. Yin Zhiwen is the reason I have studied inorganic scintillator, the reason I embarked on this study.

My heartfelt thanks to Dr. Zhu Ren-yuan, for his detailed, insightful comments and directions on nearly every step of my work at California Institute of Technology. Dr. Zhu Ren-yuan is the reason I had faith that the work would, with sufficient diligence, yield a host of new insights. I am delighted that, from him I learned a lot and still find he has much more to teach me.

Special thanks to Prof. Liao Jingying for her support and guidance of my work at Shanghai Institute of Ceramics. This work drew inspiration and invaluable support from her. And many thanks to Prof. Shen Dingzhong, for his help and support along my work at Caltech.

A number of others played major roles in shaping this work. I would particularly like to thank Wan Lijing, Shen Bingfu, Shao Peifa, Zhou Leping for their industrious efforts in crystal growth.

I would like to also thank my friends whom I worked with and played with at the High Energy Physics CMS group at Caltech: Dr. Zhang Liyuan, Dr. Zhu Kejun and Mrs. Virginia Licon; Chul Tim Chang and his wife, Jin at Pasadena, for their much appreciated ideas, support, who made my stay at Caltech such a beautiful and happy life.

The BTCP samples investigated in this thesis was provided by Drs. P.Lecoq and P.Lecomte. The BGRI samples were provided by Dr.Mingrong Zhang. Part of the

GDMS data used in this thesis was provided by Dr.P.Lecomte. Many interesting discussions with Drs.H.F.Chen, P.Lecomte, F.Nessi and D.S.Yan are acknowledged.

Finally, I would like to thank all my family for their love and encouragement.

Abstract

In this thesis, I present a study of lead tungstate crystals and improvement of radiation hardness.

Precision crystal calorimeters and inorganic crystal scintillators used in high energy physics are discussed in Chapter 1. Two different $PbWO_4$ crystal growth method used at Shanghai Institute of Ceramics are described in Chapter 2. In Chapter 3, radiation damage phenomena in scintillating crystals are discussed in detail. The measurement methods for scintillation properties of $PbWO_4$ and irradiation facilities used at Caltech are presented in Chapter 4.

Results of a study on Sb doping in lead tungstate crystals are presented in Chapter 5. Sb doping is found to reduce slow scintillation components. Result of GDMS trace analysis on raw materials and crystals shows that the concentration of Sb ions in $PbWO_4$ crystals is inhomogeneous. The segregation coefficient of Sb in $PbWO_4$ crystals is determined to be 0.052 ± 0.004, indicating the difficulty of Sb ions to enter the $PbWO_4$ lattice.

The scintillation emission and longitudinal transmittance spectra, light output, decay kinetics and radiation damage were measured for Sb doped $PbWO_4$ crystals. A broad radio luminescence peaked at the blue (430 to 450 nm) was observed for Sb doped $PbWO_4$ crystals, and it has a 50 to 60 nm blue shift as compared to that of photo luminescence. The radiation induced absorption in all Sb doped $PbWO_4$ samples can be decomposed to two color centers with a common center peaked at wavelength of 353 nm (3.51 eV) of a width from 0.25 to 0.54 eV. The other less energetic center is peaked at 537 nm (2.31 eV) for samples prepared with oxygen compensation. These centers are more deeper than radiation induced color centers in trivalent doped samples (3.07 and 2.30 eV). These explains a smaller dose rate dependence of radiation damage in Sb doped $PbWO_4$ crystals.

It is found that Sb doping alone is not sufficient to produce radiation hard lead tungstate crystals, and post growth oxygen compensation is required. Because Sb ions function as pentavalent in high temperature, Sb doping does not make effective compensation for the intrinsic oxygen vacancies in $PbWO_4$ crystals.

A study on Y doped $PbWO_4$ crystals are presented in Chapter 6. GDMS analysis shows Y distribution in $PbWO_4$ crystals is rather uniform. The segregation coefficient of Y ions in $PbWO_4$ crystals is determined to be 0.91 ± 0.04. It was found that light output of Y doped $PbWO_4$ samples in early 1999 is sensitive to the temperature of thermal annealing. Color centers causing "instability"(increase of light output under irradiation) for Y doped $PbWO_4$ samples is concentrated at the tail part of ingots, where defects and some impurities, such as Na, K, Cu and As, are concentrated. Bleaching light at wavelength of 550 or 575 nm seem most effective in removing color centers and resetting Y doped samples to the highest light output.

The radiation induced absorption in all Y doped $PbWO_4$ samples can be decomposed to two color centers with two common centers peaked at wavelength of 400 nm (3.07 eV) and 540 nm (2.30 eV) with widths of 0.76 and 0.19 eV respectively. These two color centers are peaked well apart at two sides of the peak of radio luminescence, and they have different damage and annihilation constants.

$PbWO_4$ light monitoring was discussed in Chapter 7. Because it is less transparent at short wavelengths, the monitoring sensitivity for $PbWO_4$ crystal is better at short wavelength. The best linearity can be achieved with monitoring light wavelength around the peak of radio luminescence weighted with quantum efficiency of photo detector. It is expected that the monitoring wavelength of choice is around 440 nm for all tri-valent or Sb doped $PbWO_4$ crystals. The undoped crystal would require a monitoring wavelength around 510 nm.

Finally, the conclusions of the thesis are given in Chapter 8.

Keywords: Lead tungstate, Doping, Radiation induced, Color centers,

Monitoring

Contents

List of Tables

List of Figures

Chapter 1

Introduction

1.1 Precision Crystal Calorimeters

1.1.1 Introduction

In high energy and nuclear physics, large arrays of scintillating crystals have been assembled for precision measurements of the energy and angle of photos and electrons. Total absorption shower counters made of inorganic scintillating crystals have been known for decades for their superb energy resolution and detection efficiency. The Crystal Ball detector[1] first demonstrated the discovery potential of crystal calorimeters through its study of radiative transitions and decays of charmonium states[2]. Over the last decade, following the Crystal Ball and CUSB[3] experiments, large crystal calorimeters have been constructed, and their use has been a key factor in the successful physics program of the L3 experiment at LEP[4], of CLEO II at CESR[5], and of the Crystal Barrel at LEAR[6].

Recently, several crystal calorimeters have been designed and are under development for the next generation of high energy physics experiment aimed at the study of CP violations. These include a CsI calorimeter for the KTeV experiment at Fermi Lab[7], two CsI (Tl) calorimeters for B Factory experiments: the *BaBar* experiment at SLAC[8] and the BELLE experiment at KEK[9], and a lead tungstate($PbWO_4$) calorimeter for the Compact Muon Solenoid (CMS) experiment at the Large Hadronic Collider(LHC)[10], where the electroweak symmetry breaking physics requires resolutions of the crystal calorimetry[11, 12, 13].

1.1.2 Precision crystal calorimeters in high energy physics

Table 1.1: Crystal calorimeter parameters

Experiment	C. Ball	L3	CLEO II	C. Barrel	KTeV
Accelerator	SPEAR	LEP	CESR	LEAR	FNAL
Crystal Type	NaI(Tl)	BGO	CsI(Tl)	CsI(Tl)	CsI
B-Field (Tesla)	-	0.5	1.5	1.5	-
Inner Radius (m)	0.254	0.55	1.0	0.27	-
Number of Crystals	672	11,400	7,800	1,400	3,300
Crystal Depth (X_0)	16	22	16	16	27
Crystal Volume (m^3)	1	1.5	7	1	2
Light Yield (p.e./MeV)	350	1,400	5,000	2,000	40
Photosensor	PMT	Si PD	Si PD	WS[a]+Si PD	PMT
Gain of Photosensor	Large	1	1	1	4,000
Noise/Channel (MeV)	0.05	0.8	0.5	0.2	Small
Dynamic Range	10^4	10^5	10^4	10^4	10^4
$\mathbf{a_0}$[b] (%)	0.02	0.3	0.2	0.06	<0.1
$\mathbf{a_1}$[c] (%)	0.2	0.1	0.05	0.07	0.5

[a] Wavelength Shifter.
[b] Noise contribution to the energy resolution (at 1 GeV).
[c] Photoelectron statistics contribution to the energy resolution (at 1 GeV).

Tables 1.1 and 1.2 summarize design parameters for major crystal calorimeter projects of the recent past (Crystal Ball, L3, CLEO II, Crystal Barrel) and present (KTeV, *BaBar*, BELLE, CMS) in high energy physics. The parameters $\mathbf{a}_0$ and $\mathbf{a}_1$ represent contributions to the energy resolution (at 1 GeV) from electrical noise and photoelectron statistics, respectively (see Equation 1 in [14]). One notes that each of these calorimeters requires several cubic meters of high quality crystals. The BaF_2 calorimeter design for the GEM experiment [15] at the SSC, and the calorimeter design for the L3P experiment at the Large Hadron Collider (LHC) [16] are included for completeness.

The details of the design of each crystal calorimeter are governed by its physics goals, which are usually related to precision measurements of photons and electrons

Table 1.2: Parameters of recently designed crystal calorimeters

Experiment	*BaBar*	BELLE	CMS	(GEM)	(L3P)
Laboratory	PEP-II	KEK	LHC	SSC	LHC
Crystal Type	CsI(Tl)	CsI(Tl)	$PbWO_4$	BaF_2	CeF_3
B-Field (T)	1.5	1.0	4.0	0.8	2.0
Inner Radius (m)	1.0	1.25	1.29	0.8	2.9
Number of Crystals	6,580	8,800	83,300	15,000	129,600
Crystal Depth (X_0)	16 to 17.5	16.2	25	24.5	23.2
Crystal Volume (m^3)	5.9	9.5	11	11	~50
Light Yield. (p.e./MeV)	5,000	5,000	2	30	50
Photosensor	Si PD	Si PD	APD[b]	VPT[c]	VPT[c]
Gain of Photosensor	1	1	50	12	10
Noise/Channel (MeV)	0.15	0.2	30	3	20
Dynamic Range	10^4	10^4	10^5	10^5	10^5
$\mathbf{a_0}$[d] (%)	0.01	0.01	6	1	6
$\mathbf{a_1}$[e] (%)	0.03	0.03	0.2	0.6	0.5

[a] Wavelength Shifter.
[b] Avalanche photodiode.
[c] Vacuum photo tube.
[d] Noise contribution to the energy resolution (at 1 GeV).
[e] Photoelectron statistics contribution at 1 GeV.

[17]. At low energies (below a few hundred MeV), the large light yields (photoelectrons/MeV) are needed to achieve good energy resolution, and to reduce the energy-equivalent electronic noise (MeV/crystal), which determines the lower limit of the "energy reach" of a crystal calorimeter. These requirements have been met by the Crystal Ball using NaI, and by CLEO II, Crystal Barrel, *BaBar* and BELLE using CsI(Tl). At high energies (above few tens GeV), the energy resolution of a crystal calorimeter is dominated by systematics. The CMS, L3P and the GEM projects have enough crystal depth to achieve a systematic accuracy of less than 0.5%. In the case of KTeV, the crystal depth (27 X_0) also is dictated by the requirement that the energy resolution function have a sufficiently small tail, such that an absolute systematic uncertainty level of 0.02% in the γ energy-scale can be attained, following extensive calibration [7].

The unique physics capability of a crystal calorimeter results form its high electron and photon energy resolution over a wide energy range, uniform hermetic coverage, fine granularity over a large solid angle, and clean electron and photon identification[17]. The combined energy and position resolution of these detector systems results in the best efficiency (and signal-to-background ratio) for the reconstruction of multilepton, lepton-photon, and multiphoton invariant masses as well as in a clean separation of electrons from jets and single hadrons.

A well-designed crystal calorimeter has greater sensitivity than sampling calorimeters (in which the detection medium is interleaved with, or embedded in, a matrix of inert material) for detecting yet-to-be discovered high-mass particles such as the Higgs in the intermediate mass range between 80 and 170 GeV. Experiments that include large crystal calorimeters thus have the capability of isolating rare new physics events from standard physics backgrounds. In future high energy experiments, however, crystal calorimetry faces a new challenge: the radiation damage caused by the increased center of mass energy and luminosity. While the dose rate is expected to be a few rad per day for CsI (Tl) crystals at two B Factories, it would reach 15 to 500 rad per hour for $PbWO_4$ crystals at LHC. In order to maintain high resolution *in situ*, crystals must be radiation hard enough and inter-calibration must be able to follow crystal's change.

1.1.3 The CMS detector

The main motivation for building the LHC is to investigate the mechanism responsible for electroweak symmetry breaking. It provides enough flexibility to allow an investigation of the electroweak symmetry breaking mechanism, even if there were no elementary Higgs bosons. The CMS detector is built around a large, 13 m long, 6 m diameter, high-field superconducting solenoid (4T) leading to a compact design for the muon spectrometer, hence the name Compact Muon Solenoid(CMS). The hadronic and electromagnetic calorimeters are located inside the coil. To detect signatures of new physics efficiently, identification and precise measurement of muons, photons and electrons is emphasized in the design of CMS. With the investigation of the origin of particle masses, the second, and not unrelated, most important task for these detectors will be the search for the supersymmetric partners of Standard Model particles. The primary function of the electromagnetic calorimeter is to measure precisely electrons and photons. The calorimeter system of CMS, is made of a high resolution lead tungstate($PbWO_4$) crystal electromagnetic calorimeter and the hadron calorimeter behind it.

Construction of the LHC was approved by the CERN Council in December 1994[18], and the beginning of operation is presently foreseen in the year 2005. One of the primary objectives of the LHC experimental program is to elucidate the origin of mass, in particular by discovering the Higgs boson predicted by the Standard Model (SM), whatever its mass in the theoretically allowed range up to around 1 TeV. This exciting physics program will be carried out in a difficult experimental environment that imposes challenging requirements on the detector specifications.

The Compact Muon Solenoid (CMS) experiment[18] is a general-purpose detector designed to exploit the physics of proton-proton collisions at a center-of-mass energy of 14 TeV over the full range of luminosities expected at the LHC. The CMS detector is designed to measure the energy and momentum of photons, electrons, muons, and other charged particles with high precision, resulting in an excellent mass resolution for many new particles ranging from the Higgs boson up to a possible heavy Z' in the multi-TeV mass range.

A three-dimensional view of the CMS detector, at the present state of design, is shown in Figure 1.1, which has an overall length of 21.6 m, a radius of 7.5 m and a total weight of about 12,500 ton. CMS consists of a powerful inner tracking system based on fine-grained microstrip and pixel detectors, a scintillating crystal calorimeter followed by a sampling hadron calorimeter made of plastic scintillator tiles inserted between copper absorber plates, and a high-magnetic-field (4 Tesla) superconducting solenoid coupled with a multilayer muon system.

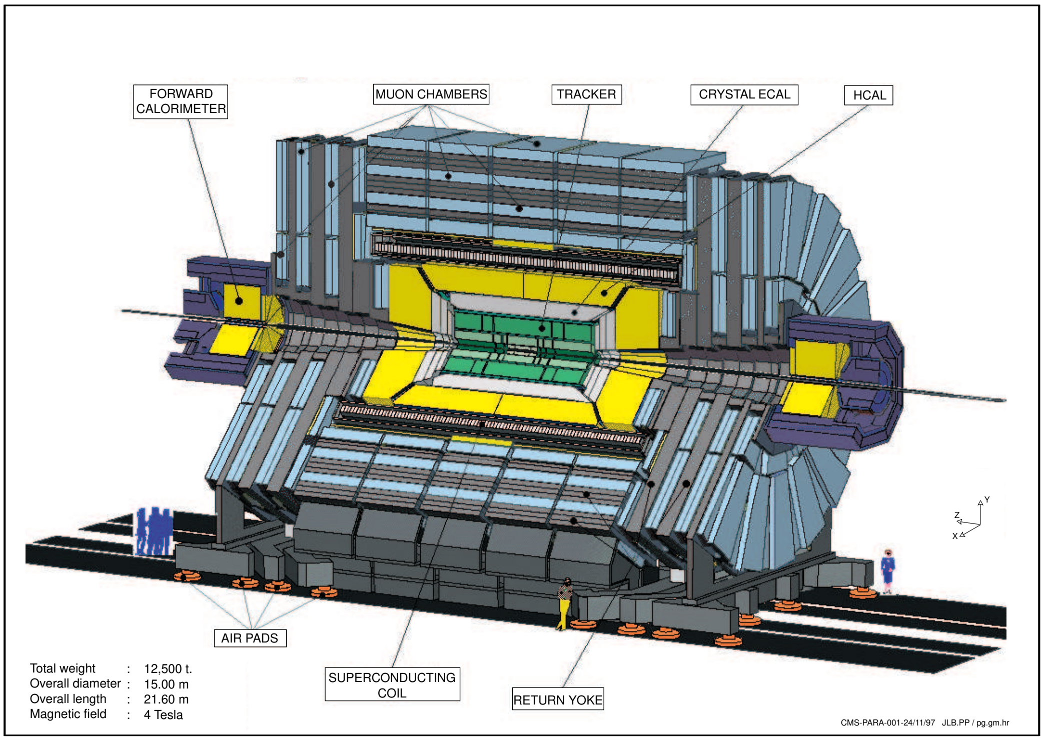

Figure 1.1: Three dimensional view of the CMS detector

The CMS detector can generally be subdivided into one barrel region and two identical endcap regions. The central element of the CMS detector is a 13 m long, 6 m diameter superconducting solenoid generating a uniform magnetic field of 4 T. Located within the solenoid bore are the central tracker and both the electromagnetic (ECAL) and hadron (HCAL) calorimeters. The overall length (excluding the very forward calorimeters) and width of the detector are approximately 22 and 14.6 m respectively, the total weight will be about 12,500 ton.

1.1.4 The electromagnetic calorimeter

The electromagnetic calorimeter(ECAL) will play an essential role in the study of the physics of electroweak symmetry breaking, particularly through the exploration of the Higgs sector. The ECAL will also be an important detector element for a large variety of the Standard Model(SM) and other new physics processes.

Consequently, one of the principal CMS design objective is to construct a very high performance electromagnetic calorimeter. A scintillating crystal calorimeter offer the best performance for energy resolution since most of the energy from electrons or photons is deposited within the homogeneous crystal volume of the calorimeter. High density crystals with a small Molière radius allow a very compact electromagnetic calorimeter system. Furthermore, a high resolution crystal calorimeter enhances the H $\rightarrow\gamma\gamma$ discovery potential at the initially lower luminosities.

Several large crystal calorimeters are successfully operating in high-energy physics experiments(e.g., L3 at LEP and CLEO II at CESR). However, these detectors do not face the difficult experimental environment at the LHC which imposed stringent and challenging requirements on the detector specifications. Compared with the L3 BGO calorimeter, where high precision and wide dynamic range are required, the same criteria have to be met but at a much higher speed and in a much more hostile radiation environment at the LHC. Special efforts have therefore been made during the past few years to develop crystals, photodetectors, electronics and software that provide the performance required by the physics and the LHC.

After an intensive initial R&D program, lead tungstate ($PbWO_4$) crystals were chosen as the baseline for the Technical Proposal[18] because they offer the best prospects of meeting the demanding requirements for operation at the LHC. The choice was based on the following considerations: $PbWO_4$ has a short radiation length and a small Molière radius; it is a fast scintillator; it is relatively easy to produce from readily available raw materials, and substantial experience and production capacity already exits in China and Russia. After selecting $PbWO_4$, R&D efforts have concentrated on the optimization of the technical performance determined by the operating conditions at the LHC. As a consequence of these efforts, the initial drawback of the low light yield has been overcome by progress in crystal growth and through the development of large-area silicon avalanche photodiodes. In Table 1.3 the properties of $PbWO_4$ are compared with those of other crystals used in electromagnetic calorimeters.

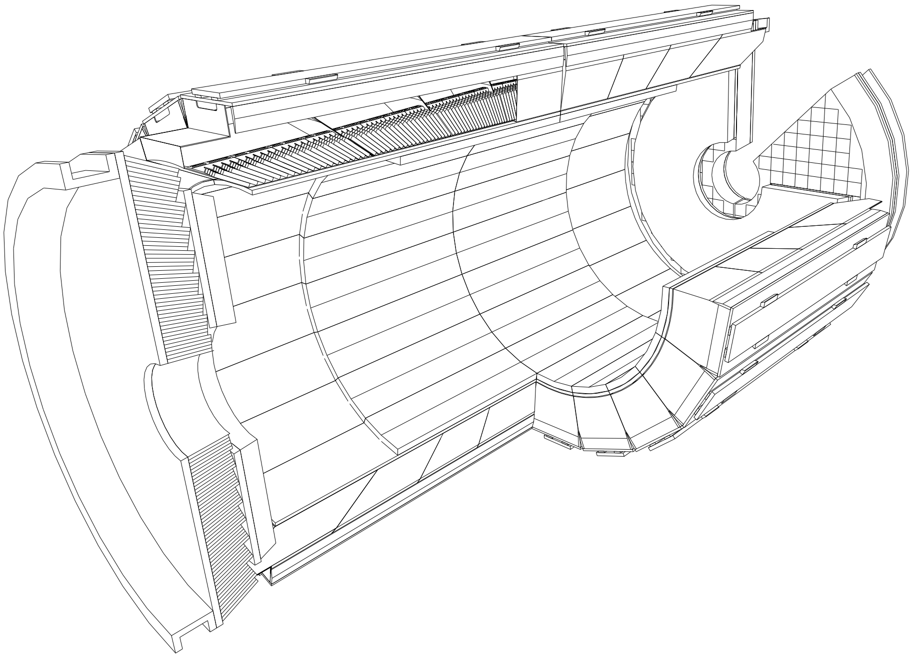

Figure 1.2: A three dimensional view of the CMS electromagnetic calorimeter

The primary function of the ECAL is the precise measurement of the energy of both electrons and photons, and in conjunction with the HCAL the measurement of jets. The large solenoid bore enables both the ECAL and HCAL to be positioned inside the coil and, hence, their performance is not degraded by the particle shower starting in the coil material. The choice of detection technique and design of the ECAL is largely determined by the desire to cleanly detect the intermediate mass Higgs decaying into two photons[19].

The $PbWO_4$ crystals used in the barrel region have a projective geometry with the front face of each crystal having a square section of 20.5×20.5 mm^2. The length of crystals is 23.0 cm corresponding to 25.8 X_0. The crystal are positioned on a cylinder of radius ∼1.44 m. Each half-barrel will be constructed from 18 supermodules each subtending 20°. Each supermodule comprises four 'baskets' with almost equal numbers of crystals. A three dimensional view of the CMS electromagnetic calorimeter showing the barrel and the two endcap regions can be seen in Figure 1.2. The $PbWO_4$ crystals used in the two endcap regions have a square front face of 23.7×23.7 mm^2, a square back face of 25.0×25.0 mm^2 and a length of 22.0 cm (24.7 X_0) with two tapered sides providing an endcap with quasi projective geometry.

To maintain the high resolution and the resultant sensitivity to new physics *in situ*, the detector must be resistant to radiation damage and allow for precision calibration in addition to high speed, mechanical robustness, and a stable readout with high linearity and large dynamic range.

1.2 Inorganic Crystal Scintillators

1.2.1 Introduction

Recently, High Energy Physics has played a major role in the development of new scintillators at an industrial scale, like BGO, CsI, and $PbWO_4$, with important spin-off in other fields like medical imaging, security devices, geology, etc. For a long time the needs for scintillatorsin High Energy Physics(HEP) were rather limited and the only choice was Sodium Iodide, NaI(Tl), because the most important parameter was a high light yield to be able to readout the signals from low energy particles with standard electronics. But in the last decade a new generation of HEP experiments has become a driving force for the development of new scintillators. This has started with Bismuth Cermanate(BGO) for L3[4] and Cesium Iodide (CsI either Thallium doped or pure) for CLEO II[20], Crystal Barrel[6], KTeV[7], Belle[9] and *BaBar*[8], which were already known but in small size and small quantities only.

Then, increasing size of the experiments and the necessity of having a good granularity of the detectors opened the research towards higher density materials. That was the era of BGO with a very high density of 7.13 g/cm^3 but rather moderate light yield and CsI , with a smaller density of 4.51 g/cm^3 but much higher light yield, which seems to have been a good compromise, as it is the only scintillator to have been used in at least 5 large size detectors. Unfortunately the hunt for very rare events imposed to build accelerators of higher luminosity, putting new constrains for short decay time of the scintillators. The requirements for high density have been further increased, whereas the one for high light yields has been somehow reduced because of the increased energy of incoming particles and of the emergence of new type of photodetectors like avalanche photodiodes. These new requirements triggered a strong R&D effort on BaF_2, CeF_3 and $PbWO_4$. The spectacular developments of avalanche photodiodes has led the CMS collaboration to prefer **Lead Tungstate** ($PbWO_4$) crystals with a lower light yield but higher density, to the well developed Cerium Fluoride CeF_3 , in order to build a more compact and less expensive detector.

1.2.2 Commonly used crystal scintillators

Table 1.3 lists the basic properties of commonly used heavy crystal scintillators in high energy physics: NaI(Tl) [21], CsI(Tl) [22], undoped CsI [23, 24, 25, 26], BaF_2[27, 28, 29], CeF_3 [30, 31, 32], BGO ($Bi_4Ge_3O_{12}$) [21] and $PbWO_4$[34, 35, 36]. All these crystals have been used in high energy and nuclear physics experiments, and are available in large quantity. The CsI(Tl) crystal is known to have high light yield, and is widely used. Its photon yield per MeV energy deposition exceeds that of NaI(Tl). The relative light yield of 45% listed in the table is due to the quantum efficiency of the Bi-alkali cathode at its emission peak (7%), which is about 1/3, as compared to 20% of NaI(Tl).

In addition to the crystals listed in Table 1.3, two other heavy crystals have recently been studied. PbF_2 [37, 38, 39] and Ce-doped lutetium oxyorthosilicate (LSO), i.e., $Lu_{2(1-x)}Ce_{2x}(SiO_4)O$ [40, 41]. PbF_2 is another dense material (7.77 g cm^{-3}, X_0 = 0.93 cm, R_M = 2.21 cm) but it is not a scintillator in its common form. Attempts to dope PbF_2 or to grow a crystal with a different structure [42, 43] to make it scintillating have not been successful. It thus does not really belong in this

Table 1.3: Properties of some heavy crystal scintillators

	NaI(Tl)	CsI(Tl)	CsI	BaF_2	CeF_3	BGO	$PbWO_4$
Density (g/cm^3)	3.67	4.51	4.51	4.89	6.16	7.13	8.28
Melting Point (°C)	651	621	621	1280	1460	1050	1123
Radiation Length (cm)	2.59	1.85	1.85	2.06	1.68	1.12	0.89
Molière Radius (cm)	4.8	3.5	3.5	3.4	2.6	2.3	2.2
Interaction Length (cm)	41.4	37.0	37.0	29.9	26.2	21.8	18
Refractive Index[a]	1.85	1.79	1.95	1.50	1.62	2.15	2.2
Hygroscopicity	Yes	slight	slight	No	No	No	No
Luminescence[b] (nm)	410	560	420	300	340	480	500
(at Peak)			310	220	300		500
Decay Time[b] (ns)	230	1250	35	630	30	300	50
			6	0.9	9		10
Relative LY[b,c]	100	45	5.6	21	6.6	9	0.3
			2.3	2.7	2.0		0.4
d(LY)/dT[b,d] (%/°C)	∼0	0.3	−0.6	−2	0.14	−1.6	−1.9
				∼0			

[a] At the wavelength of the emission maximum.
[b] Top line: slow component, bottom line: fast component.
[c] Measured with a PMT with a bialkali cathode.
[d] At Room temperature.

section — it has to be used as a Cherenkov radiator — but it is mentioned here because of the substantial efforts have been devoted to convert it into a low-cost scintillator.

LSO is also dense (7.41 g cm^{-3}, $X_0 = 1.14$ cm, $R_M = 2.3$ cm; similar in these respects to BGO). Its scintillation light peaks at 440 nm (a good match to bialkali cathodes), has a decay time of 40 ns. Its light output is 75% of NaI(Tl). Tests have also shown that it is radiation hard to 100 Mrad [44]. The main obstacles to large scale use of LSO, however, are a very high melting point (> 2,000°C) and very high price (∼100 \$/cc for crystals produced during R&D). A similar material is Ce doped GSO, $Gd_2(SiO_4)O$[45], which has similar desirable properties and practical drawbacks.

The choice of crystals for a crystal calorimeter in high energy physics is governed by its material properties, shower containment, scintillation properties, and radiation hardness. The characteristics and related considerations are summarized below:

MATERIALS PROPERTIES Density, melting point, speed of growth, breaking stress, machinability(cleaving), quality of crystal structure, flatness and crystal structure of polished surfaces, and hygroscopicity all affect the production rate, net yield, and price. They also determine the minimum thickness of support materials that must be placed in front of and between the crystals, which may affect the energy resolution.

SHOWER CONTAINMENT Radiation length(X_0) and Molière radius(R_M) are important factors here. Dense crystals with a shorter X_0 offer a smaller crystal length for longitudinal containment of high-energy electromagnetic showers. For most applications up to the TeV range, $23 - 25X_0$ is sufficient. Lateral containment is controlled by R_M. Of the energy deposited near the longitudinal position of the shower peak, 93% is contained within a perpendicular distance of $\approx$1.5 R_M from the direction of an incident photon.

SCINTILLATION PROPERTIES These include light frequency, decay speed, and temperature dependence. Scintillator in the far UV (such as BaF_2 fast component) must be read out by photosensors with special photocathodes and/or windows. Long light attenuation lengths sufficient for uniform response along the crystal (often limited by the efficiency for reflection at the surface) are more difficult to achieve for wavelength below 300 nm. High speed is an advantage for operation at multi-TeV hadron colliders, particularly for triggering the detector in less that 25 ns between beam crossings. Stability of response, and calibration precise to <0.5%, are easier to achieve if the light output is temperature independent.

RADIATION RESISTANCE Stability of response up to doses of ~10 Mrad at multi-TeV hadron colliders and ~10 Krad at B factories are required for a stable response, and hence for a high resolution.

As summarized below, BaF_2, CeF_3 , and pure CsI are particularly well suited for experiments at future multi-TeV hadron colliders. The commonly used crystals and their main characteristics are as follows:

- NaI(Tl): high light yield; emission well matched to bialkali photocathodes; highly hygroscopic and thus difficult to handle.
- CsI (Tl): high light yield; emission well matched to solid-state photodiodes; high plasticity and resistance to cracking(mechanically robust); slightly hygroscopic. Careful surface treatment is needed[25, 46].
- Pure CsI: relatively fast; emission matched to bialkali cathodes. Otherwise the similar to CsI (Tl) (but may be more difficult to grow). Its scintillation light has –0.6%/°C temperature dependence [23, 24].
- BaF_2: the fast component is the fastest scintillation signal and is temperature independent[27, 28]; intrinsically radiation hard up to the Mrad range[47], but commercially available sample display variable radiation hardness[29, 47]; radiation damage is annealable with visible light[48].
- CeF_3 : relatively new scintillator[30, 31]; relatively fast; light yield nearly temperature independent[32, 49]; emission matched to bialkali cathodes; smaller X_0 and R_m than BaF_2[32, 47, 49].
- BGO: very high density and short X_0 and R_m; emission well matched to photodiodes; not hygroscopic and easy to handle; radiation damage (up to the krad range)[50, 51] can be reduced by Eu doping[52].

1.2.3 Lead tungstate crystals

The CMS electromagnetic calorimeter will consist of over eighty thousand lead tungstate crystals(total weight of 93 ton), avalanche photodiodes or vacuum phototriodes and associated electronics operating in a challenging environment; 4 T field, 25 ns between bunches, radiation doses measured in kGy/year form LHC operation at maximum luminosity, difficult access for maintenance. Although several large crystal calorimeters have been built in the past, none of them has had to face the challenged of speed, radiation resistance and size that an LHC calorimeter will face.

Beyond the known benefits of a homogeneous calorimeter, $PbWO_4$ has been chosen as crystal for various reasons. $PbWO_4$ is a relatively fast scintillator at LHC speeds, with a main light decay component $\tau \sim 10$ ns. It has a fast scintillation emission, with a light decay time which matches the LHC bunch crossing time of 25 ns. $PbWO_4$ is sufficiently fast that very simple pulse-shaping schemes allow a voltage-sampling system to be used without recourse to complex electronics. $PbWO_4$ is a very dense (8.28 g cm^{-3}) material with a short radiation length X_0 of 0.89 cm and a small Molière radius $R_M = 2.2$ cm, enabling thus the construction of a very compact and highly granular calorimeter[10]. The small Molière radius reduces the effect of pileup contributions to the energy measurement by reducing the area over which the energy is summed. At the time of the decision which type of electromagnetic calorimeter to adopt for CMS, substantial $PbWO_4$ production capabilities existed already. This crystals can relatively easily be grown from readily available raw materials. Compared to other crystals, like BGO, it has a modest light yield, but this drawback can be overcome by gains of the photodetectos, such as the PMT and avalanche photodiode (APD). A detailed study on the performance of $PbWO_4$ crystals is underway by several institutions in China, Europe and United States.

System R&D approach has been followed in China, Russia and in the Czech Republic since the end of 1994. The first objective was to grow ingots large enough to extract crystals with the required dimensions: 23 cm in length, 2.05×2.05 cm^2 front section and 2.38×2.38 cm^2 back section. It took several months to obtain crystals of these dimensions with a good mechanical stability and therefore a high cutting and polishing yield.

A second problem was the suppression of slow component in the light emission of $PbWO_4$. It was observed in 1995 that the optimization for a higher light yield had very often the consequence to produce slow components at a few percent level in the crystals. A thorough investigation was made which led to the conclusion that a combination of Molybdenum contamination and bad annealing conditions could introduce such components. After extensive discussions and exchange of ideas at the SCINT95 conference, the problem was immediately solved for the Czech and a few months later for Chinese and Russian crystals.

A very critical parameter for $PbWO_4$ crystals is their ability to survive in the high radiation environment of the Large Hadron Collider (LHC) in the CMS experiment, with the minimum variation of collected light as a function of time. This problem is difficult to solve, as it implies a perfect modelisation of the radiation conditions in the LHC machine, and a very good understanding of the chemistry of defects in $PbWO_4$ crystals. All these aspects have been systematically investigated and significant progress have been obtained which have been published in different papers[53, 54, 55, 56, 57, 58, 59, 60].

During all these R&D phase a constant effort has been made to improve the optical quality of the crystals and optimize the scintillation conditions in order to increase the amount of light yield of good $PbWO_4$ crystals for a given parameter. A combined effort between CMS and producers, Shanghai Institute of Ceramics, Shanghai, China and the Bogoroditsk Techno-Chemical Plant in Tula, Russia, is under way to optimize mass-production procedure to long, high-quality $PbWO_4$ crystals. Milestones towards this goal have included: understanding the $PbWO_4$ scintillation mechanism; enhancing the light output; understanding the radiation damage mechanisms and developing techniques to produce radiation-hard crystals; understanding the mechanical properties of the crystals and producing stress-free crystals to avoid breakage during cutting and polishing; finding the most economical way of mass-producing these crystals.

The intrinsic properties of lead tungstate crystals had been thoroughly tested in the laboratory and in the beam tests, and many results can be found in several publications[10, 61, 62]. The R&D results can be summarized as follows:

MATERIALS PROPERTIES $PbWO_4$ is a birefringent, tetragonal, scheelite-type crystal belonging to the space group $\mathbf{I4_1/a}$ or monoclinic raspite (space group $\mathbf{P2_1/a}$)[63]. The raspite phase transforms irreversibly to the stolzite one at about 400 °C[73]. $PbWO_4$ shows interesting luminescence[74] and acousto-optical properties[75]. The first information on the emission properties of lead tungstate is dated as early as the late 1940s[74]. It is grown from a 50% - 50% mixture of lead oxide(PbO) and tungsten oxide(WO_3) which melts congruently at 1123°C, without a phase transition during cooling. The $PbWO_4$ crystal is optically and mechanically anisotropic and care must be taken during the growing process to avoid formation of cleavage planes. This anisotropy, which can be a cause of mechanical instability, is well understood and its effects are controlled by a judicious choice of growth and annealing conditions. Properties of lead tungstate are listed in Table 1.3 and compared to those of other crystals used in electromagnetic calorimeter.

SHOWER CONTAINMENT A total thickness of about 25 radiation length is required to limit the longitudinal shower leakage of high-energy electromagnetic showers to an acceptable level. This corresponds to a crystal length of 23 cm in the barrel region. The presence of a preshower (a total of $3X_0$ of lead) in the endcap region allows the use of slightly shorter crystals(22 cm).

SCINTILLATION PROPERTIES $PbWO_4$ is a relatively fast scintillator at LHC speeds, with a main light decay component $\tau \sim 10$ ns. It has a fast scintillation emission, with a light decay time which matches the LHC bunch crossing time of 25 ns. $PbWO_4$ has a rather weak but fast emission because of a strong quenching of the scintillation process. This quenching is rather complex but to a large extent associated with high-temperature charge transfer process and thermal decomposition of excited states. The efficiency of these two mechanism can be modified by the presence of some impurities, as demonstrated in 1995[59]. The thermal quenching of the scintillation mechanism leads to a rather strong temperature dependence of the light emission, of typically -1.98 %/°C at room temperature[56]. The temperature coefficient of the crystals, and of the APD, implies that the temperature of the calorimeter must be stabilized to a tenth of a degree.

RADIATION RESISTANCE $PbWO_4$ is intrinsically radiation hard, but non-optimized crystals do suffer from radiation damage. The R&D carried out over the last few year has led to a better understanding of this damage mechanism:

1. One very important parameter which is relatively easy to measure and strongly correlated with the optical and radiation-hardness properties of the crystal is the optical transmission spectrum. The transparency of the crystal is only indirectly connected to the calorimeter performances: the light transmission, in fact, is required to exceed a minimum value in order to have a good light collection uniformity and sufficient light yield.
   - the longitudinal measurement through the 23-cm-long crystal allows the detection of even weak absorption bands which give a good indication about the light yield and radiation hardness of the crystal. Particularly important is the control of the sharpness of the optical transmission edges ad the absence of the 420 nm absorption band. The transverse measurement at different points along the crystal also gives the longitudinal uniformity of the optical parameters of the crystal.
   - the optical transmission of the crystals has been steadily improved, in particular in the region of scintillation, between 340 and 570 nm. The optical transmission of $PbWO_4$ crystals can be limited by the presence of macroscopic defects like inclusions, precipitates or veils which scatter the light in all directions, or by the existence of traps which induce absorption bands. The most frequent traps observed in $PbWO_4$ are located near the valence and conduction bands and affect the shape of the transmission edge. A band at 350 nm believed to be due to oxygen defects if frequently observed. Another band at 420 nm, believed to be caused by the presence of holes trapped by lead ions, is responsible for the yellowish coloration of

some crystals.

  - a better control of the raw material preparation and of the growth and annealing conditions, as well as the introduction of dopants, have led to considerable improvement in the optical transmission of CMS size $PbWO_4$ crystals. The improvement of the transparency of crystals has been associated with an increase in the amount of collected light. Light yield values in excess of 10 photoelectrons/MeV are now systematically observed in a gate of 200 ns on a photomultiplier covering all the back face of 23 cm long crystals, with over 90% of this light being contained in a 100 ns gate and with no detectable afterglow.

2. Beam test measurements has shown that irradiation does not affect the scintillation mechanism in the crystals, at least in the range of dose rate considered at LHC[64, 65], and indeed no change of shape is observed in the crystal emission spectrum[64, 66]. It has also been shown that damage resulting in light yield loss of 15% causes a degradation in resolution of less than 0.2%, if well monitored. Tests with electrons, gammas and charged hadrons all confirm that the damage can only be attributed to the electromagnetic interaction.

3. Radiation damage affects the transparency of the crystals through the formation of color centers related to defects in the crystals introduced by mismatched stoichiometry and creation of oxygen vacancies. This conclusion was reached by detailed material analysis[67, 68]: a glow discharge mass spectroscopy(GDMS) analysis revealed no correlation between the detected trace impurities and the crystal's susceptibility to radiation damage; electron microprobe(EMPA) and particle-induced X-ray emission (PIXE) analysis revealed that crystals with poor radiation hardness have a non-optimal Pb/W ratio[66, 69, 71]. Thus the light transport is changed by self-absorption of the crystals, and effect of irradiation can be quantified by a radiation-induced absorption coefficient μ_{ind} (expressed in m^{-1}). The loss of transmission due to irradiation will be mon-

itored by a light injection system in the calorimeter, and a correction can be established and applied.

4. Extensive studies on the radiation damage mechanism have led to the conclusion that it is not driven by extrinsic impurities but by host-structure defects acting as traps[66, 70]. The improvements have been achieved by using a combination of optimized raw materials purity, stoichiometric ratio, oxygen-annealing[55] or specific doping, depending on the growth technique. All crystals doped in conditions of optimized raw materials show a considerable improvement of radiation hardness with a light-yield decrease of less that 5% after several days of irradiation at a dose rate similar to that expected in most of the calorimeter at high luminosity.

5. Irradiation does not change the uniformity of collected light yield along the crystal, provided that the initial light attenuation length is long enough and the damage remains moderate. This has been proven experimentally by a measurement of longitudinal uniformity after irradiation[66, 71]. Highly transparent $PbWO_4$ crystals have a non-uniform light yield response due to the tapered shape of the crystals and the high refractive index of lead tungstate ($n = 2.3$ at 500 nm). Light yield uniformity can be restored by roughening the lateral faces to reduce total reflection. Numerous studies performed in laboratories with sources or with particle beams showed in particular that:

   - an adequate light-collection uniformity can be achieved by depolishing one or several faces of the crystals;
   - the choice of the wrapping does not significantly affect the uniformization;
   - the resulting light yield non-uniformity in the region of shower maximum is less than $(0.3 \pm 0.1)\%$ per X_0.

6. The loss in the amount of collected light stabilizes at a level dependent on

the dose rate, an effect well described by the creation of color centers under irradiation and their annihilation through room-temperature annealing[69, 71].

7. There is no damage recovery with time constants of less than a few hours for dose rates that will be encountered at the LHC. Correspondingly, irradiation only induces a loss of 5 to 8% of transmitted light in the $PbWO_4$ crystal, which is at a tolerable level for the CMS ECAL, especially since the effect saturates at low doses(∼1 krad), and the recovery time is of the order of several days. The loss of transmission due to irradiation can then be monitored as foreseen through a light injection system in the calorimeter. However, it has to be ensured that consistently no fast recovery is present, since it would be hardly monitored.

In Shanghai Institute of Ceramics, China, the R&D efforts are continuing for the production of crystals with good radiation hardness properties. The efforts were concentrated there as well on all aspects of crystal growth, where progress was aimed at in steps, with successful production of 5cm long, extremely radiation hard crystals[55], progressing then to 10 cm long radiation resistant samples[72] and now working on full-size crystals. In parallel, SIC is preparing the infrastructure for mass production, through the development of multiple crystal furnace, where 10-crystal furnace are already operation and two 28-crystal furnace are being constructed, along with cutting and polishing machines. Optimization of growth parameters has been pursued in Shanghai Institute of Ceramics to maximize the crystal yield. The growth yield has reached 70%, and further improvements aim at a final growth yield of 80%.

The CMS ECAL is now in the preproduction phase. Some R&D is still being performed to (1) understand crystals' performance and (2) improve crystal quality, especially radiation resistance, to consolidate the quality of the detector elements subject to the highest demand in terms of stability and radiation resistance. The investigation described in this thesis titled "**A Study of Lead Tungstate Crystals and Improvement of Radiation Hardness**" is an integrated part of this effort.

In Chapter 2 of the thesis, the growth methods for $PbWO_4$ crystal production at Shanghai Institute of Ceramics are described. Raw materials and doping are also discussed is this chapter.

In Chapter 3, some radiation damage phenomena in $PbWO_4$ scintillation crystal were given in detail.

In Chapter 4, the measurement methods of scintillation properties are described, including the measurement of longitudinal transmittance, light attenuation length, scintillation emission spectra, light output, decay time and uniformity of crystals, irradiation facilities are also described in the end of this chapter.

In Chapter 5, the test results of Sb doped crystals are presented, including segregation coefficient of Sb in $PbWO_4$, radiation damage and its radiation hardness improvement.

In Chapter 6, a complete study on latest Y doped $PbWO_4$ crystal is presented, including Y distribution in $PbWO_4$ crystal, "instability" of Y doped $PbWO_4$ under room temperature, radiation damage, and long term stability of crystal.

In Chapter 7, $PbWO_4$ light monitoring is discussed. Correlations between variations of transmittance and light output are analyzed, the results of monitoring sensitivity, linearity and wavelength determination are presented in this chapter.

Finally, the conclusions of the thesis are given in Chapter 8.

Chapter 2

Crystal Growth

2.1 Czochralski Method

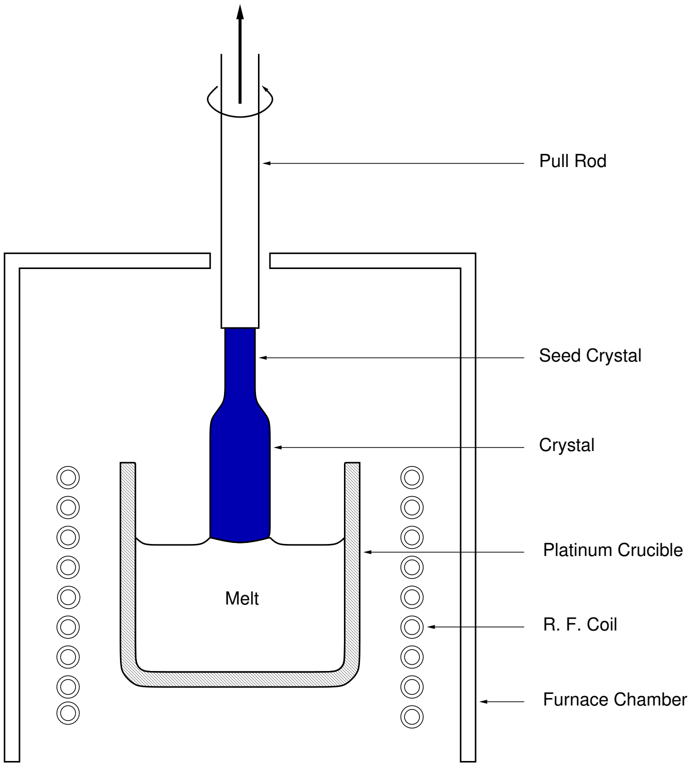

Figure 2.1: The Czochralski growth of $PbWO_4$ crystal at SIC

Two different crystal growth methods can be used to produce large size lead tungstate crystals. The Czochralski method is currently used in Russia and Czech

Republic to grown $PbWO_4$ crystals[10]. The modified Bridgman-Stockbarger technique is used at SIC to produce large size $PbWO_4$ crystals. But for $PbWO_4$ crystal growth at SIC, crystal seed was produced by Czochralski method. Figure 2.1 illustrates the principles of the Czochralski technique currently being used for the growth of $PbWO_4$ seed crystal from melt at high temperature at SIC. It is the purpose of this section to explain the basic techniques of this method adopted by SIC to grow $PbWO_4$ seed crystal.

"Crystal pulling" or the Czochralski technique (1918)[76] is a popular method of crystal growth because it can produce large, dislocation free crystals in a relatively short space of time. Crystal pulling is in many ways the most satisfactory method of growing crystals. It is the only method of growing crystals from the melt in which there is real scope for producing large dislocation-free crystals. This is because the solid-liquid interface is no longer in contact with a crucible and the radial temperature gradients can be kept small by suitable design of the crucible system.

2.1.1 Crystal puller

The main advantage of crystal pulling is that it is a "real time" technique whereby the size and diameter of the crystal can be controlled while it is growing. The principle of the method is shown in Figure 2.1, the essential parts of a crystal puller are: a crucible to hold the melt, a means of heating the melt, a seed, and a mechanism for producing relative motion of the seed and melt. In the apparatus shown in Figure 2.1, which has been used to grow crystals of lead tungstate in air, the seed is held in a chuck attached to a shaft which is raised and rotated. The $PbWO_4$ melt in this apparatus is contained in a platinum crucible which is heated by the R.F.field from the coil shown. This represents an extremely simple crystal puller, and the sequence of operations is:

1. A rotating seed crystal (hatched) is brought into contact with the melt and then slowly raised.

2. The diameter of the crystal is increased by lowering the crucible temperature and pulling continued.
3. To a first approximation constant crucible temperature gives a constant diameter crystal. Small divergences can be corrected by decreasing the seed rotation or decreasing the pulling rate all of which increase the diameter of the crystal or by reversing these changes the diameter can be decreased.
4. After the desired length of crystal has been grown, the crucible temperature is raised to cause the diameter to decrease until the crystal breaks contact with the melt.

Nassau and Broyer[77] have suggested that an ideal material suitable for growth by the pulling technique would have the following properties: (1) congruent melting point; (2) no destructive phase changes; (3) low vapor pressure; (4) low viscosity; (5) suitable growth habit and (6) no destructive cleavage. However, there exist methods for overcoming most of the problems raised by the absence of some of these properties.

Melt growth of any kind is very much dependent on there being a satisfactory crucible material to contain the melt. Lewis[78] *et al.* have summarized the main requirements of a good crucible material, which are: (1) the crucible material be insoluble or only slightly soluble in the melt; (2) it must be as free as possible from impurities which might be transferred to the melt; (3) it must be readily cleanable so that any surface impurities can be removed; (4) the crucible must have high strength and physical stability under normal conditions of use; (5) it must have low porosity to facilitate degassing, and (6) it must be easily machinable or formable into the crucible shape required.

A further property of the crucible material, which is important if the crucible is going to be used with r.f. heating, is the resistivity. It is preferable if the crucible has round corners as this aids stirring of the melt. In $PbWO_4$ crystal growth by Czochralski method at SIC, a metal platinum crucible is used, which considerably adds to the strength of the crucible. Precious metal crucibles are usually used with r.f. heating at high temperatures. It is advisable to have a fairly thick wall in these circumstances because otherwise hot spots can occur and the crucible itself may melt with catastrophic(and expensive) results. The crucible must be fairly robust in order to resist mechanical damage when the remain of a melt are being removed after a run.

One of the essentials of Czochralski(crystal pulling) is that the melt must be kept at a precisely controlled temperature. There are several ways of supplying the power to melt the material to be grown: radio-frequency heating, resistive heating, gaseous combustion, lasers, thermal imaging, electron beams and arcs. The most common methods are resistive and r.f. heating because they are the easiest to control and do not impose many constraints on the crystal growing system. The melt is usually kept at a controlled temperature by a closed loop control system. More work had been focused on using either the weight of the crystal[79] or the weight of the melt[80] as the input parameter to the control system. This would appear to be more reliable than using optical systems which are liable of fogging.

2.1.2 Seeding

One of the advantages of Czochralski(crystal pulling) over other techniques of crystal growth is that some of the defects in the seed crystal need not be propagated into the grown crystal. The ideal seed for crystal pulling is a defect-free, oriented single crystal of the material to be grown. When a crystalline seed is being used, some care must be taken to make sure that any work damage or residual strain is removed before it is used. A low dislocation seed which has been etched to remove the work-damaged layer and annealed to remove strain is preferable. The problem then exists of reducing the number of crystallites propagated into the growing crystal. This is usually done by the process called “necking”. The process simply consisting of making the diameter as small as possible by increasing the pull rate or slightly increasing the melt temperature. After some time when an appreciable narrow length of crystal has been grown, the growing crystal is then allowed to increase its diameter. The process can be repeated several times if necessary and any non-axial dislocations will gradually be eliminated as well.

When the seed has been mounted in the crystal puller, it should be lowered slowly towards the melt in order to avoid thermal shock. The seed is rotated at the same time in order to attain thermal symmetry and also to stir the melt. The melt should be hot enough to melt back some of the seed to ensure that uniform epitaxial growth takes place. The choice of orientation of the seed can be important.

A slight seed misplacement will cause uncontrollable increase in diameter and unstable interface. Subsequently, the crystal started to grow out along side ways nonuniformity. Supercooled melt regions as wave-like extrusions were observed around the growing crystal. Once this kind of melt supercooling occurred, then any change in seed rotation rate and/or in temperature to get rid of it was not successful, the number of extrusions of supercooled regions increased twofold and all of the sudden the diameter of the crystal reached that of the crucible. Ultimately the growth was terminated in the shoulder stage itself.

So the seed and initial seal-on are of prime importance[81]. Under suitable conditions dislocations which are not parallel to the growth axis grow out of a crystal. It is, however, usual to use a low dislocation seed. For the growth of high quality crystals, good seed crystals are required. In general, seeds should be cut with care and cutting damage should be removed by polishing or etching. Since the seed may have been mechanically worked (e.g. ground to fit its holder) it is desired to etch the seed heavily to remove any damaged surface. The seed should be pre-heated by lowering very slowly to the melt surface so as not to introduce dislocations by thermal shock.

It is important to ensure a good seal-on(i.e. complete wetting). This is most readily achieved by using a relatively small diameter seed and allowing plenty of time to elapse before commencing to pull. In order to eliminate any dislocations present in the seed or caused by the seal-on, the initial growth should be made at seed diameter or slightly less. Typically a length of 3 to 10 seed diameters should be grown before expansion. The use of a small diameter seed has the additional advantage that there will only a small total number of dislocations to be grown out.

2.1.3 Growth procedure

The growth procedure is simple. A charge is melted in the crucible, the seed is brought into contact with the melt. The crucible temperature is then adjusted so that the seed neither grows nor melts. This temperature is held for a few minutes to ensure that the melt has completely wetted the seed and then the temperature is lowered and pulling started. When the diameter needs to be increased, the crucible temperature is lowered. A typical crystal will have a diameter between 25 and 60% of the crucible diameter. A practical limit with manual control is 45 – 50%. With larger crystals there is a problem in seeing into the crucible and many workers prefer to use 30 –35%. At the end of growth cycle, the diameter is decreased by raising the crucible temperature.

Once the growth as commenced there are a number of further points. The presence of scum on the melt will give rise to particles on the solid surface with, in general, different emissivities from that of the solid. This will result in thermal straining which may give rise to dislocations. This effect depends on the atmosphere in the puller. To eliminate thermal strains the radial temperature gradient must also be kept small. In order to stop the formation and collapse of vacancy discs the rate of cooling of the crystal must be kept small. This is most easily done by reducing the axial temperature gradient.

The main requirements for growing good crystals by this method are that the pull and rotation rates should be smooth and that the temperature of the melt should be accurately controlled. The diameter of the crystal is dependent on both the temperature of the melt and the pull rate. To increase the diameter of a crystal being grown, either the power is reduced or the pull rate decreased, the opposite applies for reducing the diameter. The maximum size of crystal that can be produced by this technique is governed by the volume of the melt, the diameter of the crucible, the distance that the pull rod can move and the strength of the crystal at its minimum diameter. And additional practical limitation will be how well the seed is secured into its holder – nothing is more depressing than seeing a freshly grown crystal becoming detached and sinking back into the melt.

An important parameter governing the quality of a pulled crystal is the shape of the solid-liquid interface. The best crystals are usually grown with a flat interface because a curved one gives rise to a non-uniform impurity distribution across the face of the crystal. Where an interface is convex into the melt it is possible for some low index planes to be parallel to part of the freezing isotherm and for facets to form. This can be overcome if a sufficiently high rotation rate is used(100-200 rev/min). The shape is also governed by ambient gas pressure and the length of the crystal[82].The interface becomes less concave towards the melt as the pressure increases and as the length of the crystal increases.

The rotation rate has other effects besides altering the shape of the interface, it alters the flow patterns in the melt and hence the temperature and impurity distribution[83, 84, 85]. Details study of flow patterns can be found at[83, 84, 85, 103]. The choice of pull rate is dependent on a number of factors: (1) diameter of the crystal required, (2) melt temperature, (3) importance of dislocation inclusions and (4) constitutional supercooling.

The choice of pull rate is usually a compromise between growing the crystal as fast as possible and the introduction of defects that this produces. The crystal is rotated otherwise it will assume a cross-sectional shape which corresponds to that of the temperature distribution in the melt. If the crucible is not heated uniformly the crystal will grow laterally towards the coldest part producing a non-circular cross-section. A slow rotation rate of about ten rev/min is sufficient to overcome this but a higher rotation rate will produce increased stirring which will help prevent the build up of impurities at the solid-liquid interface. Impurities are often incorporated into the crystal in bands which are caused by variations in the growth rate due to temperature fluctuations produced by convective currents in the melt. These convection currents can be minimized by placing a baffle in the melt[86].

It is essential for this method that the temperature distribution in the melt should be such that the temperature of the solid-liquid interface is the lowest in the liquid. If it is not, spurious nucleation will occur. The surface of the melt must also be kept free from dust and particles of the melt which have been condensed above the crucible, otherwise these too will act as nucleation centers. It is probable that as large a crystal as possible will be wanted but it should be borne in mind that the larger the diameter, the more strain there will be present and the higher the dislocation density. The dislocation density also increases with increased growth rate.

2.2 Modified Bridgman-Stockbarger Method

In this method, due to Bridgman[87], a crucible containing a molten charge is moved slowly, relative to a stationary temperature gradient for unidirectional solidification. Figure 2.2 shows the growth of a crystal by what is usually called the vertical Bridgman technique. In this method the material to be grown is first completely melted in a crucible. This is lowered through a temperature gradient which results in solid forming first at the end of the seed $PbWO_4$ crystal. With a correctly shaped crucible only one crystal usually grows. The principal characteristic of the method is that the solid-liquid interface is completely enclosed by the crucible so that latent heat of solidification can only be removed by conduction through the solid and the crucible. In the apparatus shown, the baffle helps to give uniform temperature in the two portions(the upper and lower portions) with a steep temperature gradient between them.

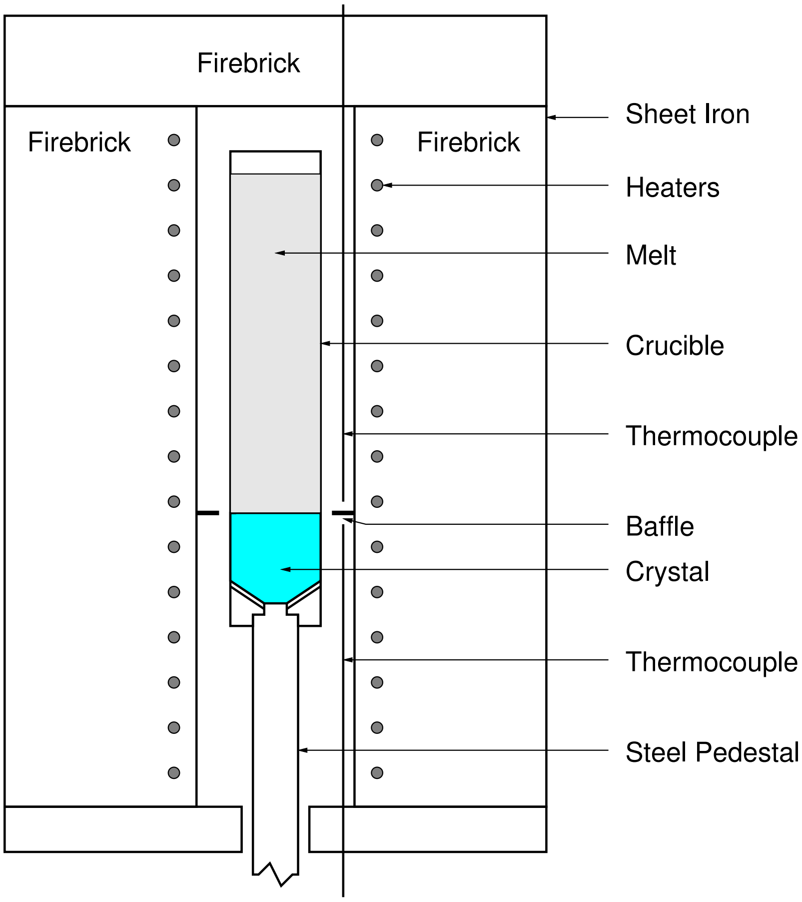

Figure 2.2: The Bridgman-Stockbarger's arrangement for $PbWO_4$ crystals grown in atmosphere

It has been shown that, if homogeneous crystals are required, it is essential to have uniform growth conditions and this implies a high degree of control over the heat source. This control can only be obtained easily by using electrical equipment. The subject of temperature control has been reviewed by Ansley[88]. Since the crucible supports the melt it must be sufficiently strong at the working temperature to do this. In addition, it may be a vital part of the thermal system as, for example, the source of heat or as a diffuser to even out both spatial and temporal temperature irregularities.

The correct choice of crucible material is of prime importance to the growth of satisfactory crystals. An obviously desirable property of a crucible material is that it should not react with the melt. If the grown solid will be in contact with the crucible, to eliminate strain, the crucible should have a lower coefficient of expansion that the solid. Prior to use the crucible it is essential to clean crucible thoroughly.

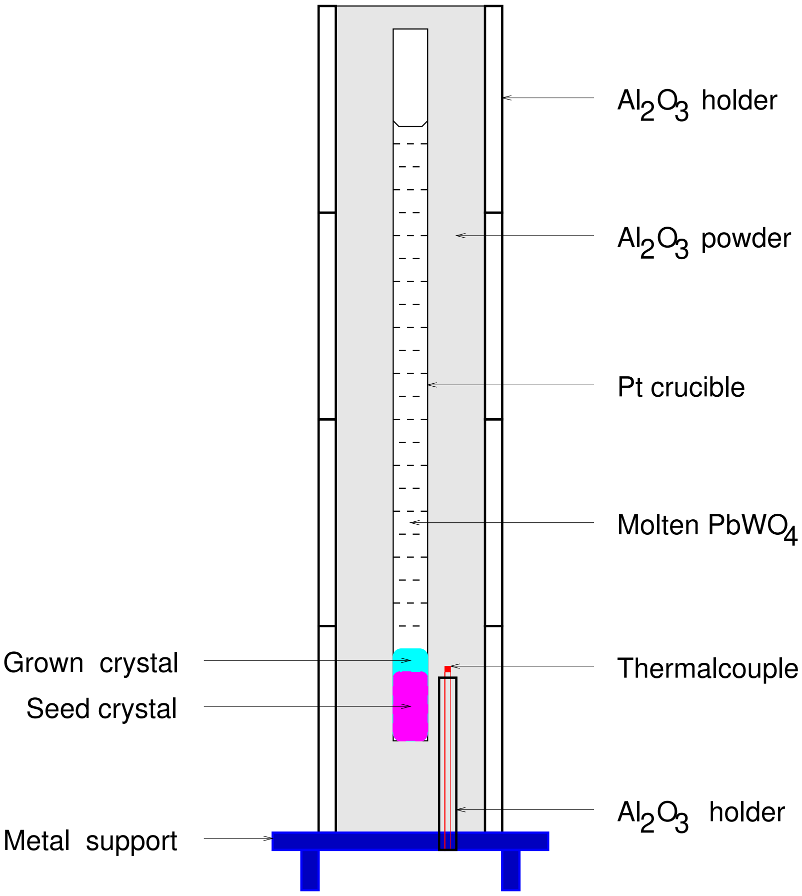

Figure 2.3: Crucible configuration of the modified Bridgman-Stockbarger method for the growth of $PbWO_4$ at SIC

$PbWO_4$ single crystals were grown by Modified Bridgman technique in Shanghai Institute of Ceramics, Shanghai, China. Raw materials of high purity, PbO (5N) and WO_3 (4N), are produced in Shanghai, and are mixed in precise stoichiometric proportion of $PbWO_4$ in an agate mortar. The mixture is first melted in a platinum crucible in air for a period of time to ensure complete homogeneity. After heated to high temperature this melt is sintered into platinum crucible to form polycrystalline $PbWO_4$ grogs for crystal growth. Figure 2.3 shows a schematic structure of a crucible arrangement in modified Bridgman Method for the growth of $PbWO_4$ at Shanghai Institute of Ceramics.

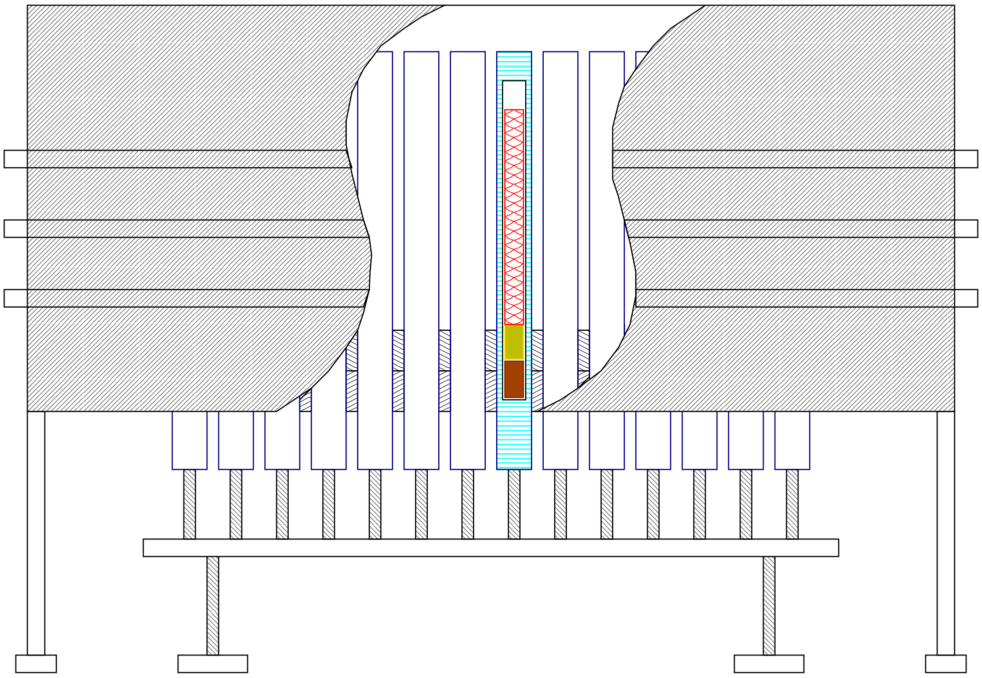

Figure 2.4: A schematic view of a typical Bridgman furnace with 28 crucibles.

At Shanghai Institute of Ceramics, multiple crucibles with individual computer controlled temperature profile are constructed in each furnace, allowing multiple pulling in one furnace. The layout of the furnace and its temperature profile can be found in [91]. Figure 2.4 is a schematic showing a typical furnace with 28 crucibles for $PbWO_4$ growth. Furnaces of this kind were developed during 1980's at SIC to grow BGO for the L3 experiment, and were later successfully adapted for growth CsI(Tl) crystals for the *BaBar* and BELLE experiments, and for growth of $PbWO_4$ crystals for the CMS experiment.

The stability fo temperature field in furnace is crucial for successful growth of large size crystals. It can be found that in the case of crystal growth by Bridgman method, the thermal strain in the boule is mainly due to inappropriate longitudinal thermal field. The temperature in these furnaces was monitored by Pt-Pt/Rh thermocouples and controlled by DWT-702 temperature controller. During crystal growth the variation of temperature is required to be less than ±0.5°C, which stabilized the crystal growth rate and reduces the density gradient in the diffusion layer of the solid-liquid interface so that the density of constitutional super-cooling defects is minimized. Under the optimized thermal field for growing high quality crystal, the thermal gradient should be as small as possible. Of course, the cooling speed should be also under control. With these measures, the risk for cracking for $PbWO_4$ crystal will be alleviated to a great extent.

The crucible used at Shanghai Institute of Ceramics are made of platinum by moulding and welding techniques. Instead of conventional crucibles with conical bottoms, flat-bottom crucible have been successfully been used at SIC for $PbWO_4$ crystal growth. A serious technical difficulty in Bridgman growth from large volume of $PbWO_4$ melt is the corrosion of $PbWO_4$ melt against platinum crucible during the long period of growth. The wall of crucible sometimes is corroded to form ditches and micro-cracks. In serious case, it leads to leakage of the $PbWO_4$ melt during the crystal growing process. The ductility of platinum metal can be recovered after the purification and treatment of the platinum fragments by chemical methods to insure the reproduction of platinum crucible.

The crystal cracking is mainly attributed to the difference in thermal expansion coefficients of $PbWO_4$ along a and c directions and to that of platinum. When the crystal is grown along c axis, it will tend to shrink much more along the growth direction than along the normal direction because of the higher ratio between the thermal expansion coefficients α_c (along the c-axis: $2.95\times10^{-5}/°C$) and α_a (along the a-axis: $1.28\times10^{-5}/°C$). But the wetting along the crucible wall will not allow the crystal to shrink freely. This along with the higher ratio between α_C and α_{Pt} (the thermal expansion coefficient of platinum: 1.02×10^{-5}/°C) leads to tension and hence normal (to the growth direction) cracking. For the crystal grown along a(or b) axis the above-mentioned tensile force will act in a direction perpendicular to the growth direction. This leads to the parallel cracking along the length of the crystal. In this case sometimes cracks are also observed along a direction at an angle of about 25° which is attributed to the cleavage phenomenon as the cleavage plane for $PbWO_4$ is (101) at an angle of 24.38° to the <100> direction[89, 90]. When thinner crucible is used, the above-mentioned effects are very much reduced and crack-free crystals could be obtained.

Crystals were grown aloing the c axis at SIC, twenty eight crucibles of rectangular shape are constructed in every furnace for CMS $PbWO_4$ crystal growth. This shape of crucible makes efficient use of raw material since only a small fraction of ingot needs to be cut off to make final dimension. Therefore the utilization ratio of the materials is very high. The as-grown $PbWO_4$ single crystals are transparent, colorless without visible defects, such as cracking, inclusions, scattering particles and growth striation. Optimization of growth parameters has been pursued to maximize the crystal yield at Shanghai Institute of Ceramics. The growth yield has reached 70%, and further improvements aim at a final growth yield of 80%.

The modified Bridgman-Stockbarger method has many advantages over the Czochralski method including: (1) simple operation with no complicated automatic diameter control system; (2) low-temperature gradient alleviating the problem of cracking which is more pronounced in the case of $PbWO_4$; (3) large size high quality scintillation crystal can be grown; (4) multi-crucible structure furnace offers the capability for mass production, and (5) by using different shaped crucible, the ingots with desired shape can be grown and the utilization ratio of the material is high.

The practical requirements of the techniques described in section 2.1 and section 2.2 have many common features. For example, it is always important to eliminate random temperature variations. Thus, temperature control systems are vital to the growth of high quality crystals. Similarly, these two methods involve parts in slow relative motion and it is important that these movements shall be steady. Reviews of crystal growth technology can be found in[102] and [103].

2.3 Raw Material and Doping

2.3.1 Raw materials

Raw materials used to grow scintillation crystals are required to have high purity, preferable 5N or 6N. The high cost, however, prevents the use of material of extra high purity. Research is needed to find and selectively remove harmful impurities. Various material characterization means are available to determine trace elements in raw material as well as crystals. Among them Glow Discharge Mass Spectroscopy(GDMS) analysis is commonly used. It surveys 77 elements in a sample with precision of sub ppm level for metallic contamination.

The identification of impurities, defects and structural changes are crucial for $PbWO_4$ crystals development, since they are possibly responsible for the blue absorption, the slow decay components and the susceptibility to radiation damage.

The result of GDMS analysis revealed that the presence of slow scintillation component in $PbWO_4$ is due to the Mo contamination, as reported by R.Y.Zhu [97] and Kobayashi [96]. Since Mo is naturally contaminated in WO_3, special effort was made to reduce its contamination. After removing Mo and other cation contamination from the raw materials, $PbWO_4$ crystals produced at SIC have significantly reduced the slow component.

Table 2.1 lists the result of GDMS analysis for trace elements (ppmw) in raw materials of different batches since 1998 from Shanghai Institute of Ceramics. Also listed the date of these raw materials produced. All detected impurities at a level greater than 1 ppm are listed, in addition to the sum of the transition metals (TM):

Table 2.1: GDMS analysis results(ppmw) of raw materials

Raw	PbO					WO_3				
Date	04/98	11/98	03/99	12/99	04/00	04/98	11/98	03/99	12/99	04/00
Na	0.08	0.03	0.02	0.02	<0.01	0.15	0.07	0.07	0.46	0.16
Mg	0.01	0.01	0.05	0.02	<0.01	0.04	0.01	<0.01	0.02	0.08
Al	0.70	0.42	0.85	0.25	0.42	0.22	0.22	0.30	0.36	0.35
Si	0.15	0.12	0.27	0.26	0.14	0.15	0.25	0.25	2.0	2.4
K	0.15	0.06	<0.05	<0.05	<0.05	0.23	0.32	0.11	0.12	0.28
Ca	<0.05	0.18	0.22	0.52	<0.05	0.36	0.11	<0.07	0.30	0.35
Mo	0.01	0.03	<0.01	0.02	<0.01	0.61	0.61	0.20	0.32	0.36
Sb	<0.05	<0.05	<0.05	<0.05	<0.05	0.20	<0.05	<0.05	<0.05	<0.05
TM[a]	0.50	<0.30	<0.40	<0.40	<0.30	1.10	<1.00	<0.40	<1.10	<0.50
RE[b]	<0.30	<0.50	<0.50	–	–	<0.20	<0.50	<0.30	–	–

[a] Sum of transition metals.

[b] Sum of rare earths.

Sc, Ti, V, Cr, Mn, Fe, Co, Ni, Cu and Zn, and the sum of detected rare earth elements (RE): Ce, Pr, Nd, Eu, Sm, Gd, Tb, Dy, Ho, Er, Tm, Yb and Lu. Mo contamination is less than 1 ppm. This results showed that the raw materials used at SIC have stable high purity.

2.3.2 Doping

Among other properties, a good radiation hardness is required for the use of $PbWO_4$ crystals in the CMS electromagnetic calorimeter due to the expected radiation level at LHC[10]. Therefore, a strong effort has been performed during the last years at Shanghai Institute of Ceramics(SIC) in order to understand the radiation damage mechanism and to achieve the necessary level of radiation hardness of full size $PbWO_4$ crystals. Extensive studies on the radiation damage mechanisms in $PbWO_4$ crystals have shown that damage in $PbWO_4$ is caused by host structure defects, such as oxygen vacancies [97, 98, 99, 100, 101]. These defects introduce local charge unbalance which can easily trap electrons or holes and consequently induce the formation of color centers under irradiation.

One way of reducing the impurities and defects in the $PbWO_4$ crystals is related to the purification of raw materials (PbO and WO_3) and the optimization of the growth techniques. Another way of decreasing host structure defects concentration is related to the optimization of the stoichiometric ratio between two oxides and its control during the crystal growing process. The role of stoichiometry and related structural defects to the radiation damage effect of $PbWO_4$ was studied and reported in other papers[69, 59]. It is shown this optimization was not sufficient to obtain the radiation hardness level required for CMS. And then, ways to suppress or compensate the remaining defects by specific doping of $PbWO_4$ crystals are proposed. In order to have or improve the scintillating properties of crystals, specific ions are intentionly added to the crystals, which is called doping.

Doping $PbWO_4$ crystal lattice by heterovalent ions has been used as a method to modify natural point defects and color center concentrations with the aim to increase $PbWO_4$ radiation hardness and to modify possibly also other scintillation characteristics. Doping $PbWO_4$ by specified ions like Nb, La, Lu and Y at optimized level of concentration has shown a significant improvement in the sharpness of the transmittance band edge which has resulted in increased transparency. All crystals doped with these ions in conditions of optimized raw materials also showed a considerable improvement of radiation hardness [92, 95, 94].

In this direction, doping $PbWO_4$ by La, Nb, Sb, or Y ions and its growth was intensively studied at SIC, with an aim to improve its radiation hardness, transmittance, and possibly also other scintillation properties. A certain amount of dopant was introduced into the melt, in the form of an oxide, during the growth-cycle, to produce doped crystal. Some dopants were introduced at different levels, in different crystals, in order to study their effect quantitatively. Dopants can usually be added to the material to be grown when the crucible is being filled at the start of a run. GDMS analysis were systematically performed for different position of Sb or Y doped $PbWO_4$ crystal after growth. These measurements allowed us to determine the segregation coefficient of the doping ions and to tune the doping conditions.

In parallel to specifying the doping level, an uniform distribution of dopant in the crystal is expected as much as possible. The distribution of dopant ions between the solid and liquid phase during crystal growth is a complicated process which depends on the growth conditions as well as on the nature of the ionic species. The effective segregation coefficient k_e defined as the ratio of the concentration of dopant in the bulk crystal, $C_{crystal}$, to the concentration of dopant in the melt, C_{melt}, is simple used to describe the ability of the dopant to enter into the solid phase, i.e., $PbWO_4$ single crystal:

$$k_e = \frac{C_{crystal}}{C_{melt}} \tag{2.1}$$

Therefore, when growing the doped $PbWO_4$ crystals, both the growth conditions and the segregation coefficient of the dopant must be taken into account technically.

Burton, Prim and Slichter[93] define the effective distribution coefficient as that describing the overall reaction of the solute incorporatin into the solid at non-zero growth speeds in the steady state. The implication here is that only at zero growth velocity the equilibrium distribtion coefficeent is decisive in solute incorporatin into the solid. For the Bridgman process, th following assumptions are made for the derivation of the first expression: (1) diffusion of the solute, under consideration, is negligible in the solid, (2) the effective distribution coefficetn k_e is constant, and (3) the density change of the solution during freezing is zero.

Then the solute concentration (e.g., solute atoms/unit volume) in the solid immediately behind the interface is given by:

$$C_{crystal} = k_e C_0 (1 - g)^{k_e - 1} \tag{2.2}$$

where $C_{crystal}$ is the solute concentration(dopant concentration) in the solid, and g is the solidified fraction of the original volume of unity.

Equation 2.2 can be rewritten in the logarithmic form:

$$\ln\left(\frac{C_{crystal}}{C_0}\right) = \ln k_e + (k_e - 1)\ln(1 - g) \qquad (2.3)$$

It can now be used for a simple experimental dertamination of k_e. The logarithmic plot of $C_{crystal}/C_0$ against (1-g) is a straight line and its slope and intercept at $g = 0$ will provide a measure of k_e[1].

---

[1] The assumptions made here are in fact valid for (1) systems with complete mixing (i.e., C_L uniform) and (2) steady state systems with partial mixing where the growth velocity and the thickness δ of the diffusion layer is constant.

Chapter 3

Radiation Damage Phenomena

3.1 Radiation Damage in Scintillating Crystals

The interaction of ionizing radiation with a scintillation crystal invariably creates radiation damage. The creation of radiation damage is a complicated process which involves not only the host material but also the impurities and defects in the crystal. These inhomogeneities enhance the probability of the creation of the radiation-induced point defects or color centers in the crystal. The incident radiation can cause changes in optical and scintillation properties of the crystal during irradiation and after accumulating large doses. The properties of the inorganic scintillator can be impaired under irradiation in the following ways:

1. The formation of color center absorption bands that absorb photons emitted by the luminescence centers: a decrease in optical transmission is especially dangerous in the large gamma detectors for high energy physics.

2. Direct effect of the radiation on luminescent centers and change of the emission characteristics (efficiency, spectrum, decay time); the luminescence centers may be rendered inoperable (quenched) due to valence changes or compensatory ion diffusion. The degradation of the scintillator light emission can also occur because of reduction of energy transfer from electrons and/or holes to luminescence centers. The radiation-induced defects and traps decrease the mobility of the carries.

3. Created shallow traps increase the level of afterglow.
4. Heavy crystals irradiated by high energy hadrons (protons, neutrons, mesons. etc.) display induced radioactivity; this can influence the operation of electromagnetic calorimeters.

A large body of research shows that the degradation in optical transmission is the most important effect of radiation damage. In most crystals, an observed loss in scintillation light output can be explained by a decrease in transmission rather than in luminescence. Therefore, the radiation hardness studies refer first to measurements of the optical transmission of a scintillator irradiated by various doses of radiation.

All known crystal scintillators suffer from radiation damage. The principal damage phenomenon observed in all mass-produced crystals is the appearance of absorption bands, caused by color-center formation. Most damages recover under room temperature, and can be fully cured by thermal annealing although at different temperature, depending on the depth of color center traps. Optical bleaching which may be implemented *in situ*, is also effective for many crystals.

These absorption bands reduce the transmission of scintillation light in the crystals and hence the apparent light yield following irradiation. Additional effects observed in some crystals include reduced intrinsic yield of scintillation light, increased fluorescence, and phosphorescence(spontaneous light emission over a long period). For a crystal to be used in a high-radiation environment, such as at multi-TeV hadron colliders, its scintillation mechanism must not be damaged and the radiation-induced phosphorescence must not affect the read-out signal. Crystals such as BaF_2 or CeF_3 meet these criteria. However, the increased radiation-induced absorption (equivalently, a reduced light attenuation length) changes the light-response uniformity and thus may degrade the energy resolution.

The absorption bands reduce crystal's light attenuation length (LAL), and hence the light output. The color center formation, however, may or may not cause a degradation of the **light response uniformity**. The radiation also causes phosphorescence (afterglow), which leads to an increase of readout noise. Additional effect may include a reduced intrinsic scintillation light yield (damage of the scintillation mechanism), which would lead to a reduced light output and a deformation of the light response uniformity. The damage may recover under room temperature, which leads to the **dose rate dependence** [71]. Finally, thermal annealing and optical bleaching may be effective in eliminating color centers in the crystal.

The radiation-induced formation of color-centers and the decreased absorption length are usually related to impurities and/or structural defects in the crystals. The impurities may be present as substitutional or interstitial trace element atoms in the lattice, or they may occur as molecular ions or as microscopic color-center complexes containing many atoms. An in depth study of (1) the trace element content and distribution in the crystals, (2) the quality of the crystal structure, and (3) the density and structure of the inclusions in a series of crystal samples was carried out for BGO in in 1981-1985[50, 51, 52] and for BaF_2 from 1988-1993[29, 27, 28, 47]. From this study, it is known that the impurities may lead to macroscopic structures which have a high density of trace-element rich color center complexes clustered together. These structures form inclusions which are visible under a low power microscopic and, in some cases, to the naked eye. These data were cross-correlated with the degree of radiation damage in a series of doped and undoped crystal samples, which led to greatly improved processing technology for growing types of crystals. As a result of the improved control of raw materials, crystal growth, and annealing methods, crystals with greater radiation resistance were produced. At this writing, studies of the radiation damage problem for pure and doped $PbWO_4$ are still underway.

In previous studies, it is concluded that the scintillation mechanism of BGO [51], BaF_2[29] are not damaged, and the consequence of the radiation-induced phosphorescence is negligible for BaF_2[29] and $PbWO_4$[66]. It is also known that the damage in BGO [51], BaF_2[29] and $PbWO_4$ [66] are thermally annealable, as well as optically bleach-able, while it is not in CsI [104].

3.1.1 Radiation-induced color center formation and recovery

Primary effect of radiation damage is degradation in transparency rather than that in luminescence[50, 47]. Decrease in optical transmission is especially dangerous in the γ–detectors for high energy physics. This is because even a small decrease in transmittance per unit length should accumulate over as long as 20 radiation lengths. Consequently, degradation in optical transmission, in other words polarization, should be the most important and the most extensively studied effect of radiation damage.

The most common damage in scintillating crystals is the radiation-induced color center formation, which reduces the light attenuation length and thus the light output. Depending on the type of the defects in the crystal, the color centers may be electrons located in anion vacancies (F center), or holes located in cation vacancies (V center), or interstitial anion atoms (H center) or ions (I center). Radiation-induced color centers formation may be observed by measurement of crystal's transmittance.

It should be noted that definition of radiation hardness has not been very clear in publications. Usually this terminology has been used as a measure which gives the maximum dose tolerated in actual detectors. Such tolerable dose may depend on the detector depth.

The left plot of Figure 3.1 shows the longitudinal transmittance changes of four full size (~23 cm long) $PbWO_4$ samples measured immediately after γ-irradiation.The radiation-induced absorption bands in $PbWO_4$ are broad, and can be seen in all four samples SIC-210(undoped), SIC-275(Sb doped), BTCP-2150(La doped) and BTCP-1978(Nb doped). It can be seen from Figure 3.1 that, for the radiation hardness samples, i.e., SIC-275 & BTCP-2150, the radiation-induced absorption bands are narrower than those of radiation soft samples(SIC-210 & BTCP-1978). Compared the degradation level of the longitudinal transmittance for these four different doping full size $PbWO_4$ samples, it is also can be seen that the degradation level of the longitudinal transmittance for two radiation hardness samples(SIC-275 & BTCP-2150), is much smaller than those of two radiation soft samples(SIC-210 & BTCP-

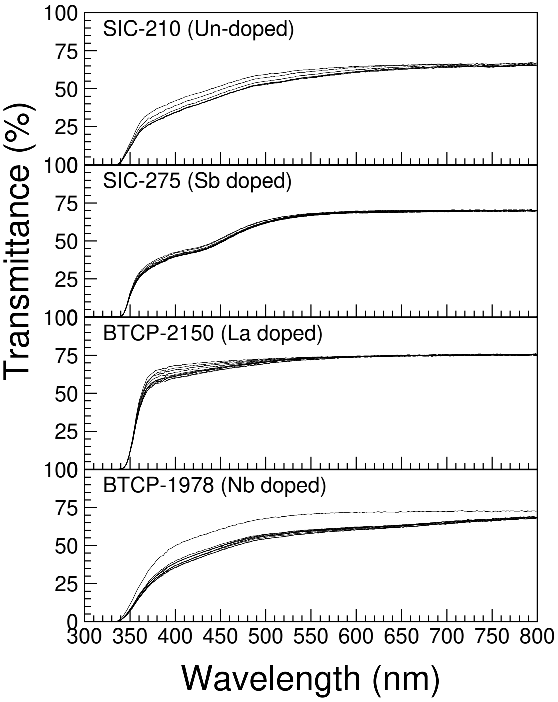

Figure 3.1: Longitudinal transmittance of full size $PbWO_4$ samples, showing radiation-induced absorption bands

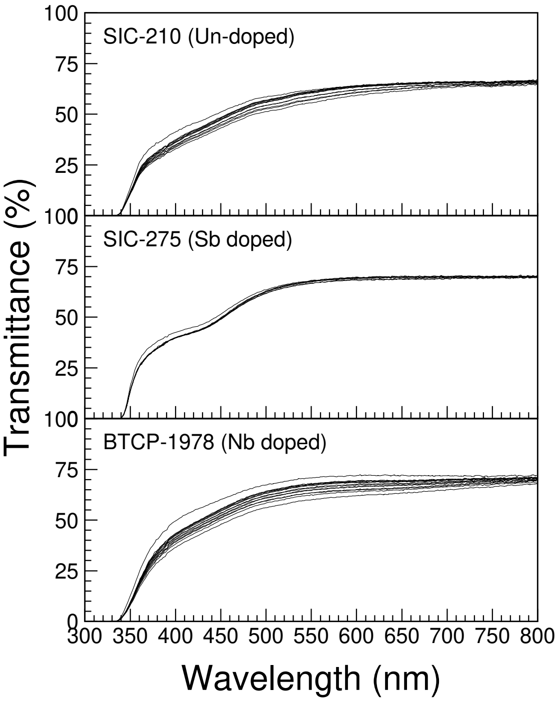

Figure 3.2: Longitudinal transmittance of full size $PbWO_4$ samples, showing the recovery of radiation damage for radiation-induced absorption bands

1978).

Some irradiated crystals can recover their transmission with time. The natural recovery rate is an important parameter at the stage of preliminary choice of scintillators, because this permits correction of the radiation hardness. However, the recovery of many scintillators is extremely slow at room temperature, especially in the short wavelength region. Almost complete recovery in transmission can be obtained after thermal bleaching of a sample at elevated temperature. The temperature (usually 200 to 350°C) and duration of the bleaching depend on the properties of color centers in the crystal.

A more suitable way of recovery of the optical transmission is irradiation of crystals by ultraviolet (UV) or visible light. This feature of the recovery provides an important way of dealing with radiation damage in the actual detector by allowing for the possibility of annealing the crystals in intervals when the detector is not operating. Almost full recovery in the transmission can be reached after exposure to light from tens of minutes to several hours, depending on the intensity of the light source with a specially selected wavelength. The right plot of Figure 3.2 shows the

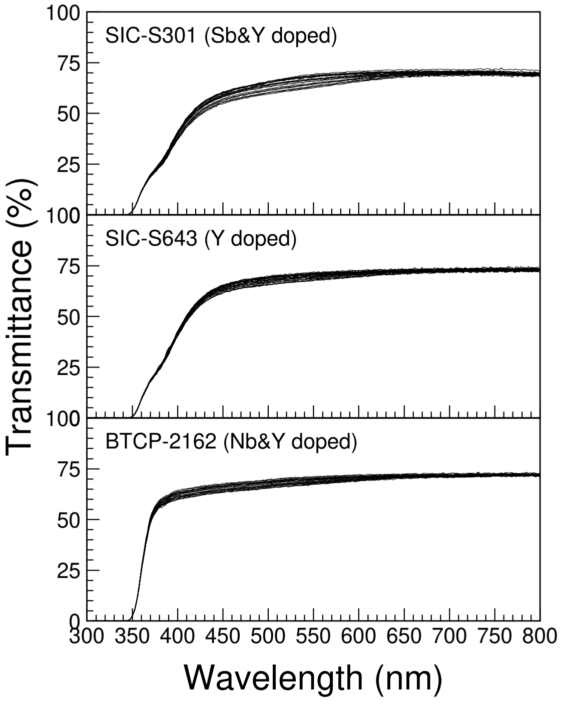

Figure 3.3: Longitudinal transmittance of full size $PbWO_4$ samples, showing radiation-induced absorption bands

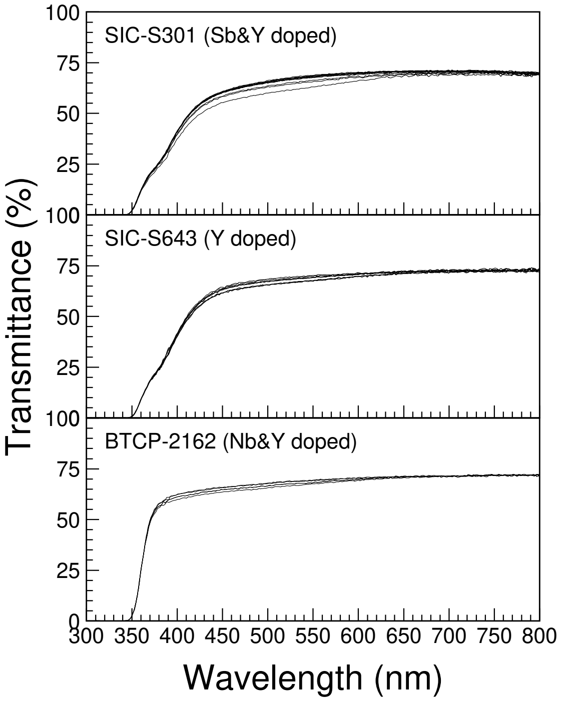

Figure 3.4: Longitudinal transmittance of full size $PbWO_4$ samples, showing the recovery of radiation damage for radiation-induced absorption bands

recovery of longitudinal transmittance for full size ($\sim$23 cm long) $PbWO_4$ samples after γ-irradiation. The radiation-induced absorption bands in $PbWO_4$ recovered with different time constants after irradiation.

The left plot of Figure 3.3 shows the longitudinal transmittance changes of three full size ($\sim$23 cm long) $PbWO_4$ samples after γ-irradiation. The radiation-induced absorption bands are clearly identified in all samples SIC-S301(Sb/Y doped), SIC-

S643(Y doped) and BTCP-2162(Nb/Y doped), which are produced in last two years. It can be seen from Figure 3.3 that the radiation hardness for $PbWO_4$ produced from both in Russia and China are much improved and both met the requirements for CMS detector construction. The right plot of Figure 3.4 shows the recovery of longitudinal transmittance for full size (∼23 cm long) $PbWO_4$ samples after γ-irradiation. The radiation-induced absorption bands in $PbWO_4$ recovered with different time constants after irradiation. A more detailed discussion of color centers can be found in references [33].

3.1.2 Light response uniformity

An adequate light response uniformity profile is the key to the precision of a crystal calorimeter. The effect of the light response uniformity to the energy resolution has been studied by full GEANT simulations for each designed crystal calorimeter. Figure 3.5 [29] shows the GEANT predictions for the energy fraction (top figure) and the intrinsic energy resolution (bottom figure) calculated by summing the energies deposited in a 3×3 sub-array, consisting of tapered BaF_2 crystals of 25 radiation length, as a function of the light response uniformity. In this simulation, the light response (y) of the crystal was parametrized as a normalized linear function:

$$\frac{y}{y_{mid}} = 1 + \delta(x/x_{mid} - 1) \tag{3.1}$$

where y_{mid} represents the light response at the middle of the crystal, δ represents the deviation of the light response uniformity, and x is the distance from the front(small) end of a tapered crystal.

Figure 3.6 shows the definition of the light response uniformity in this simulation and a schematic illustrating its measurement in laboratory by shooting a point γ-ray source at different locations of a tapered crystal.

While the change of the amplitude of the light output can be inter-calibrated, the

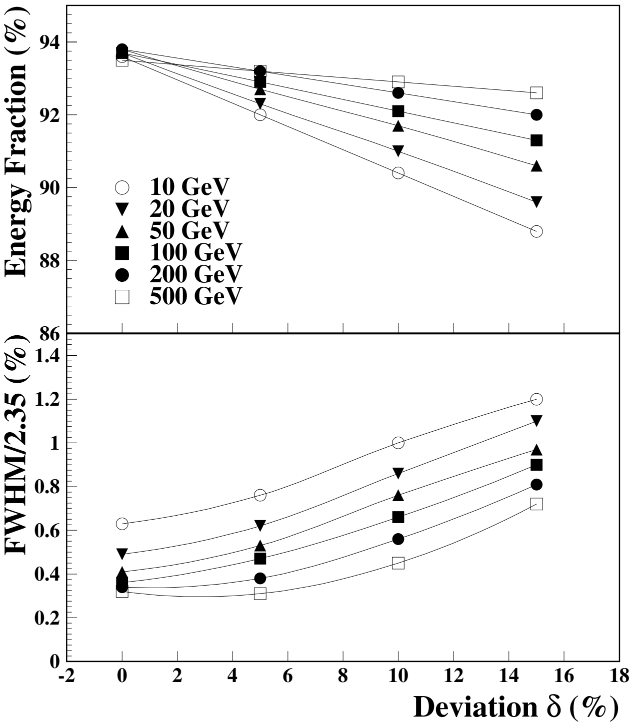

Figure 3.5: The relative mean energy fraction and the energy resolution for electromagnetic clusters of 3 × 3 crystals as a function of light response uniformity, derived with a GEANT simulation [29]. See Equation 3.1 in the text for the definition of parameter δ

loss of the energy resolution, caused by the degradation of light response uniformity is not recoverable. To preserve crystal's intrinsic energy resolution the light response uniformity thus must be kept within tolerance. According to above simulation, the δ value is required to be less than 5% so that its contribution to the constant term of the energy resolution is less than 0.5%. A recent simulation fo CMS $PbWO_4$ crystals[107] confirmed this conclusion.

To maintain a systematic limitation to the intrinsic energy resolution to less than 0.5%, the δ value is required to be less than 5%, and thus a light attenuation length

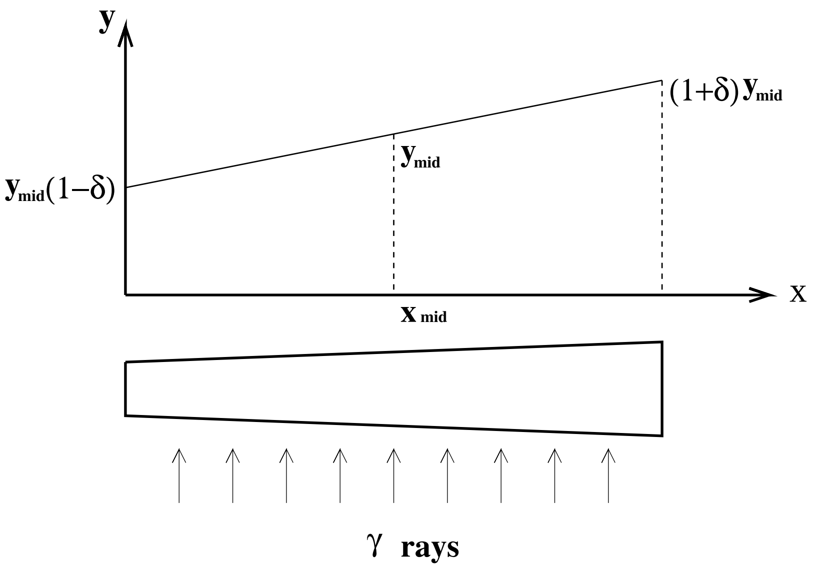

Figure 3.6: A schematic showing the light response uniformity definition and its laboratory measurement

(LAL) of longer than 95 cm. A detailed study using many different functional forms of the light response non-uniformity, in addition to a linear dependence, confirmed this conclusion quantitatively [105].

Light response uniformity can be achieved by using special wrapping or coating techniques. For a tapered crystal with its 6 faces polished, there are two counter-balancing factors which affect the light uniformity over the crystal length: the light attenuation (both bulk attenuation and losses at each reflection) and an "optical focusing" effect. The optical focusing effect can be understood in terms of Liouville's theorem: as the crystal gets larger and a bundle of light rays thus is allowed to expand, the individual rays within the bundle tend to become more parallel to the long axis of the crystal. While light attenuation causes a decrease of the response with increasing distance from the photosensor, the optical focusing effect leads to higher light collection efficiency and thus increasing response with distance. For a 24 cm BGO crystal, the second factor dominates: a strong increase of the light response (up to a factor of 2.4) at the small end compared to the large end was observed for L3 crystals which had all sides well-polished [4].

In general, uniform light response has been obtained by treating at least part of the crystal surface to avoid total internal reflection that continues over many bounces – effectively "trapping" part of the light in the crystal – and to instead scatter the light diffusely, randomizing the direction of light rays within the crystal. Common techniques are (1) depolishing the lateral crystal faces in a nonuniform and carefully controlled manner (Crystal Ball) [106], (2) coating all surfaces of the crystals with a highly reflective diffuse reflector, such as a 40-50 μm thick coating NE560 white paint NE560 (L3 BGO calorimeter) [4], or (3) teflon or aluminized Mylar wrapping (KTeV CsI calorimeter) [7].

3.1.3 Light output degradation and recovery

The most direct representation of crystal radiation hardness is degradation of its light output after irradiation. We use light output normalized to that before irradiation. To reduce systematic uncertainties of this measurements, light output was defined by an average of several measurements with collimated ^{137}Cs source shooting at evenly distributed positions along the sample. We use 9 measurements for CMS size samples.

Figure 3.7 and 3.8 show light output degradation(solid dots with error bars) as a function of time for samples BTCP-2133 and BTCP-2162 respectively. Measurement were done step by step for four different dose rates: 15, 100, 500 and 1,000 rad/h, as shown in the figures. The dose rate dependence of light output degradation is clearly observed.

Figure 3.9 and 3.10 show light output degradation(solid dots with error bars) as a function of time for Y doped samples SIC-606 and SIC-S643 respectively. Measurement were done step by step for three different dose rates: 2, 15, and 100 rad/h, as shown in the figures. Once again, The dose rate dependence of light output is clearly observed. Compared $PbWO_4$ samples produced from BTCP and SIC, the

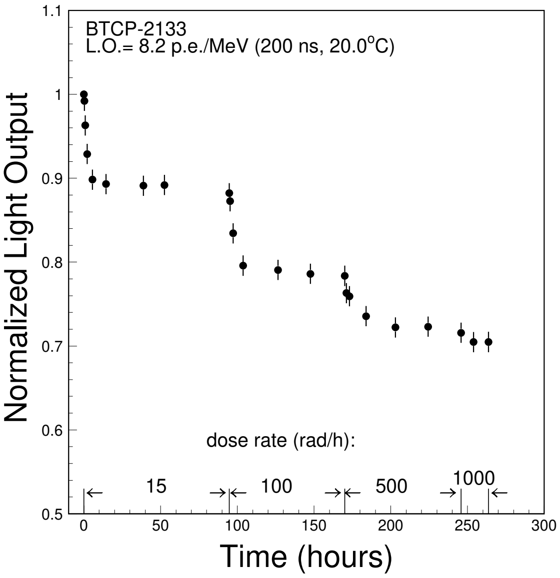

Figure 3.7: Light output is shown as a function of time under irradiation at 15, 100, 500 and 1,000 rad/h for Nb/Y doped sample BTCP-2133

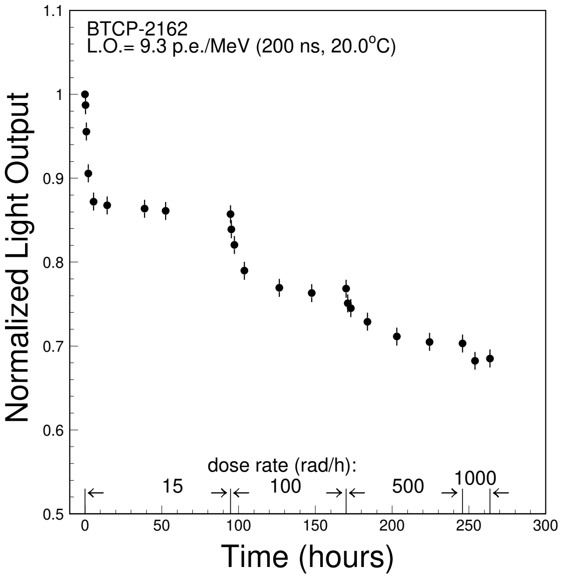

Figure 3.8: Light output is shown as a function of time under irradiation at 15, 100, 500 and 1,000 rad/h for Nb/Y doped sample BTCP-2162

performance of Y doped samples(SIC-606 and SIC-S643) from SIC are identical to preproduction samples(BTCP-2133 and BTCP-2162) from BTCP. It is clearly that the radiation hardness for crystals produced recently in SIC are much improved.

The radiation damage in crystal may recover at room temperature - a consequence of room temperature thermal annealing. The recovery speed, however, depends on the depth of the traps. A slow recovery would ease the calibration requirement, therefore it is preferred for crystals to be used in a radiation environment. It is known that damage in BaF_2[29] and CsI [104] recovers at an extremely slow speed, while BGO[51] and $PbWO_4$[60] do recover at a speed of orders of few hours to few weeks.

Figure 3.2 and Figure 3.4 show the recovery in the transmittance as a function of wavelength for $PbWO_4$ samples after irradiation. Figure 3.11 and Figure 3.12 show the damage recovery of normalized light output as a function of time after irradiation for samples BTCP-2162 and SIC-606. The solid line in the light output plot is a fit to an exponential recovery with a time constant of 71.9 h and 84.9 h for BTCP-2162 and

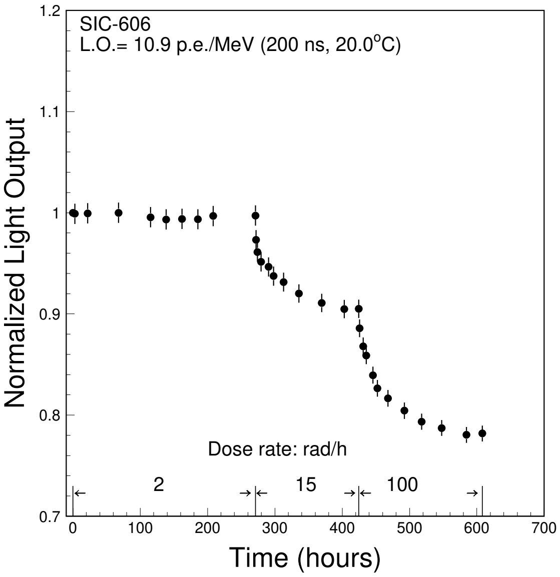

Figure 3.9: Light output is shown as a function of time under irradiation at 2, 15 and 100 rad/h for Y doped sample SIC-606

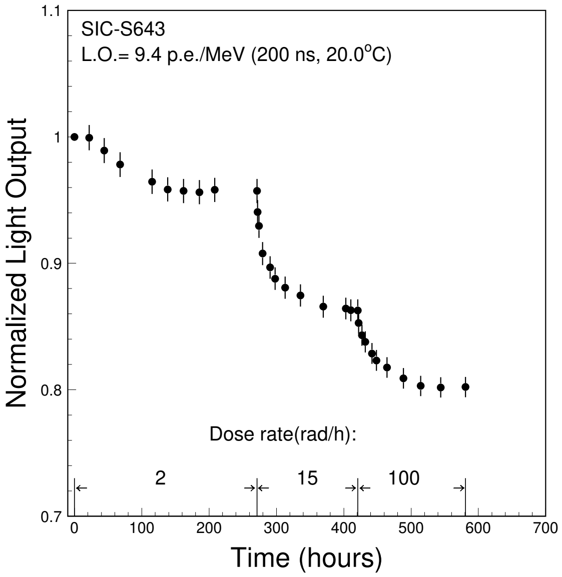

Figure 3.10: Light output is shown as a function of time under irradiation at 2, 15 and 100 rad/h for Y doped sample SIC-S643

SIC-606 respectively, as shown in the Figure 3.11 and Figure 3.12. Similar recovery in the transmittance and light output was also observed for all $PbWO_4$ samples. Because of this damage and recovery, special attention should be paid to the stability of a $PbWO_4$ calorimeter *in situ*.

3.1.4 Dose rate dependence

If both annihilation(recover) and creation(damage) coexist, the color center density at the equilibrium depends on the dose rate applied. Assuming the annihilation speed of color center i is proportional to a constant a_i(recovery constant in units of hr^{-1}) and its creation speed is proportional to a constant b_i(damage constant in units of kRad^{-1}) and the dose rate (R, the radiation dose rate in units of kRad/hr), the differential change of color center density when both processes coexist can be written

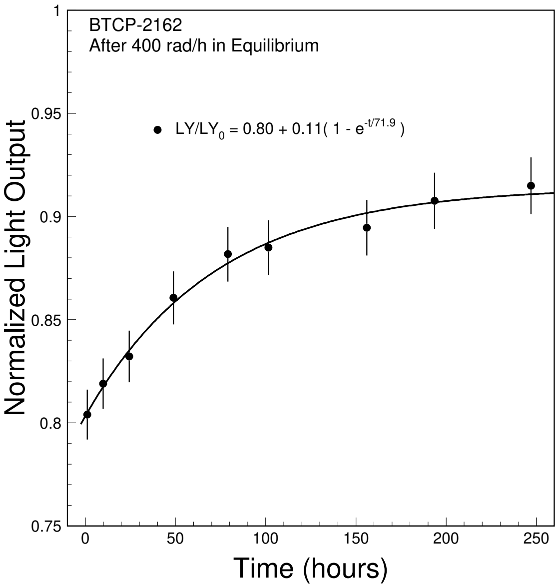

Figure 3.11: Recovery in light output from radiation at room temperature for sample BTCP-2162

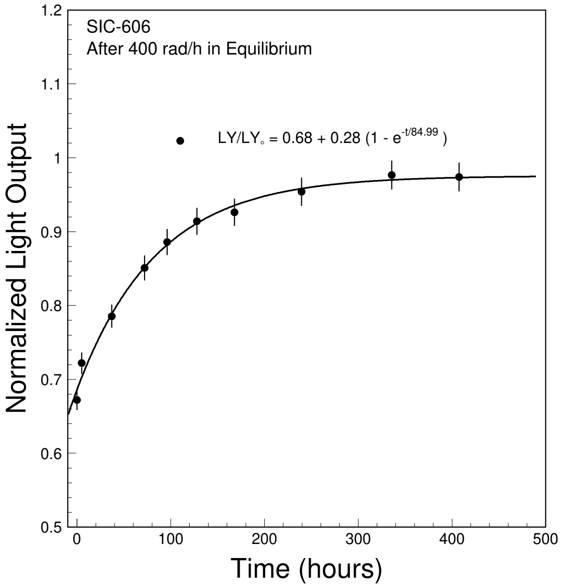

Figure 3.12: Recovery in light output from radiation at room temperature for sample SIC-606

as [48]:

$$dD = \sum_{i=1}^{n}\{-a_iD_i + (D_i^{all} - D_i)\; b_iR\}dt, \tag{3.2}$$

where D_i is the density of the color center i in the crystal in units of m^{-1}, and the summation goes through all centers. The solution of Equation 3.2 is

$$D = \sum_{i=1}^{n}\{\frac{b_iRD_i^{all}}{a_i + b_iR}\;[1 - e^{-(a_i+b_iR)t}] + D_i^0 e^{-(a_i+b_iR)t}\}, \tag{3.3}$$

where D_i^{all} is the total density of the trap related to the center i in the crystal and D_i^0 is its initial density. The color center density in equilibrium (D_{eq}) thus depends on the dose rate (R).

$$D_{eq} = \sum_{i=1}^{n} \frac{b_iRD_i^{all}}{a_i + b_iR}, \tag{3.4}$$

Figure 3.13 shows light output normalized to before irradiation (solid dots with error bars) as function of time for undoped(SIC-167), Sb doped(SIC274), La doped (BTCP-1965), Y/Nb double doped(BTCP-2133), Y/Sb double doped(SIC-S301) and

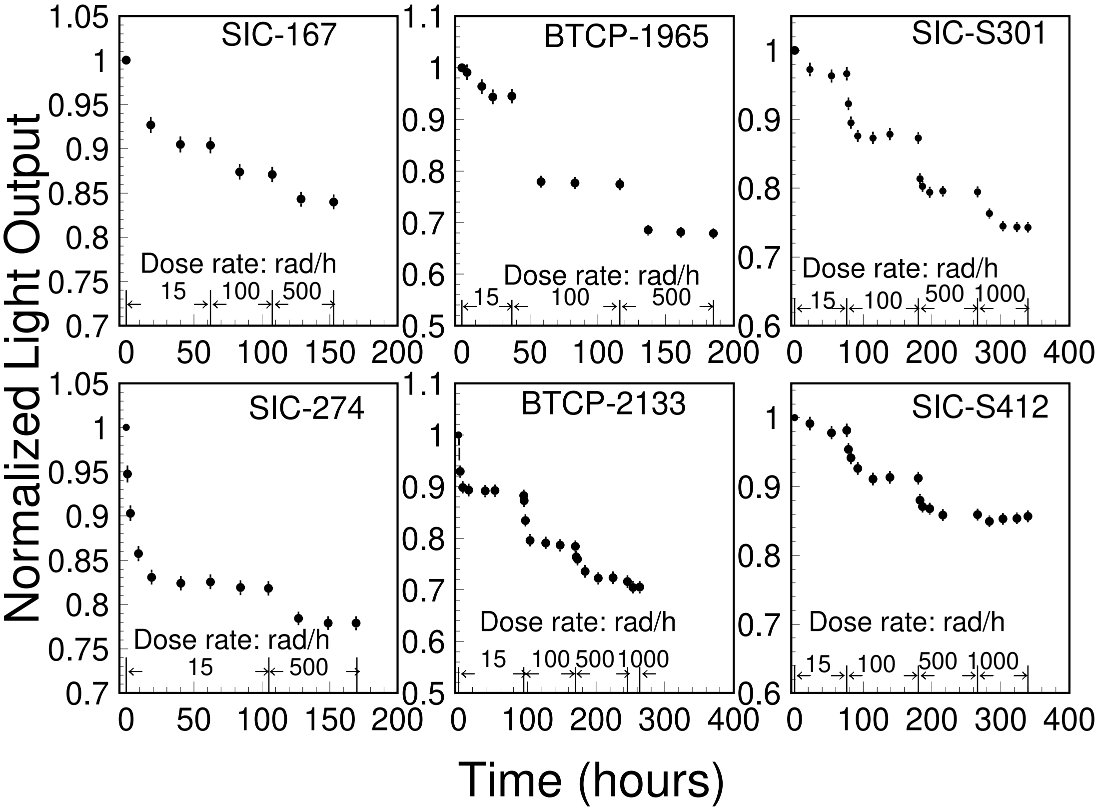

Figure 3.13: The dose rate dependence is shown for $PbWO_4$ samples

Y doped (SIC-S412) samples under lateral irradiation by a ^{60}Co γ-ray source. The dose rate is also shown in the figure. Note, lateral irradiation provides a uniform dose profile of entire body of the sample, so is more severe as compared to front irradiation[60]. Also shown in the figure is the dose rate applied. As shown in the figure, the level of $PbWO_4$ damage is indeed dose rate dependent. The dose rate dependence of light output is clearly observed for all six $PbWO_4$ samples. Because of this dose rate dependence, an adequate radiation hard specification for $PbWO_4$ crystals would refer to a level of light output degradation under a specific dose rate, e.g. 15 rad/h, which is typical dose rate expected at LHC.

If the recovery speed (a) is slow, however, the dose rate dependence would be less important, the color center density in the equilibrium would less depends on the dose rate. The extreme is no dose rate dependence, as shown in Equation 3.5

$$D'_{eq} = \sum_{i=1}^{n} D_i^{all}. \tag{3.5}$$

3.2 Radiation-Induced Phosphorescence

A scintillator can display a long-time luminescence (several microseconds and up) which is called afterglow. The afterglow origin is phosphorescence rising in a crystal due to the thermal release of the carriers from the traps. Photons can be emitted by luminescent centers which are excited by electrons (holes) released from the traps. The traps are formed due to defects and impurities existing in the crystals as well as those created by irradiation. The residual impurities and point defects can form additional centers of luminescence (phosphorescence) in the crystal. The intensity, spectral composition, and decay time of the afterglow depend on the purity of raw material, crystal pulling conditions, heat treatment, and doses of irradiation.

Afterglow is the phenomenon that luminescence can still be observed a long time after the end of the excitation pulse. A long time here is defined as a time much longer than the decay time of the luminescence. Everybody knows this phenomenon from the luminescent lamp that will glows after being switched off. For certain applications the level of afterglow should be negligibly low.

Afterglow is due to the phenomenon that radiant recombination of electrons and holes is sometimes considerably delayed due to trapping of electrons or holes. Excitation with energy above E_g yields free electrons and holes. Let us assume that the holes are trapped by the luminescence centers, whereas the electrons in the conduction band recombine with the holes yielding emission.

However, part of the electrons are trapped in the electron trap center, from where they escape thermally after some time. Only then they recombine with a trapped hole. The corresponding emission occurs with considerable delay and is called afterglow. It will be clear that phosphorescence characterizes a spin-forbidden transition (ΔS=1) which is very slow, whereas afterglow relates to whatever type of emission transition after trapping of an electron or hole elsewhere.

Phosphorescence, that is continued light emission after the end of UV excitation, has been reported[57] with time constants in the range 15 - 127 ms and conjectured to be also due to molybdenum contamination. Excitation of crystals with pulsed UV light source was used to study the time constants in the range up to a few ms[59].

Afterglow refers to the long-term emission of light after irradiation, usually with γ, and we distinguish it from the slow components in the scintillation light because, owing to their long delays, the afterglow photons cannot be associated anymore with a specific incoming particle. Afterglow with a time constant of 12 min has been seen earlier in small undoped $PbWO_4$ samples irradiated at massive dose rates(between 40 and 1000 Gy/h) by counting the number of photoelectrons in a random gate of 100 ns duration[57]. Afterglow has also been reported in [66] by using the anode current measurement method, with two time constants of $\sim$ 6 and 42 min. A similar method, monitoring the anode current from the silicon diode of a Hybrid PhotoMultiplier Tube(HPMT) is described in [108]. Following the observation of an excess of single photoelectrons in the scintillation spectrum of some lead tungstate crystals after irradiation, H.Hofer[109] *et al.* developed a method to determine whether scintillating lead tungstate crystals also respond to γ irradiation with long-term afterglow, in the minutes to hours range. They observed radiation-induced afterglow rates which differ considerably from crystal to crystal, and explained such an effect can be an indication of structural problems in the crystals. Radiation-induced phosphorescence(afterglow) will lead to an increase of readout noise.

3.3 Radiation-Induced Scintillation Mechanism Change

There are a number of possible effects of radiation damage in a scintillating crystal. These include radiation induced absorption (i.e. color center formation), a possible effect on the scintillation mechanism, and radiation induced phosphorescence. Damage to the scintillation mechanism could affect the light yield, while color center formation would affect the light attenuation length of the crystals, and thus the light output observed by the photodetector. Radiation induced phosphorescence could cause additional noise in the readout device.

3.3.1 Damage mechanism in alkali halides

The oxygen contamination is known to cause radiation damage in alkali halide scintillators. In BaF_2[29], for example, hydroxyl (OH^-) may be introduced into crystal through a hydrolysis process, and latter decomposed to interstitial and substitutional centers by radiation through a radiology's process, as shown in Equation 3.6

$$OH^- \rightarrow H_i^0 + O_s^- \quad or \quad H_s^- + O_i^0, \tag{3.6}$$

where subscript i and s refer to interstitial and substitutional centers respectively. Both the O_s^- and the U center (H_s^-) were identified[29].

Following the BaF_2 experience, effort was made to remove oxygen contamination in CsI(Tl) crystals. An approach was taken at SIC: using a scavenger, such as Pb for BaF_2, to remove oxygen contamination. A significant improvement of the radiation hardness was achieved for CsI(Tl) crystals produced taking this approach[104]. It is understood that the function of the scavenger is to form oxide with density less than CsI , so that the oxide will migrate to the top of the ingot during the growing process, similar to the zone-refining process. By doing so, both oxygen and scavenger are removed from the crystal.

Additional analysis was carried out to quantitatively identify the oxygen contamination in CsI(Tl) samples. Figure 13 in[60] shows depth profile of oxygen contamination for two radiation soft and two radiation hard CsI(Tl) samples. Crystals with poor radiation resistance have oxygen contamination higher than that of radiation hard samples. The radiation damage in CsI(Tl) is caused by oxygen contamination.

The scintillation mechanism of CsI(Tl) crystals is not damaged. The degradation of light output is due only to the radiation-induced absorption, i.e. color center formation. This conclusion is drawn based on the following facts[60]:(1) no change in the shape of emission spectrum; (2) no change in the scintillation decay time; and (3) negligible damage in the light response uniformity, if crystal's initial light attenuation length is long enough. The light output degradation of CsI(Tl) after irradiation is not dose rate dependent because the recovery speed of CsI(Tl) at room temperature is very slow, as shown in Figure 8 in[60].

3.4 Lead Tungstate Damage Mechanism

Material characterization, including determination of trace element impurities, defects and structural analysis, can help to provide information on the crystals' radiation damage mechanism. Glow Discharge Mass Spectroscopy (GDMS) was used to search for trace element impurities in $PbWO_4$ samples. However, the GDMS analysis at Charles Evans and Associates found no specific correlations between the detected trace impurities in $PbWO_4$ crystals and crystal's susceptibility to the radiation damage[66]. This indicates an important role of defects in the crystals, such as oxygen vacancies which cannot be determined by GDMS.

Crystal defects, such as oxygen vacancies, is known to cause radiation damage in oxide scintillators. In BGO, for example, three common radiation induced absorption bands at 2.3, 3.0 and 3.8 eV were found in a series of 24 doped samples [51], indicating defect-related color centers, such as oxygen vacancies.

Following the BGO experience, effort was made to reduce oxygen vacancies in $PbWO_4$ crystals. An approach was taken at SIC: oxygen compensation through post-growth thermal annealing in an oxygen-rich atmosphere. Significant improvement of radiation hardness was achieved[60]. $PbWO_4$ samples, which were not annealed, have the worst radiation hardness. Samples annealed in oxygen are more radiation hard than that in air. Samples, which were annealed under the optimized oxygen conditions, are the best.

3.4.1 Oxygen compensation

In order to understand the radiation damage mechanism of $PbWO_4$, three pairs of $PbWO_4$ samples were made by SIC to compare the difference between samples before and after oxygen annealing. Each pair of samples were cut from the same $PbWO_4$ ingot to make sure they had the same growth conditions and were from the same batch of raw material, the only difference is their annealing conditions. These samples were carried out the complete measurements including transmittance, scintillation emission, decay time and light out degradation before and after irradiation. Detail test results can be found in[110]. It indicates that these two group samples have different scintillation mechanisms, it is also confirmed by the results of decay time measurements for these samples. It is clear that the initial transmittance edge of oxygen annealed samples are at the shorter wavelength than that of non-annealed samples. And oxygen annealed samples also have much better transmittance at around 370 nm, which absorption is thought caused by oxygen deficiency. It means oxygen annealing on small samples can successfully compensate the oxygen deficiency inside the $PbWO_4$ crystals.

Summary the oxygen compensation experiment results, some conclusions were made as follows: 1) oxygen annealing changed the scintillation mechanism of $PbWO_4$ crystal. It made $PbWO_4$ scintillation emission peak shift from blue to green. It also enlarged slow component of crystal's emission; 2) the absorption edge of $PbWO_4$ crystal's initial transmittance was shifted to shorter wavelength by oxygen annealing. The initial transmittance at 370 nm was improved by oxygen annealing. It indicates that the initial absorptions at around 370 nm for samples received no annealing were caused by oxygen deficit; 3) the radiation-induced absorptions were reduced by oxygen compensation, the light output degradations were also eased by oxygen annealing. The results confirmed that oxygen deficit worsen the radiation resistance of $PbWO_4$ crystal.

3.4.2 Identification of oxygen vacancies

As discussed above, although significant improvement of radiation hardness of $PbWO_4$ crystals has been observed by oxygen compensation through post-growth thermal annealing in an oxygen-rich atmosphere, a direct observation of oxygen vacancies in the crystal is still expected. Particle-Induced X-ray Emission (PIXE) and quantitative wavelength-dispersive Electron Micro-Probe Analysis (EMPA) for $PbWO_4$ crystals in Charles Evans and Associates was first tried. It was found that crystals with poor radiation hardness were found to have a non-stoichiometric W/Pb ratio[60]. However, both PIXE and EMPA did not provide oxygen analysis.

The direct observe oxygen vacancies requires a measurement of the complete stoichiometric ratio of Pb:W:O in $PbWO_4$ samples. X-ray Photoelectron Spectroscopy (XPS) was tried at Charles Evens & Associates [67]. It, however, was found to be very difficult due to the systematic uncertainty in oxygen analysis. Effort has also be made to directly identify oxygen vacancies by Electron Paramagnetic Resonance (ESR) and Electron-Nuclear Double Resonance (ENDOR) through observing unpaired electrons. It, however, was also difficult to reach a quantitative conclusion.

By using Transmission Electron Microscopy (TEM) coupled to Energy Dispersion Spectrometry (EDS), a localized stoichiometry analysis was possible to identify oxygen vacancies. A localized stoichiometry analysis was carried out at SIC[54] by employing a TEM with EDS system. This analysis clearly identified oxygen vacancies in $PbWO_4$ samples of poor radiation hardness, and confirmed our early conjecture on $PbWO_4$ radiation damage mechanism. So, the radiation damage in oxides is understood to be caused by stoichiometry-related defects, e.g. oxygen vacancies, as evidenced by localized stoichiometry analysis by TEM/EDS, and the effectiveness of the oxygen compensation for $PbWO_4$ crystals[97].

3.5 Summary

Crystal calorimeters in future high-energy colliders will operate in a severe radiation environment caused by the increased center of mass energy and luminosity. Despite much experience and expertise accumulated in the last decade, crystal calorimetry is facing a new challenge. Without stringent quality control, crystals would suffer from significant radiation damage, leading to a degraded performance.

Possible effects of radiation damage in scintillation crystals include (1) radiation induced absorption; (2) radiation-induced phosphorescence, and may be (3) damage in scintillation mechanism. The predominant radiation damage effect in crystal scintillators is the radiation induced absorption, or color center formation, not the loss of scintillation light yield.

It is understood that crystal scintillators for precision calorimetry must preserve their light response uniformity under irradiation, which requires a long enough light attenuation length. With such crystals, a precision light monitoring may function as inter-calibration.

The radiation damage in alkali halides is understood to be caused by the oxygen and/or hydroxyl contamination, as evidenced by the SIMS analysis and the effectiveness of the usage of a scavenger in removing oxygen contamination in CsI(Tl) crystals. The radiation damage in oxides is understood to be caused by stoichiometry-related defects, e.g. oxygen vacancies, as evidenced by localized stoichiometry analysis by TEM/EDS, and effectiveness of the oxygen compensation for $PbWO_4$ crystals.

Chapter 4

Measurement Methods

4.1 Scintillator Emission

The emission spectrum of a scintillator should peak near the maximum quantum efficiency of a Photosensor. The standard photosensor in the scintillator detector is a PMT with a bialkali photocathode and a glass window. The scintillator used in combination with such a PMT should emit at wavelength between 280 and about 500 nm. The use of a quartz or MgF_2 window extends the sensitivity of the PMT with bialkali photocathode to the UV and vacuum ultraviolet (VUV) regions. Another way to detect the scintillation light from a crystal is to use silicon photodiodes[113]. The quantum efficiency of the Si photodiodes is typically 70% between 500 and 900 nm, but it decreases rapidly below 500 nm. It is clear that the highest signal will be detected from scintillation crystals that have an intensive emission above 500 nm with silicon photodiodes.

4.1.1 Photo and radio luminescence

Photo luminescence of $PbWO_4$ was measured by using a Hitachi F-4500 fluorescence spectrophotometer. The Hitachi Model F-4500 fluorescence spectrophotometer is a high-performance spectrophotometer that can be used to measure fluorescence, phosphorescnece, and luminescence in the ultraviolet and the visible regions of the spectrum. A schematic drawing of the optical design of the fluorescence spectrophotometer is shown in Figure 4.1. The optical module of the spectrophotometer is designed

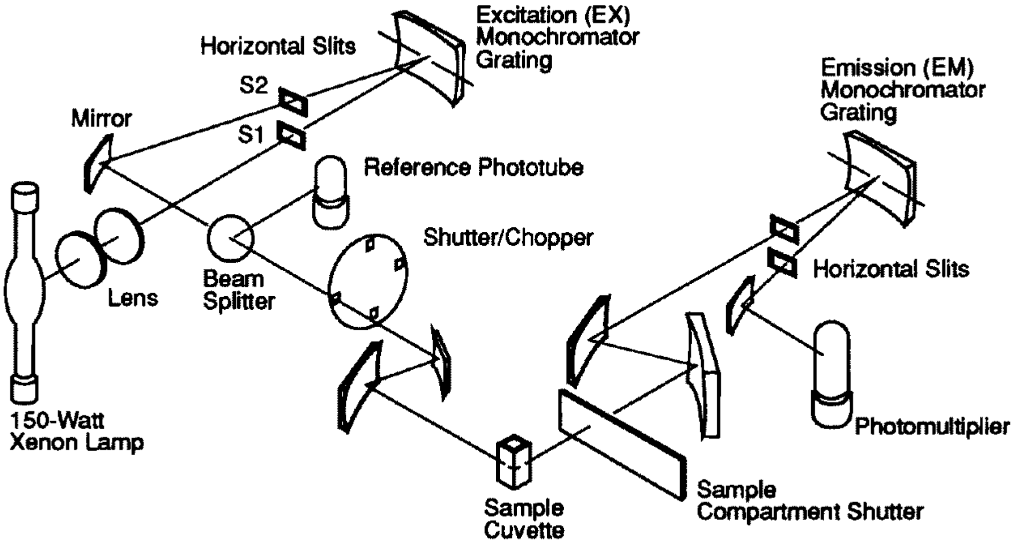

Figure 4.1: F-4500 fluorescence spectrophotometer optics

to maximize sensitivity(as measured by the signal-to-noise ratio), while providing excellent resolution. *A 150-Watt Xenon(Xe) lamp* is used for excitation. The radiation from this lamp is focused on the entrance slit of the excitation (EX) monochromator.

The *EX Monochromator* has a stigmatic concave diffraction grating (900L/mm) blazed at 300 nm. The radiation transmitted by the diffraction grating is focused on the exit slit of the monochromator. The optical design maintains a beam size that is independent of the slit selection.

After the radiation exits from the EX monochromator, it strikes a *Beam Splitter*. A small fraction of the radiation is deflected to the *Reference Phototube*, which monitors the change in the intensity of the lamp as a function of time. The signal from the reference phototube is used to correct the fluorescence intensity for small changes in the lamp output.

A *Shutter/Chopper* is located between the beam splitter and the sample. The shutter/chopper is used as a chopper to measure phosphorescence. It is used as a shutter when the operator wants to protect the sample from photochemical degradation. The optical module has a large *Sample Compartment* to provide easy positioning of large samples.

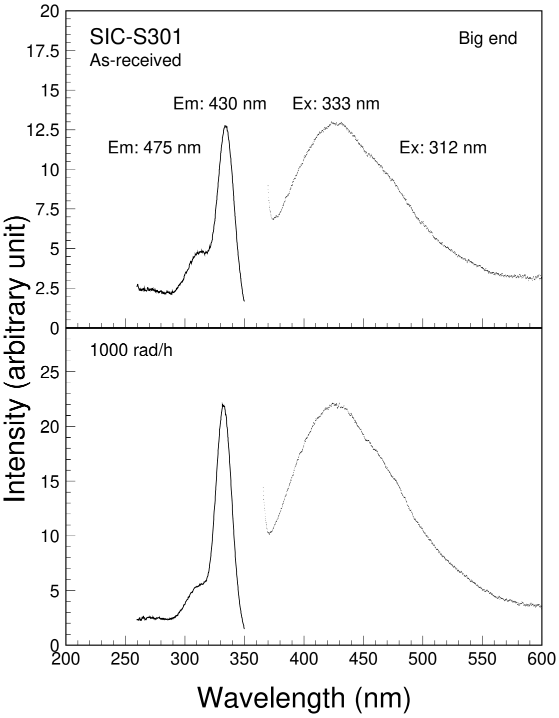

Figure 4.2: The excitation and emission spectra for big end of $PbWO_4$ SIC-S301 measured by Hitachi F-4500 at before and after irradiation

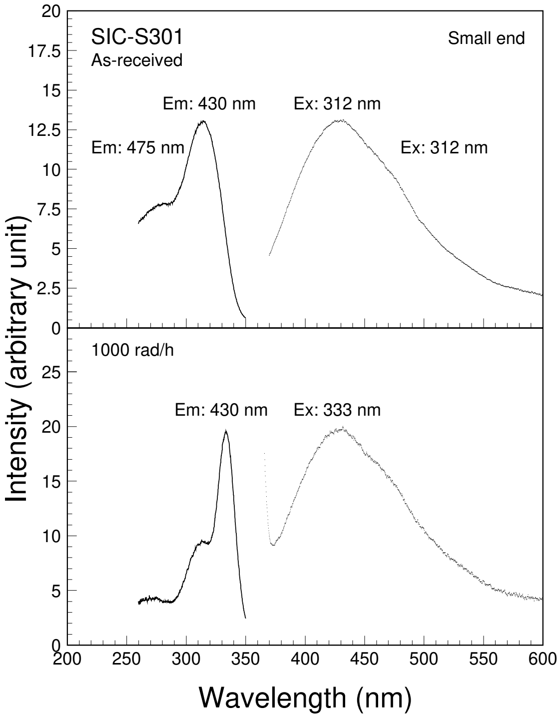

Figure 4.3: The excitation and emission spectra for small end of $PbWO_4$ SIC-S301 measured by Hitachi F-4500 at before and after irradiation

The radiation from the sample compartment is focused on the entrance slit of the *Emission (EM) Monochromator*. The EM monochromator has a stigmatic concave diffraction grating (900 L/mm) blazed at 400 nm. The radiation transmitted by the diffraction grating is focused on the exit slit of the monochromator. The radiation from the EM monochromator is detected by the Photomultiplier. The optical module contains a number of devices that exhibit wavelength-dependent characteristics, e.g., the lamp, the photomultiplier, and the monochromator gratings. The *Instrumental Response* function (special correction factors) can be used to compensate for these effects. The corrected emission and excitation spectrum is within a range of 200 - 600 nm, which is sensitive enough to detect the scintillation emission of $PbWO_4$ samples. Figure 4.2 and Figure 4.3 show the excitation and emission spectra of a $PbWO_4$ sample SIC-S301. The sample was excited by 310 nm and its emission peak is at 430 nm.

A schematic of the measurement setup for photo luminescence is shown in Figure 4.4, where UV excitation light was shot to a bare surface of the sample and the photo luminescence, without passing through sample, was measured by a photo multiplier tube (PMT) through a monochromator. The setup used to measure radio luminescence is shown in Figure 4.5, where whole body of a wrapped sample was irradiated by a ^{60}Co γ-ray source at a dose rate of about 1,000 rad/h, and the radio luminescence, passing through sample, was focused and measured.

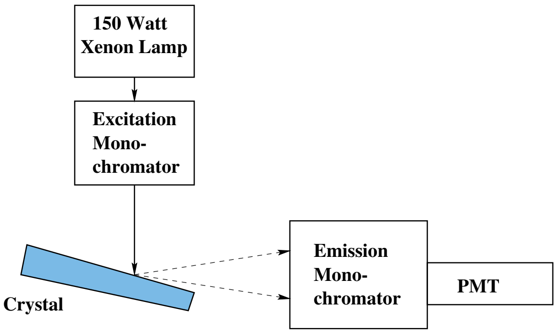

Figure 4.4: A schematic of setup used to measure photo luminescence

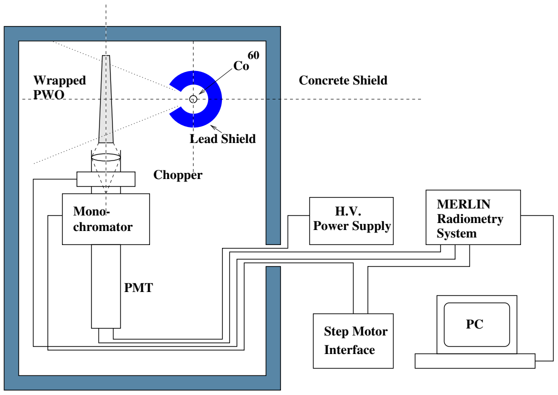

Figure 4.5: A schematic of setup used to measure radio luminescence

4.1.2 Phosphorescence

The radiation induced phosphorescence was determined by measuring the light output from the crystal shortly after irradiation with no further external excitation applied. Irradiations were carried out at a dose rate (400 rad/h) corresponding to the typical dose rate expected at the LHC (500 rad/h) for cumulative dose of 36 krad. The light output was measured by placing a Phillips XP2020 PMT immediately in front of the crystal and recording the phototube current as a function of time after irradiation. For measurements starting approximately 5 min after irradiation, the phototube current never exceeded approximately 1 μA (800 nA) at a phototube voltage of 2400 V. However, care had to be taken to prevent the phototube from being exposed to excessively high currents during irradiation. Therefore, the high voltage was kept off during irradiation, and was raised to 2400V within a few seconds after irradiation to measure the current due to the phosphorescence. Under these conditions, the current in the phototube produced by light from the crystal, which was wrapped in white reflecting Tyvek, never exceeded approximately 1 μA(800 nA). The current produced in the phototube alone under the same conditions was less than 70 nA.

4.2 Optical Transmittance

4.2.1 Longitudinal transmittance and light attenuation length

The main optical characteristics of a scintillator are transmission and index of refraction. In most applications, the scintillator should transmit its own emitted light. The portion of absorbed light, as well as γ-rays, is determined by the absorption coefficient of the material and path of light beam. The path of light beam can significantly exceed the length of the crystal due to the repeated reflections of light from the inside surfaces of the scintillator, other than that adjacent to the photomultiplier tube (PMT) photocathode. It is desired that a large fraction of the photons emitted by the luminescence centers in the scintillator be collected at the cathode of the photomultiplier (or at another photodetector)[113].

The emitted light can be absorbed by impurities and defects (background absorption) as well as by the host crystal(reabsorption). The level of reabsorption depends on physical characteristics of the compound like band-gap width and properties of the activator. This type of absorption can hardly be decreased. The level of the impurity absorption depends on the concentration of residual impurities and point defects. Therefore the transmission of a crystal is dictated by purity of the raw materials and conditions of the crystal growth. The transmission can vary along the length of the crystal due to a nonuniform concentration of impurities within the crystal resulting from growth methods which tend to concentrate the impurities in a particular region of the ingot. In this case, the large crystal may have a higher concentration of residual impurities at one end than the other. This can affect the energy resolution of the detector.

The transmission of a crystal can also be reduced due to bulk light scattering. The bulk scattering is caused by a small interposition with a refractive index differing from one of the host crystals. The scattering centers can be created as a phase interposition of host or impurity crystalline areas. When the dimensions of the interposition exceed 0.1 to 0.5 μm, the light scattering adds to bulk absorption of the material. In this case, the transmission of the crystal is determined by an extinction coefficient which is equal to the sum of the absorption and light scattering coefficients. It is important to note that the crystal with light scattering centers also have a low radiation hardness. The light collection efficiency of the scintillator with specific dimensions depends on the optical properties of the crystal. Bulk absorption and bulk scattering of scintillation photons reduce the light collection efficiency.

Another important characteristic of the optical properties of a scintillator is a crystal index of refraction n. The optical matching of scintillator and photosensor is required, otherwise part of the light will reflected at the scintillator-detector interface. The windows of the conventional photomultiplier are made from a glass with $n_w \approx 1.5$. Usually a scintillator is matched to the glass or quartz window of a photomultiplier by means of a silicon compound. The condition $n_{sc}(\lambda) \leq n_w(\lambda)$ should be met in order for all light to enter the photocathode (n_{sc} is the refractive index of the scintillator). Traveling a long distance as a result of repeated reflections inside the scintillator, the light reaches the photocathode with some delay. This increases the duration of scintillation pulse.

One very important parameter which is relatively easy to measure and strongly correlated with the optical and radiation-hardness properties of the crystal is the optical transmission spectrum. The longitudinal measurement through the 23-cm-long $PbWO_4$ crystal allows the detection of even weak absorption bands which give a good indication about the light yield and radiation hardness of the crystal. Particularly important is the control of the sharpness of the optical transmission edges and the absence of the 420 nm absorption band. The transverse measurement at different points along the crystal also gives the longitudinal uniformity of the optical parameters of the crystal.

The transparency of the crystal is only indirectly connected to the calorimeter performances: the light transmission, in fact, is required to exceed a minimum value in order to have a good light collection uniformity and sufficient light yield. Nevertheless the crystal transmission is simple to measure and is useful for crystal production specifications. Longitudinal transmission is used to detect possible wide absorption bands and to determine the light attenuation length of the scintillation spectrum. This parameter is useful for the uniformization of the light collection efficiency of the scintillation elements.

Longitudinal transmission spectrum provides data for the calculation of absorption attenuation length at any wavelength from the selected region. It shows the short wavelength cut-off of the spectrum that brings information about possible defects and impurities present in the crystal. However, the data obtained from such a measurement do not contain any information about the non-uniformity of the crystal transmission along the crystal axis. Furthermore, this method does not allow defects in the crystal such as bubble corners or other scatters, which sometimes exits in the initial or tail part of the crystal, to be identified.

The longitudinal transmittance of each $PbWO_4$ sample was measured using a Hitachi U-3210 UV/Visible double beam, double monochromator spectrophotome-

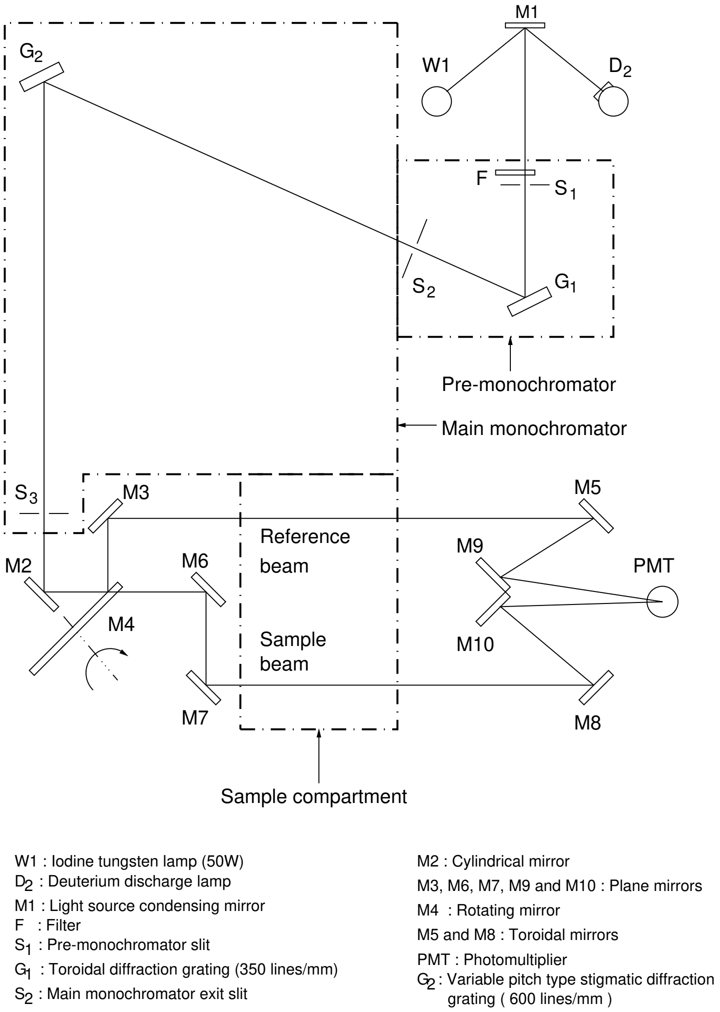

Figure 4.6: Optical layout of model U-3210

ter equipped with a large sample compartment, including a custom Halon coated integrating sphere. The optical layout of U-3210 is shown in Figure 4.6. The systematic uncertainty in repeated measurements of transmittance was approximately 0.3%. However, the uncertainty in measurements made by repeatedly placing and removing crystals in the test stand inside the large sample compartment was about 0.5%.

For $PbWO_4$ crystals, additional uncertainties in the transmittance measurements arise because of its birefringent nature[1], and due to macroscopic defects, such as voids

---

[1] The C axis of the crystal is at about 19° to the crystal axis, according to the manufacturer.

and scattering centers, in the crystal. The uncertainty due to the birefringence was determined to be less than 10% for different azimuthal orientations of the crystal. To avoid this effect, a particular azimuthal orientation was chosen for each sample which gave the maximum longitudinal transmittance. The second uncertainty was less important in our measurements, since the integrating sphere in the large sample compartment collected almost all light passing through the sample.

The light attenuation length (λ) is an important parameter in evaluating the quality of crystals [29]. An approximated formula, Equation 5 of reference [29], was suggested by one of the authors to calculate the light attenuation length of a BaF_2 crystal by use of its measured transmittance (T) and an ideal theoretical transmittance (T_s) which takes care of the loss at two surfaces of the crystal:

$$\lambda = \frac{\ell}{\ln(T_s/T)} \tag{4.1}$$

where ℓ is the path length, i.e. the crystal length.

However, this equation suffers a approximation: the equation does not take into account multiple bounces between two end surfaces of the crystal. Then the light attenuation length calculated by using Equation 4.1 is not accurate.

As defined above, T_s is an ideal transmittance of a crystal with infinite light attenuation length and two parallel end surfaces. The loss of light in each surface can be calculated by using Fresnel's law:

$$R = \frac{(n - n_{air})^2}{(n + n_{air})^2} \tag{4.2}$$

where n and n_{air} are the refractive index of crystal and air which are function of the wavelength.

Taking into account multiple bounces between two end surfaces, the ideal transmittance (T_s) can be written as

$$\begin{aligned} T_s &= (1-R)^2 + R^2(1-R)^2 + ... \\ &= (1-R)/(1+R) \end{aligned} \tag{4.3}$$

Assuming the crystal has a light attenuation length of λ, which is also a function of wavelength, the light intensity after traversing a path length of ℓ is:

$$L = e^{-\ell/\lambda} \tag{4.4}$$

Taking into account both multiple bounces between two end surfaces and light attenuation loss, the real transmittance (T) measured can be written as

$$\begin{aligned} T &= (1-R)^2 L + R^2\ (1-R)^2 L^3 + ... \\ &= \frac{L\ (1-R)^2}{1-L^2R^2} \end{aligned} \tag{4.5}$$

Equation 4.5 can be written as

$$TR^2L^2 + (1-R)^2L - T = 0 \tag{4.6}$$

which can be solved with a solution of

$$L = \frac{\sqrt{4T_s^4 + T^2(1-T_s^2)^2} - 2T_s^2}{T(1-T_s)^2} \tag{4.7}$$

where Equation 4.3 is used.

Using Equation 4.4, we thus have an accurate formula which can be used to calculate the light attenuation length (λ) by using measured transmittance (T):

$$\lambda = \frac{\ell}{\ln\{[T(1-T_s)^2]/[\sqrt{4T_s^4 + T^2(1-T_s^2)^2} - 2T_s^2]\}} \tag{4.8}$$

Note, in case T_s close to 1, the Equation 4.8 can be approximated to Equation 4.1.

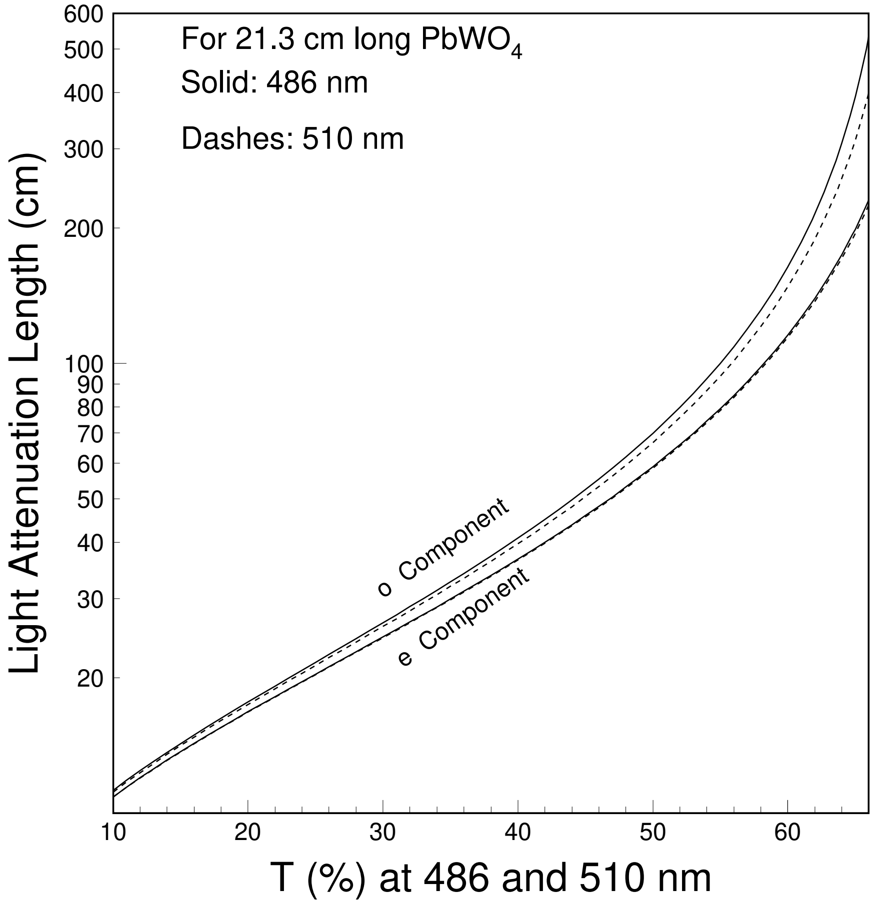

Figure 4.7: The light attenuation length at 486 and 510 nm, as a function of the measured longitudinal transmittance for 21.3 cm long $PbWO_4$crystals. The solid (dashed) curves are for 480 (510) nm. The upper bound corresponds to the refractive index of the ordinary (*o*) polarization component while the lower bound corresponds to the extraordinary (*e*) polarization component[112]

Using existing $PbWO_4$ refractive index data [112], Figure 4.7 shows the light attenuation length at 486 and 510 nm, as a function of the measured longitudinal transmittance for a 21.3 cm long $PbWO_4$ crystal. While the exact refractive index of

$PbWO_4$ at 486 nm was taken from reference [112], the refractive index at 510 nm was determined by interpolation. The solid and dashed lines in the figure are for 486 and 510 nm respectively. The upper and lower bounds correspond to the refractive index of the ordinary (*o*) and extraordinary (*e*) polarization components [112]. Because of the choice of the azimuthal orientation in the longitudinal transmittance measurement, the *e* component curves were used to determine the light attenuation length.

Theoretically, absorption (A), or optical density (D), is more adequate to describe quality of crystals, since they are linearly related to the color center density, or the cross section of light absorption. They are defined as:

$$A \ or \ D = \log(1/T) = -\log T \tag{4.9}$$

By using approximate Equation 4.1, one has

$$\lambda = \frac{0.43 \ \ell}{A - \log(1/T_s)} \tag{4.10}$$

4.2.2 Transversal transmittance

The transversal transmission spectra are measured at several points along the crystal axis. These data are necessary in order to check transmission non-uniformity which may be caused by growth technology deviations or quality of the raw materials. The main reason to do this measurement is to identify radiation hardness crystals. It is in fact noted that most of the radiation hard crystals have a steep band edge in the region 330 - 350 nm. Unfortunately no model can predict the the minimum slope of the ban edge for crystals in order to be radiation hard. The only way to set a limit is to use empirical criteria. G. Basti *et al.*used data from the last crystal samples delivered at CERN to extract the slopes of their band edges (fitted with a straight line in the region 330 - 350 nm)[114]. They have an average value of 2.76 %/nm with a σ of 0.19%/nm.

The transversal transmission measurement can provide information about the non-uniformity of the transmission and additional information necessary to uniformize crystal light collection with APD, using light yield non-uniformity data obtained with PMT readout. In principle, longitudinal transmission can also be reconstructed using transversal transmission data[115].

4.3 Light Output Measurement

4.3.1 Readout devices

The essential feature required of any scintillator is to be an effective converter of ionizing radiation to visible light. The conversion or energy efficiency η of a sintilllator may be written as:

$$\eta = \frac{\langle h\nu_r \rangle N_{ph}}{E_\gamma} \tag{4.11}$$

where N_{ph} is the total number of photons emitted upon interaction with a gamma quantum of energy E_γ or with other ionizing radiation, $\langle h\nu_r \rangle$ is mean energy of emitted photons. The energy efficiency ν is a physical characteristic of a scintillator which is important for the integrating regime of detector work. For scintillation counting, the *relative light output* or scintillation yield L_R is a more significant quantity than ν. L_R is the number of the emitted photons per unit of absorbed energy (usually 1 MeV):

$$L_R = \frac{N_{ph}}{E_\gamma} \tag{4.12}$$

Determination of the absolute scintillation yield requires an accounting of the light collection efficiency and a quantum efficiency of the photosensor.

The scintillation light yield at room temperature (20°C) for $PbWO_4$ was measured using a Hamamatsu photomultiplier tube (R2059 PMT) which has a bialkali photocathode and quartz window. A collimated γ-ray source ^{137}Cs was used to excite the sample. One end of the crystal was coupled to the PMT with Dow Corning 200 silicone fluid. All other surfaces of the crystal were wrapped with two layers of Tyvek paper in order to increase the collected light.

The gain or current amplification for R2059 PMT is around 10^7. The anode pulse signal is first split, one-half of the signal goes through a delay cable to a q-input of a qvt multichannel analyzer(LeCroy 3001), whereas the other half goes to a threshhold discriminator (LeCroy 821), which delivers a standard logic signal for every analog signal with an amplitude higher than the threshold. The logic signal was then fed into a scalar and into a Camac-controlled precision gate generator (LeCroy 2323a) which defines the charge integrating time, usually 200 ns; the discriminator is set so that the valley below the single photoelectron peak is visible. The scintillation spectra usually show one, two and sometimes three photoelectrons peaks, allowing absolute calibration. Each spectrum shows a peak corresponding to the absorption of the photons in $PbWO_4$ and a continuum produced by Compton interactions. The peak position gives the absolute light yield in p.e./MeV once the calibration in ADC channels per photoelectron is given.

The ADC data are accumulated into a 1024 channels histogram. Analysis consists in pedestal verification and a fit to determine the position of the photoelectric peak from the calibration source.

The gate signal was used to external trigger the qvt multichannel analyzer(LeCroy 3001). Here the LeCroy 3001 is a multichannel analyzer that can histogram any one of three parameters: charge(area), voltage(peak), and time(start/stop). The Q mode is intended for analysis of photomultiplier anode signals without amplifying or shaping. Analog-to-digital convection is performed on the quantity of charge received at the Q-Input within a well defined time interval. A gate pulse activates a linear gate and allows the current at the q-Input to be integrate on a capacitor. Thus the analog "pulse height" is stored for ADC.

The 10-bit ADC used for the q(charge) mode has a sensitivity of 0.25 pC/channel, directly compatible with photomultiplier anodes pulses, thus obviating the need for a charge-sensitive preamplifier. The discriminator(LeCroy 821) served the purpose of excluding low level electronic noise. The threshold should be carefully adjusted so as to ensure that electronic noise is eliminated, but not so high as to also cut out good signals.

4.3.2 Determination of photoelectron numbers

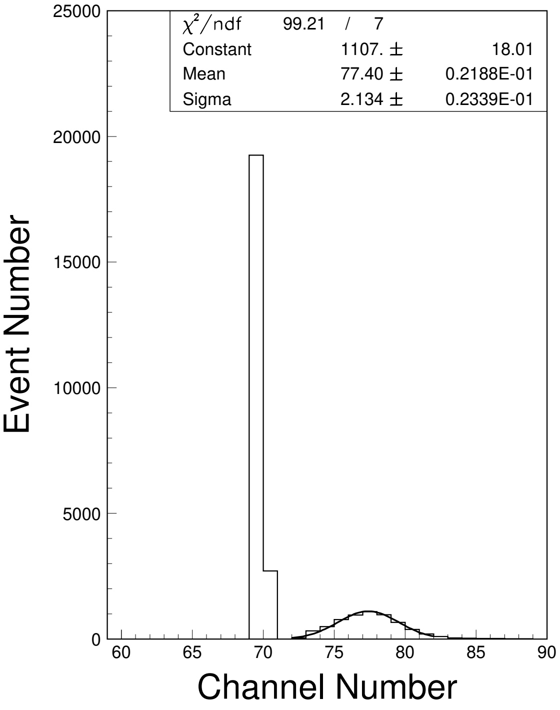

Figure 4.8: Spectra of pedestal and single photoelectron

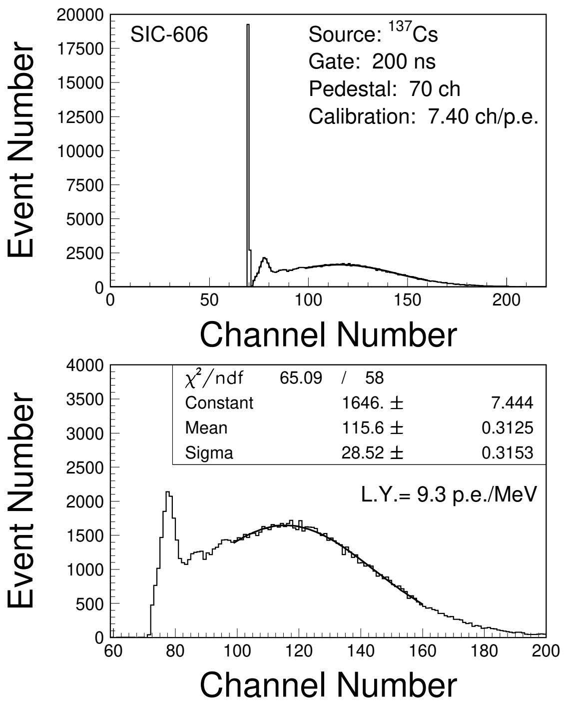

Figure 4.9: A ^{137}Cs spectrum as seen by a PbWO$_4$ crystal SIC-606

The photoelectron numbers, corresponding to the γ-ray peak, was determined by the peak ADC channel obtained by a Gaussian fit(not including the Compton edge), times a calibration constant corresponding to the number of photoelectrons per ADC channel. The calibration was obtained by using the single photoelectron peak, again from a Gaussian fit, and was cross-checked with an LED calibration, taking into account the intrinsic width of the single photoelectron spectrum:

$$photoelectron\ number = [1 + (\sigma_{spe}/Peak_{spe})^2](Peak_{LED}/\sigma_{LED})^2 \tag{4.13}$$

where, $Peak$ and σ are the peak and width from a Gaussian fit, and the subscripts LED and spe refer to the distributions of LED and single photoelectron spectra, respectively.

The spectra of pedestal and single photoelectron for PMT tube R2059 are shown in the Figure 4.8. The pedestal is the channel number obtained when a gate pulse is applied with a no analog input. Here the gate duration is 200 ns, and the HV(high voltage) supplied on PMT is 2100 V. Figure 4.9 shows the ^{137}Cs γ-ray pulse height spectrum collected from $PbWO_4$ crystal SIC-606 for a gate of 200 ns. The up-right corner of Figure 4.8 and Figure 4.9 show the results of Gaussian fit carried on the peak of single photoelectron and the γ-ray spectrum of $PbWO_4$ crystal SIC-606 respectively.

4.3.3 Temperature corrections

In most applications, the scintillators are used at room temperature. During the operation the temperature of the detector can vary slightly due to irradiation or change of ambient conditions. The change of scintillator light yield with temperature leads to a change of the output signal of the detector. The thermal stability of the scintillation yield is needed for proper operation of the detector. For a linear detector response, the light output of scintillator crystals should be stable within the operating temperature range. The stability is characterized by the temperature coefficient of the light output

$$\alpha_T = \frac{L - L_0}{L_0(T - 300)} \tag{4.14}$$

where L_0 is light output of the scintillator at 300 K. NaI(Tl)(α_T = 0.22 to 0.95

%/K), CsI(Tl) and CsI(Na)(α_T = 0.24 to 0.67 %/K) have positive temperature coefficients, while crystals BGO (α_T = -1.5 to -1.7 %/K), CsI, and BaF_2 have negative ones[113]. The thermal quenching causes a reduction in intensity and also in decay time of luminescence.

It is of note that the measurements of the scintillation yield, i.e., essentially the output pulse height of the detector, do not account for the variation of decay time and emission spectrum with temperature. Recently, the temperature dependencies of the absolute scintillation yield have been measured by special techniques, the shaped square wave method and the current mode method[116].

The thermal quenching of the scintillation mechanism of $PbWO_4$ leads to a rather strong temperature dependence of the light emission, of typically -1.98 %/°C at room temperature[56]. The temperature coefficient of the $PbWO_4$ crystals, and of the APD, implies that the temperature of the calorimeter must be stabilized to a tenth of a degree[10].

Studies had shown that there were spontaneous recovery process of induced absorption at room temperature for $PbWO_4$ crystals, which are related to the stability of radiation induced color centers, i.e. to the thermal depth of related trapping centers. For the light yield and transmission measurement at Caltech, after $PbWO_4$ crystals being irradiated for a certain period of time under a certain dose rate, the crystals were brought out from the irradiation room into the measurement lab to test their light yield, uniformity and transmission, it took about 10 to 15 minutes before starting these tests. Since the temperature inside the measurement lab is different from that of the irradiation isotope lab, during this transporting process, the temperature of the crystal is always changing, it thus need to know the temperature corrections on the light output as a function of time to obviating the uncertainties resulting from the effect of spontaneous recovery process at room temperature on the light output of $PbWO_4$.

Figure 4.10 and Figure 4.11 show the temperature corrections on the light output

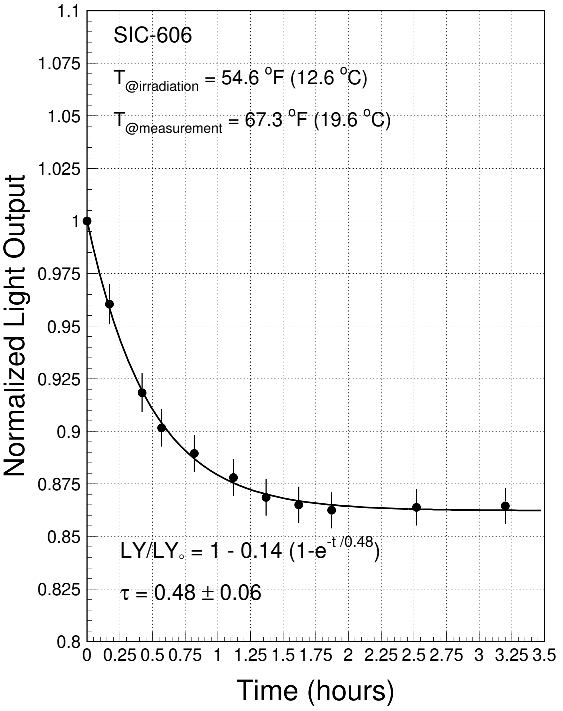

Figure 4.10: Temperature dependence and correction for $PbWO_4$ light yield of SIC-606

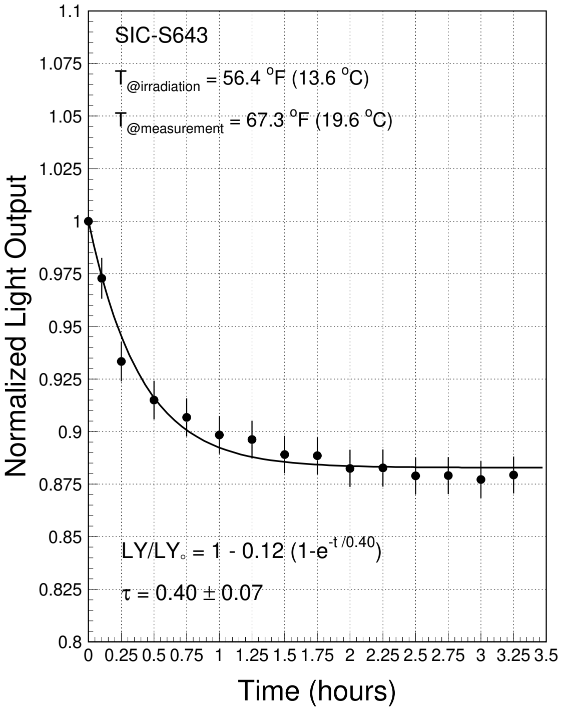

Figure 4.11: Temperature dependence and correction for $PbWO_4$ light yield of SIC-S643

measurement as a function of time measured with R2059 PMT at Caltech. From figures, it can be seen that the temperature difference for the irradiation isotope lab and measurement lab is 11 - 13°C. When the crystals was brought into the measurement lab from outside, it took at least 2 hours to thermalize with respect to the room temperature, as shown in the Figure 4.10 and Figure 4.11.

For every run of testing, temperatures inside the irradiation isotope lab and measurement lab as well as the time interval from switching off the irradiation source to the very beginning of the test were recorded, we thus can perform the temperature corrections on the light output for $PbWO_4$ crystals accordingly.

All measurement were carried out at the room temperature of 20°C. Date were corrected by using the room temperature which has daily variations of up to 0.5°C, despite central air condition of entire building and individual temperature adjustment

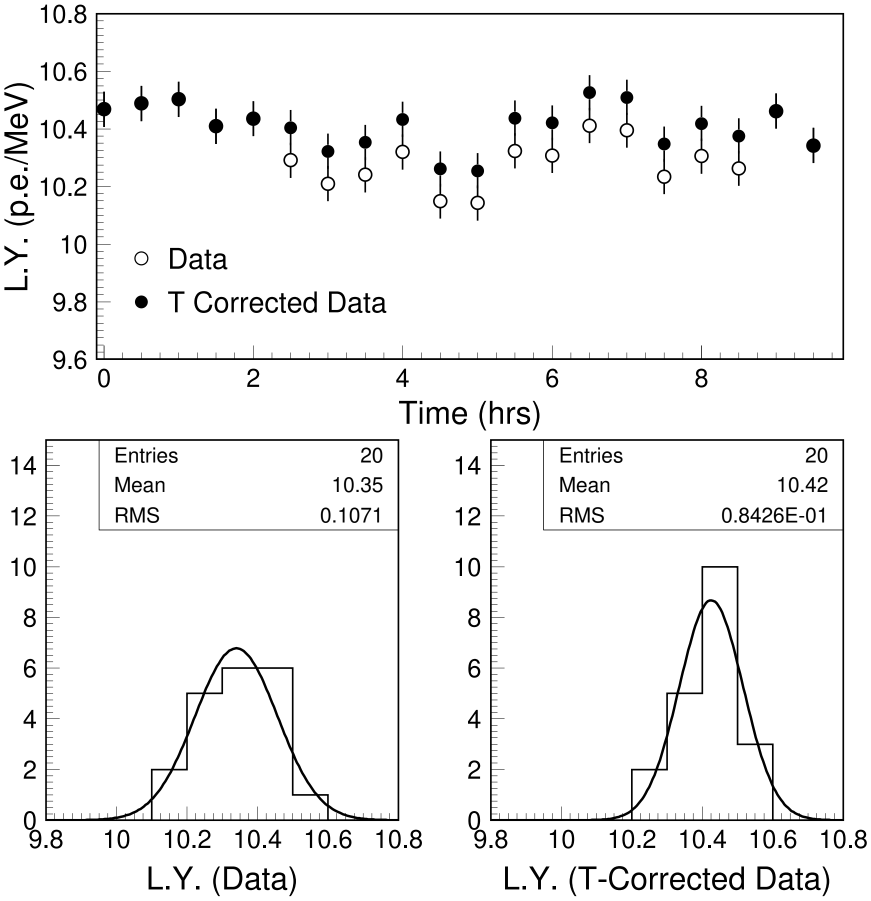

Figure 4.12: Light output measured by a PMT in 9 hours (top), and its distribution without (left bottom) and with (right bottom) temperature corrections

and feedback in the laboratory where measurement was carried out. This variation is significant since the light output of $PbWO_4$ crystal is know to have -1.98 %/°C at the room temperature. The systematic uncertainties of the light output measurement, including the temperature variation and the operation uncertainties caused by mounting samples to the PMT, were estimated to be about 1%. The top plot in Figure 4.12 shows the repeated measurement of the light output for a sample in 9 hours. Two bottom plots in Figure 4.12 show raw (left) and temperature corrected (right) light output data and corresponding Gaussian fit. A precision of 1 and 0.8% were achieved for the light output measurement without and with temperature corrections respectively.

4.4 Decay Kinetics

The decay constants of the the scintillation light were measured using two independent methods: (1) an integration method and (2) a single photon counting method. In the integration method, the photoelectron yield was measured as a function of integration gate width up to 4μs and the result was characterized as

$$LY/LY_{tot} = F + S_1(1 - e^{-t/\tau_1}) + S_2(1 - e^{-t/\tau_2}), \tag{4.15}$$

where LY_{tot} is the total light yield obtained from the fit, and F, S_1 and S_2 are the normalized amplitudes of a fast component with a decay time constant of less than $\sim$ 10 ns, and two slow components with decay time constants of τ_1 and τ_2 respectively. The normalization was done such that

$$F + S_1 + S_2 \equiv 1. \tag{4.16}$$

Figure 4.13 and Figure 4.14 show the data of latest two Y doped $PbWO_4$ for the light yield and decay time measurements determined by using the integral method. The light yield as a function of integration time was fit to the parameterization given in Eq. 4.15 and the results are shown in the figure.

In the single photon counting method, coincident γ-rays from a ^{60}Co source were used to measure the decay time distribution of single photoelectrons produced by the scintillation light in the crystal. The distribution was measured relative to a fast start signal which was provided by a 1” diameter. BaF_2 crystal coupled to a Hamamatsu R5023 PMT which had rise time of 0.6 ns. The stop signal was provided by a Hamamatsu R2059 PMT which was weakly coupled to the $PbWO_4$ sample in

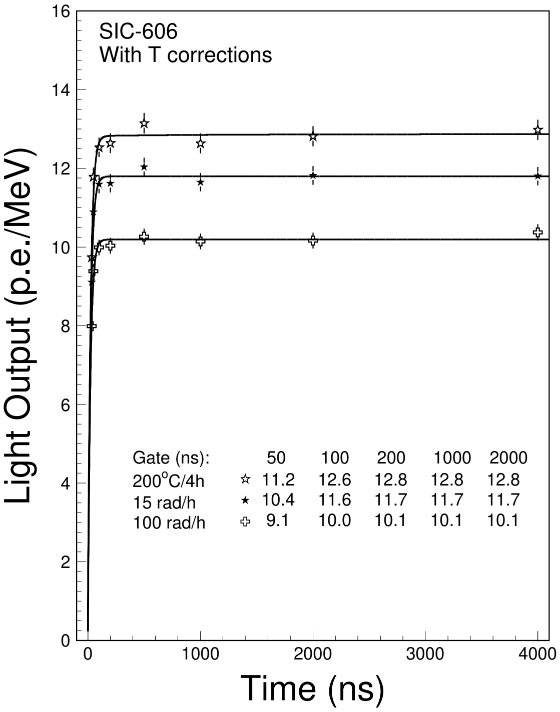

Figure 4.13: The light yield of SIC-606 as a function of integration time

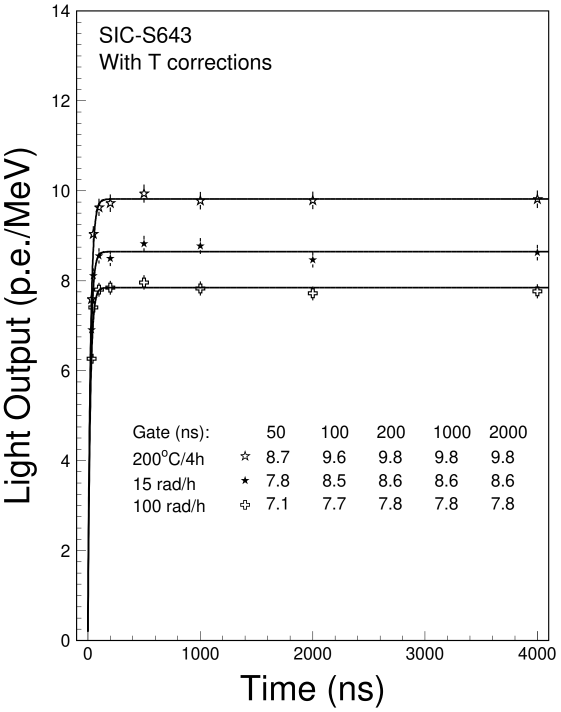

Figure 4.14: The light yield of SIC-S643 as a function of integration time

such a way that the average number of photoelectrons per gamma ray interaction was very small ($\ll 1$). The decay times were measured out to 512 ns using a LeCroy 2228A TDC which had a resolution of 250 ps/channel. The resulting time distribution, after the start peak, was characterized as

$$c_{norm}[S_a/\tau_a e^{-t/\tau_a} + S_b/\tau_b e^{-t/\tau_b} + S_c/\tau_c e^{-t/\tau_c}] \tag{4.17}$$

where S_a, S_b and S_c are the normalized amplitudes of the three decay components with time constants of τ_a, τ_b and τ_c respectively, and c_{norm} is an overall normalization factor.

It should noted that, because of the different time region in these two measurements, the time constants and relative amplitudes determined by the differential and integral methods do not directly correspond with each other. The single photon counting method is best suited to determine the short decay time components (<30 ns), but can give a poor estimate of the amplitude of the longer decay times if either the average number of photoelectrons is too large, which can result in underestimating the amplitude of the slow components, or because of poor statistics if the average number of photoelectrons is too small. On the other hand, the integration method cannot accurately measure the short decay times because of the need to provide a minimum gate length for the ADC, but gives the best measure of the very long decay time components. The two methods do agree in both the amplitudes and the decay times if two measurements were carried out in an identical time region. Therefore, they complement each other by providing the best accuracy in measuring the two different regions of the spectrum. However, it should be emphasized that in both cases, the fits are simply parameterizations of the data which are not unique, and do not necessarily represent the true decay times of the scintillation components in the crystal.

4.5 Light Response Uniformity

The light response uniformity was measured by moving a collimated γ-ray source along the crystal at different longitudinal positions and the result was fit to a linear function:

$$LY/LY_{mid} = 1 + \delta(x - x_{mid})/x_{mid}, \tag{4.18}$$

where x is the distance from the small end, LY_{mid} is the fit value of the light yield at the middle of the crystal, x_{mid}, and δ is a measure of the light response uniformity. Figure 3.6 shows light response uniformity definition.

Because of the non-uniform dose profile in crystals, caused by energy deposition of particles in experiment, a damage to the scintillation mechanism would cause a distortion of the light response uniformity and thus irrecoverable degradation of energy resolution. The radiation-induced absorption, however, may or may not cause

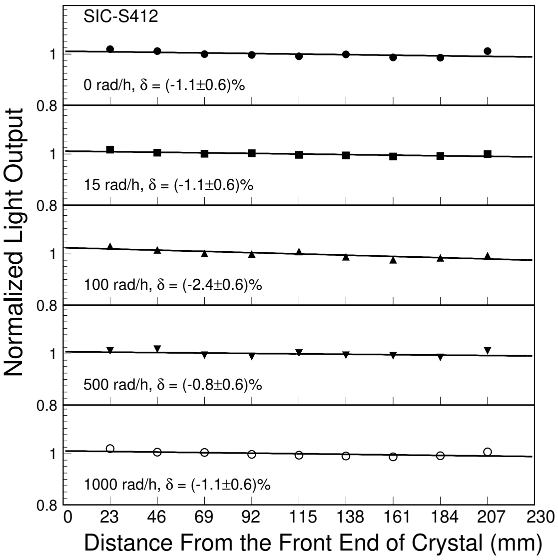

Figure 4.15: The light response uniformities are shown as a function of integrated dose for a full size $PbWO_4$ crystal SIC-S412

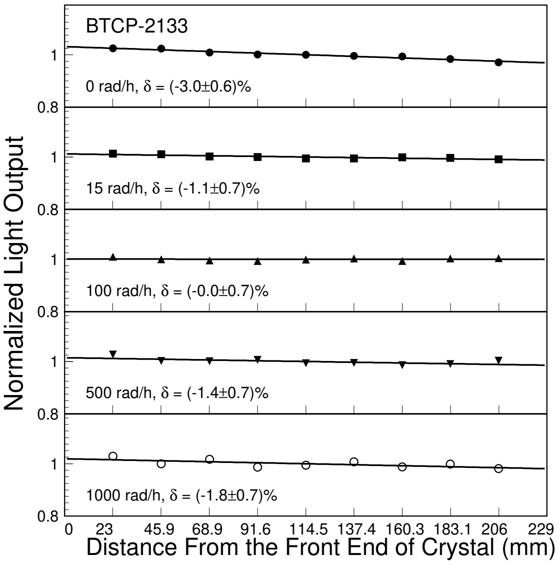

Figure 4.16: The light response uniformities are shown as a function of integrated dose for a full size $PbWO_4$ crystal BTCP-2133

a severe distortion of the light response uniformity.

Figure 4.16 and Figure 4.15 show the light response uniformity as a function of accumulated dose for full size $PbWO_4$ crystals. The pulse heights measured in nine points evenly distributed along the longitudinal axis of the full size $PbWO_4$ crystal is fit to Eq. 4.18. The results confirm that the $PbWO_4$ scintillation mechanism is not damaged, all the δ value is less than 3%, and thus a light attenuation length (LAL) of longer than 95 cm is expected.

4.6 Irradiation Facilities

The gamma ray irradiations were carried out at two different irradiation facilities. The first, as shown in Figure 4.17, was the isotope lab at Caltech. It was equipped with an approximately 50 Ci ^{60}Co source with remote control during the investigation. The crystal samples, wrapped with aluminum foil, were placed at a fixed distance on

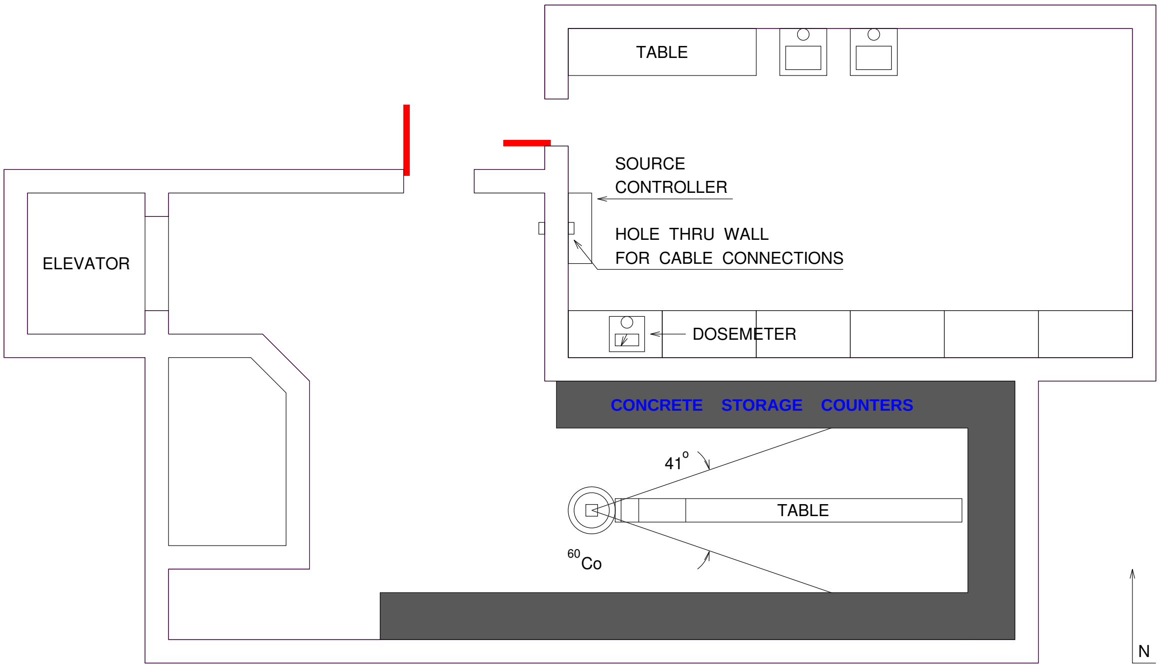

Figure 4.17: The layout of the Caltech low dose irradiation facility

the table in order to obtain a well defined dose rate within a fixed time, i.e. 15, 100, 500 and 1,000 rad/h, as illustrated in the figure. The dose rate was calibrated using a MDH 2025 Monitor with air-equivalent ion chambers which had an accuracy of 5%. This facility was mainly used to carry out the high dose rate irradiation on $PbWO_4$ samples. Another irradiation facilities was a 0.5 Ci ^{137}Cs source used for testing small samples at Caltech.

Chapter 5

Sb Doped $PbWO_4$ Crystals

5.1 Samples

A total of twelve Sb doped $PbWO_4$ samples, grown by using raw materials in Table 2.1, were studied. The full size samples has tapered shape: 2.6 × 2.6 cm^2 at the large end, tapering to 2.2 × 2.2 cm^2 at the small end, and are 23.0 cm long. The small samples were rectangular in shape. Table 5.1 lists the dimensions, data produced, Sb concentration in melt(ppm wt), post growth annealing condition and peak wavelength of Photo(λ_{pho}) and Radio(λ_{rad}) luminescence as measured by using the setup in section 4.1.1.

Table 5.1: Sb doped $PbWO_4$ crystal samples

ID	Dimension (cm)	Date	Dopant	Annealing	λ_{pho} (nm)	λ_{rad} (nm)
SIC J16	2.5 × **10.5** × 2.5	05/98	320.2	O_2	495	–
SIC 274	2.5 × **21.0** × 2.5	10/98	320.2	O_2	520	450
SIC 275	2.2 × **23.0** × 2.6	10/98	256.2	O_2	510	450
SIC 227	2.0 × **13.3** × 2.0	11/98	480.3	O_2	520	–
SIC 230	2.2 × **23.0** × 2.6	11/98	320.2	O_2	510	–
SIC 324	2.2 × **18.0** × 2.2	02/99	256.2	O_2	510	–
SIC 325	2.5 × **22.0** × 2.5	02/99	256.2	O_2	510	430
SIC S078	2.4 × **10.0** × 2.4	07/99	192.1	–	480	430
SIC AB49	2.2 × **10.0** × 2.2	07/99	256.2	–	480	430

O_2 represents high temperature annealing in O_2, i.e. oxygen compensation.

All samples were grown at SIC by modified Bridgman method. While samples

S078, AB49, J16, 274, 227, 324 and 325 have a rectangular shape, 230 and 275 are full size samples with CMS tapered geometry. Samples were prepared in two ways, i.e. with(J16, 227, 230, 274, 275, 324 and 325) and without(S078 and AB49) oxygen compensation. The oxygen compensation was carried out in conditions optimized for temperature, duration and partial pressure of the oxygen. These optimized conditions were determined by a systematic experiment on pairs of samples cut from different ingots to make sure they are adequate for all crystals.

5.2 Sb Distribution in $PbWO_4$ Crystals

One approach to reduce density of host structure defects is to optimize the stoichiometric ratio between two oxide raw materials and make a stringent control during crystal growth. This approach was attempted by SIC as well as other groups[69, 59]. It is found that this optimization alone is not sufficient to reach required radiation hardness for the CMS. Various approaches to suppress or compensate the remaining defects were taken. Oxygen compensation, referring to post growth annealing at high temperature in an oxygen rich atmosphere, was found effective at SIC[60], indicating main mechanism of radiation damage in $PbWO_4$ is oxygen vacancies, i.e. electron centers.

Doping during crystal growth is another common means to either artificially introduce local charge imbalance and thus compensate structure defects or function as scavenge to further eliminate unwanted impurities. In development of BGO for the L3 experiment, Eu doping was used at SIC to improve its radiation hardness[52]. In development of CsI(Tl) for the *BaBar* and BELLE experiments, a special scavenge was used at SIC to remove oxygen contamination[60]. Pentavalent (Nb) doping in $PbWO_4$ was first reported by Lecoq *et al.*to be effective in improving transmittance at 100 ppm level [56]. Trivalent (La) doping was first reported by Kobayashi *et al.*to be effective in improving both transmittance[57] and radiation hardness[57]. Consequent studies on doping with various ions, such as La, Lu, Gd, Y and Nb, at optimized level were reported to be effective in improving in transmittance as well as radiation hardness[59, 95, 56].

Along the same direction, doping was extensively studied at SIC. This section discusses doping with Sb. Since Sb ions exist in both trivalent and pentavalent forms it is hoped that both electron and hole centers may be compensated by Sb doping. GDMS analysis were systematically performed for different position of Sb doped $PbWO_4$ crystal after growth. These measurements allowed us to determine the segregation coefficient of the doping ions and to tune the doping conditions.

Table 5.2: GDMS analysis results(ppmw) of Sb doped $PbWO_4$ crystals

ID	Z	Melt	Na	Mg	Al	Si	K	Ca	Mo	Sb	TM	RE
227	12	480.3	0.57	0.05	0.10	0.48	1.1	1.0	0.30	27	<0.9	<1.8
227	22		0.05	0.04	0.26	0.31	0.16	0.30	0.51	18	<0.5	<1.0
275	4	256.2	1.2	<0.01	0.04	0.07	0.1	0.12	0.25	110	<0.4	<0.7
275	29		1.0	<0.01	0.05	0.13	0.2	0.30	0.17	26	<0.3	<0.9
325	4	256.2	–	–	–	–	–	–	–	36	–	–
325	23		–	–	–	–	–	–	–	11	–	–
332	2.5	192.1	–	–	–	–	–	–	–	48	–	–
332	24		–	–	–	–	–	–	–	10	–	–
230	29	320.2	0.11	0.02	0.11	0.64	0.24	0.84	0.72	20	<0.2	<0.3
J16	0	320.2	0.73	0.02	0.21	0.26	2.5	1.3	0.92	89	<0.2	<0.3

Z represents sample position from top of ingots, in cm.
Melt represents Sb concentration in melts.
TM represents the sum of transition metals.
RE represents the sum of rare earths.

Table 5.2 lists the result of GDMS analysis for Sb doped $PbWO_4$ crystals and Sb concentration (ppmw) in some $PbWO_4$ samples grown by using raw materials listed in Table 2.1. The result shows that most trace elements, except Sb, are the same level of those in raw materials, indicating no additional contamination in growth process. Table 5.2 also shows that the distribution of Sb in $PbWO_4$ is not uniform with most Sb ions concentrated at the top end of ingots, indicating it has difficulty to enter

$PbWO_4$ lattice. The result of Sb distribution along ingots (Z) together with initial concentration of Sb in melt (Melt) were used to extract the segregation coefficient of Sb in $PbWO_4$.

5.2.1 Segregation coefficient of Sb in $PbWO_4$

Table 5.3 lists GDMS result of Sb concentration (ppmw) in ten Sb doped samples at positions Z (cm) from the top of ingot. Also listed is initial Sb concentration (ppmw) in melt (Melt). The distribution in $PbWO_4$ is not uniform with most Sb ions concentrated at the top end of ingots. The data in Table 5.3 are used to extract the segregation coefficient of Sb in $PbWO_4$. The segregation coefficient k_e, defined as the ratio of the concentration of dopant in the bulk crystal, C_{cryst}, to the concentration of dopant in the melt, C_{melt}, describe the ability of the dopant to be incorporated into the solid phase,

Table 5.3: Result of GDMS analysis of Sb concentration(ppmw) in $PbWO_4$ crystals

ID	227	234	268	275	285	286	295	325	332	338
Melt	401	134	294	214	294	241	241	214	161	268
Z	12/22	10/26	12/22	4/29	4/27.5	2/27.5	6/29.5	4/23	2.5/24	5/29
Sb	27/18	55/12	68/22	110/26	83/29	63/21	94/18	36/11	48/10	39/16

$$k_e = \frac{C_{crystal}}{C_{melt}}. \tag{5.1}$$

Assuming a slow, steady state growth process, the distribution of dopant concentration in crystal can be expressed as:

$$C_{crystal}(g) = k_e \frac{C_0 - \int_0^g C_{crystal}(t)dt}{1-g}. \tag{5.2}$$

where C_0 is the initial dopant concentration in the melt, g is the relative solidification coefficient, defined as the ratio of the volume of solidification part to the whole volume of the crystal ingot. The solution of Equation 5.2 is

$$C_{crystal} = k_e C_0 (1-g)^{k_e - 1}. \tag{5.3}$$

Taking logarithm, Equation 5.3 can be written as a linear equation:

$$\ln\left(\frac{C_{crystal}}{C_0}\right) = \ln k_e + (k_e - 1)\ln(1-g) \tag{5.4}$$

It can now be used for a simple experimental determination of k_e. The logarithmic plot of $C_{crystal}/C_0$ against (1-g) is a straight line and its slope and intercept at $g = 0$ will provide a measure of k_e.

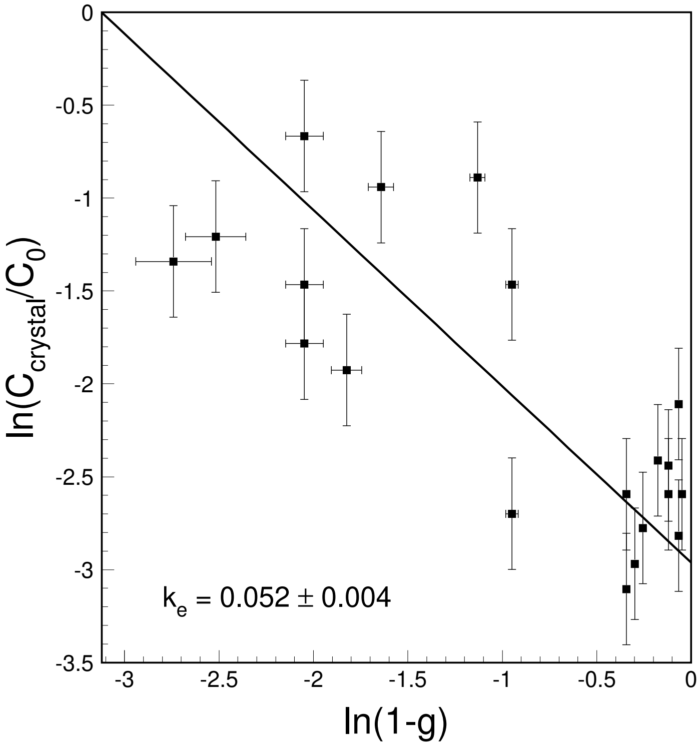

Figure 5.1: A linear fit of Sb concentration in PbWO$_4$ crystals

Figure 5.1 shows a linear fit to the GDMS data. The numerical result of the effective segregation coefficient of Sb ions in PbWO$_4$ crystal is found to be 0.052±0.004, indicating only a small fraction of Sb ions would enter PbWO$_4$ lattice.

5.3 Radiation Damage

The optical properties and light output of these samples are characterized at Caltech both before and after irradiation. All irradiation was carried out by using a ^{60}Co γ-ray source of 50 curie. During irradiation, samples were wrapped with Tyvek paper and aluminum foil, and were placed at a fixed distance to the source, so that entire body of the sample is under a defined dose rate. Samples were under irradiation all the time, except when measurements were carried out, which typically lasted for less than hour. All measurements on the samples after irradiation were carried out in the dark to minimize optical bleaching effect. More detailed discussion on the equipment and techniques used for optical property and light output measurement can be found in reference[60].

5.3.1 Scintillation emission

All Sb doped PbWO$_4$ samples' scintillation emission before and after irradiation were measured by using Hitachi F-4500 Fluorescence Spectrophotometer, as described in section 4.1.1.

Figure 5.2 and Figure 5.3 show the photoluminescence spectra for Sb/Y doped PbWO$_4$ samples 324 and 325 before and after irradiations. Within the measurement errors, the shape of these emission spectra are identical. It is clear that there is no significant change in the shape of the emission and excitation spectra before and after irradiation. As well as samples SIC-324 and SIC-325, other Sb doped samples also kept the same emission shape before and after irradiations. This indicates that the scintillation mechanism which gives rise to this spectral shape is not damaged by the radiation. However, it is more difficult to make any quantitative statement on the possible change in the absolute amplitude of the emission spectra before and after irradiation, since absolute intensity is affected by the systematic errors of the measurements and the radiation induced absorption in the PbWO$_4$ samples.

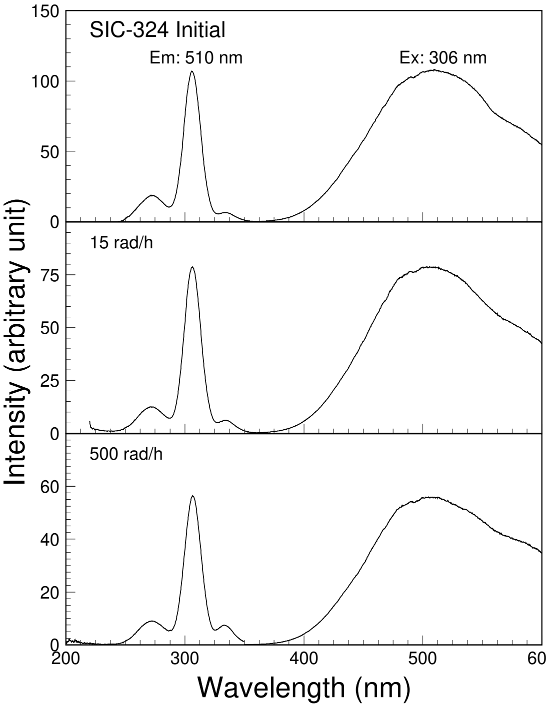

Figure 5.2: Photoluminescence before and after irradiations for Sb doped $PbWO_4$ sample SIC-324

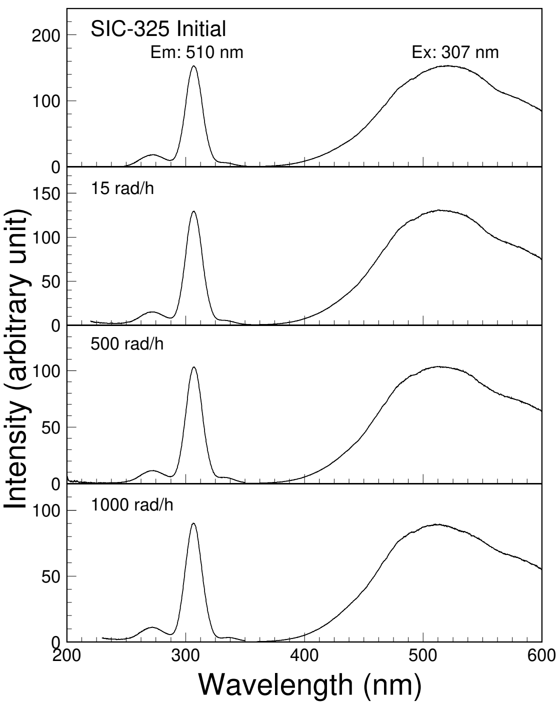

Figure 5.3: Photoluminescence before and after irradiations for Sb doped $PbWO_4$ sample SIC-325

5.3.2 Light output and decay kinetics

The scintillation light output and decay kinetics were measured by using a Hamamatsu PMT R2059, which has a bialkali photo cathode and a quartz window. For the measurement of light output the large end of a sample was coupled to the PMT with Dow Corning 200 fluid, while all other faces of the sample were wrapped with Tyvek paper. A collimated ^{137}Cs source was used to excite the sample. The γ-ray peak was obtained by a simple Gaussian fit, and was used to determine photoelectron numbers by using calibration of the single photoelectron peak.

Figure 5.4 shows the decay kinetics of Sb doped $PbWO_4$ samples determined using the integral method. Figure 5.5 gives emission spectra of nine Sb doped $PbWO_4$ samples measured by Hitachi F-4500. The light yield as a function of integration time was fit to the parameterization given in Eq. 4.15 and the results are shown in

Table 5.4: Light yield (p.e./MeV) of Sb doped PbWO$_4$ samples

ID	LY_{tot}	LY_{50ns}	LY_{100ns}	$LY_{1\mu s}$	$\frac{LY_{50ns}}{LY_{1\mu s}}$	$\frac{LY_{100ns}}{LY_{1\mu s}}$
J16	10.8	8.9	10.1	10.6	84.0	95.3
274	10.3	8.2	9.5	10.2	80.4	93.1
275	11.2	9.0	10.4	11.0	81.8	94.5
227	13.1	10.5	11.9	12.8	82.0	93.0
230	15.6	11.9	13.9	15.2	78.3	91.4
324	13.8	10.9	12.4	13.5	80.7	91.8
325	9.5	8.3	9.2	9.5	87.4	96.8
S078	26.2	19.4	23.4	25.9	74.9	90.3
AB49	20.7	15.8	18.5	20.6	76.7	89.8

the Table 5.4.

Table 5.4 lists the total light yield (LY_{tot} defined in Eq. 4.15) and the light yield integrated in 50 (LY_{50ns}), 100 (LY_{100ns}) ns and 1 μs gates, in units of the number of photoelectrons per MeV of energy deposit (p.e./MeV). Two small samples, S078 and AB49, which did not go through oxygen compensation, have higher light output that other two small samples which were prepared with oxygen compensation. The ratio of light output between 50 and 1,000 ns for all samples with oxygen compensation are larger than 80%(except 230), the ratio of light output between 100 and 1,000 ns for all samples with oxygen compensation are larger than 91%, which are faster than undoped PbWO$_4$ crystals, but is slower than trivalent doped PbWO$_4$ samples. While for two small S078 and AB49, which did not go through oxygen compensation, the ratio of light output between 50 and 1,000 ns is less than 80%, and the ratio between 100 and 1,000 ns is less than 91%. The oxygen compensation has no effect on decay kinetics, but does improve the fast component in the total light output of Sb doped PbWO$_4$ samples. It is also interesting to note that all samples with oxygen compensation have a narrow green emission, while two small samples, S078 and AB49, without oxygen compensation, show a broad emission spectra, have much more slow component, as compared to samples with oxygen compensation. Note the high photoelectron/MeV yield from samples S078 and AB49 is partly due to the

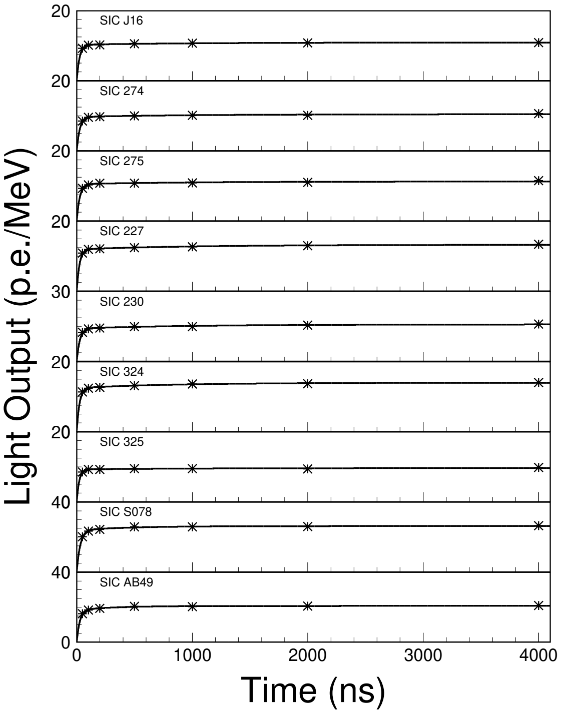

Figure 5.4: The light yield of Sb doped $PbWO_4$ samples as a function of integration time

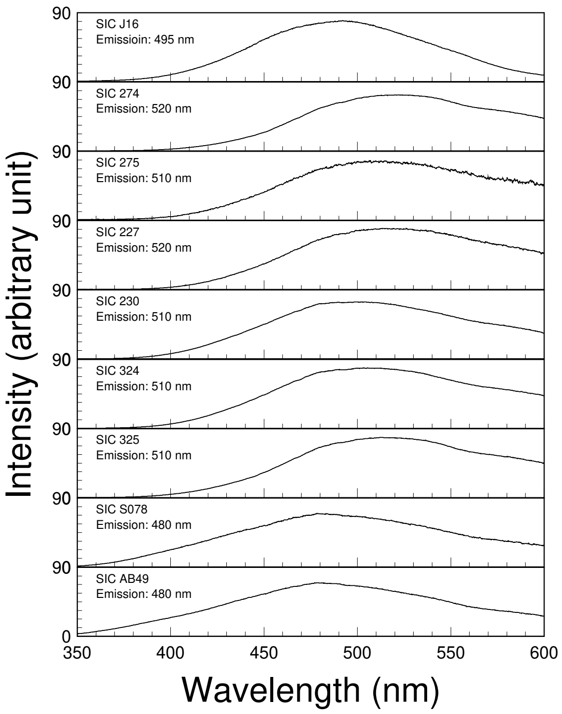

Figure 5.5: Photoluminescence of Sb doped $PbWO_4$ samples as a function of the wavelength

fact that their emission peaked near the region where R2059 PMT provides a higher quantum efficiency.

Figures 5.6 and 5.7 show light output as a function of the integrated gate width. The light output in these figures is in a unit of number of photoelectrons per MeV of energy deposition (p.e./MeV). Two small samples, which did not go through oxygen compensation, have higher light output than other tow small samples which were prepared with oxygen compensation. The ratio of light output between 100 and 1,000 ns is about 90%, as compared to typical 85% for undoped $PbWO_4$ crystals. The trivalent doped $PbWO_4$ samples, however, is more faster. This ratio is typically 98% for Y doped samples. The oxygen compensation seems having no significant effect on decay kinetics. Sample S078 and Ab49, which did not go through oxygen compensation, however, have significantly higher light output than other samples

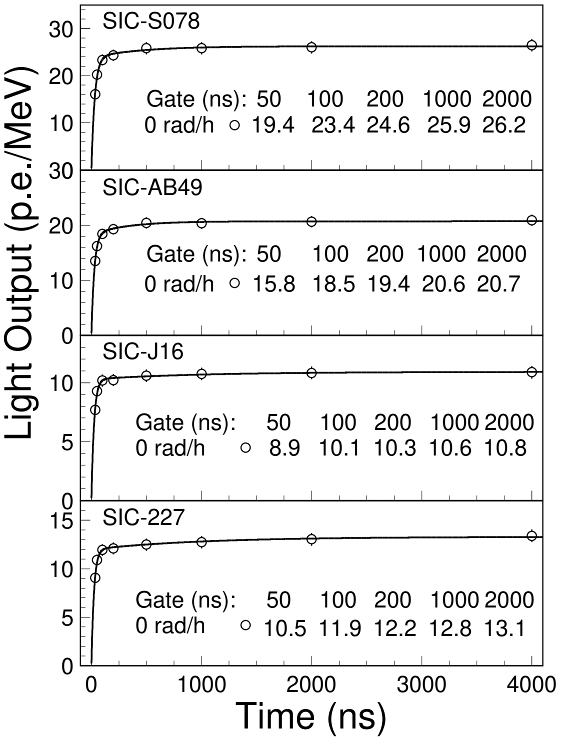

Figure 5.6: Light output of four small size PbWO$_4$ samples is shown as a function of integration time

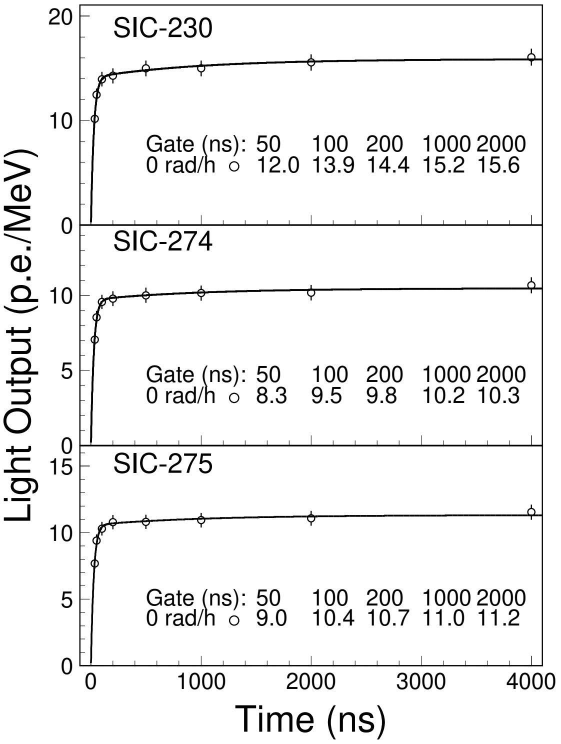

Figure 5.7: Light output of three large size PbWO$_4$ samples is shown as a function of integration time

of similar size, which were prepared with oxygen compensation. The origin of this increase of light output is yet to be understood.

5.3.3 Photo and radio luminescence

Table 5.1 lists peak wavelength of Photo (λ_{pho}) and Radio λ_{rad} luminescence for Sb doped PbWO$_4$ crystal samples treated under different annealing conditions. A schematic of the measurement setup is shown in Figure 4.4 and Figure 4.5 in Section 4.1 in Chapter 4. Figure 5.8 shows the photoluminescence (solid curves) and radio-luminescence (dashed curves) emission spectra for large size samples 230, 274 and 275. Figure 5.9 shows the photoluminescence (solid curves) and radio-luminescence (dashed curves) emission spectra for those small samples. These spectra were corrected for the wavelength dependence of light source intensity, monochromator grating efficiency and detector quantum efficiency. The vertical axis "Intensity" refers to photon numbers, and its scale is arbitrary.

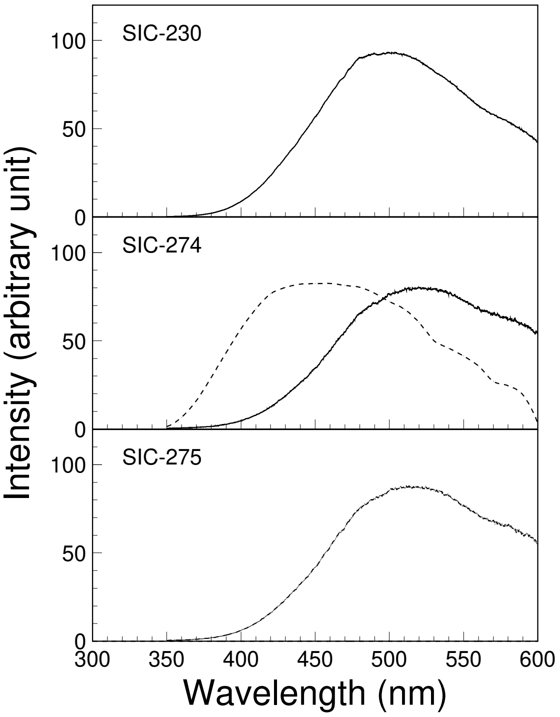

Figure 5.8: A comparison of photo (solid) and radio (dashed) luminescence spectra for three large size Sb doped $PbWO_4$ samples

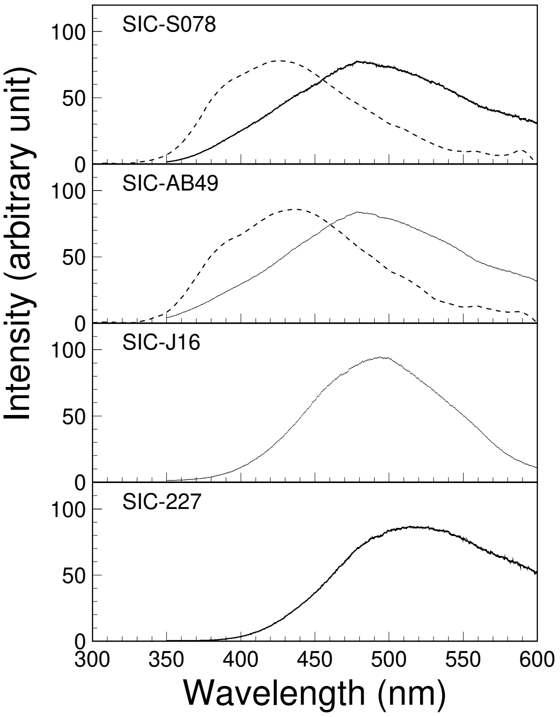

Figure 5.9: A comparison of photo (solid) and radio (dashed) luminescence spectra for small Sb doped $PbWO_4$ samples

It is interesting to note that the peak of photo luminescence of Sb doped samples is similar to what of undoped samples, while peak of radio luminescence is similar to what of trivalent doped samples[118]. As seen from the figure, the peak of radio luminescence is 50 to 60 nm blue shifted as compared to the photo luminescence. The origin of this blue shift is suspected due to that the UV photon is not energetic enough to excite deep scintillation centers in Sb doped $PbWO_4$ crystals. This assumption was confirmed by an X-ray luminescence spectrum with a peak consistent with radio luminescence. One also notices that oxygen compensation has no effect on scintillation for Sb doped samples, and Sb doped samples with or without oxygen compensation show the similar blue shift in radio luminescence as compared to their photo luminescence. The overall shape of most of the emission spectra is similar, and is close to a Gaussian distribution with a FWHM of about 130 nm. Measurements by other group show similar result[117].

5.3.4 Phosphorescence

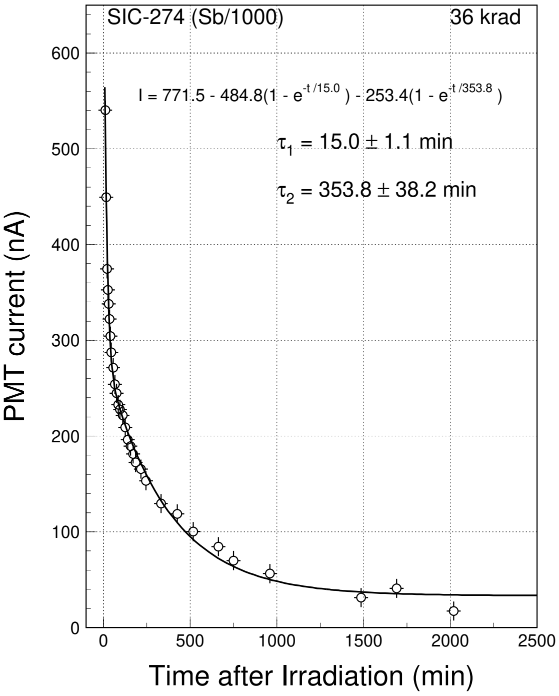

Figure 5.10: The phosphorescence intensity is shown as a function of time for sample SIC 274 after γ-ray irradiation at a dose rate of 400 rad/h

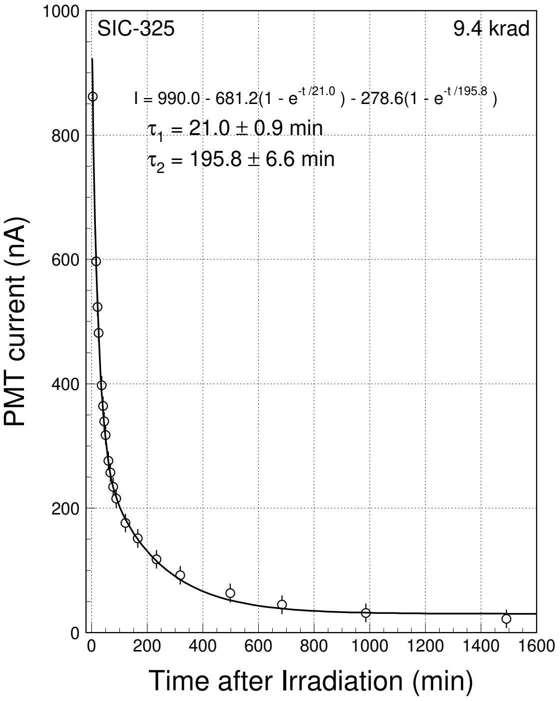

Figure 5.11: The phosphorescence intensity is shown as a function of time for sample SIC 325 after γ-ray irradiation at a dose rate of 400 rad/h

Figure 5.10 and Figure 5.11 show the radiation induced phosphorescence in samples 274 and 325 as a function of time starting approximately 7 minutes after γ-ray irradiation, which were at a dose rate of 400 rad/h. The decay time of the phosphorescence intensity can be fit to two constants: for PbWO$_4$ sample 274, one with a decay time of about 15 minutes, and another with a longer decay time of about 354 minutes. For $PbWO_4$ sample 325, one with a a decay time of about 21 minutes, and another with a longer decay time of about 195 minutes. For very short times after irradiation, the phosphorescence intensity was observed to be considerably higher than after the first 10 min, but decayed away by several orders of magnitude with approximately one minute.

At this low dose rate, the phosphorescence measured immediately after irradiation was essentially independent of total dose for longer exposure. This implies that, under low dose rate conditions, the rate at which conduction electrons are captured in traps reaches a value which is approximately equal to the rate at which electrons are thermally released from these traps and subsequently produce luminescence. However, it should be noted that the magnitude of the phosphorescence can vary significantly from crystal to crystal with different size and transparency.

5.3.5 Longitudinal transmittance

All the Sb samples show an absorption edge at 340 nm and there were no significant absorption bands at wavelengths longer than 500 nm, as seen from the top curve in each plot in Figures 5.12 and 5.13. Their transmittance at 370 nm, which is thought to be related to the radiation hardness of $PbWO_4$ crystals, are all over 40%. For most crystals, the transmittance at 800 nm was $\geq 70\%$, i.e. close to the theoretical limit, indicating a very long light attenuation length at this wavelength. However, below 500 nm, the transmittance shows significant absorption, this absorption causes the yellowish color of the samples caused by absorption bands in the blue region. The exact origin of this absorption is not yet understood.

Figure 5.12 shows the longitudinal transmittance as a function of wavelength measured before and after a series of irradiations for four small Sb doped $PbWO_4$ crystals. The curves in each plot in an order from the top to the bottom represent the transmittance before irradiation and that after irradiation with dose or dose rate specified in

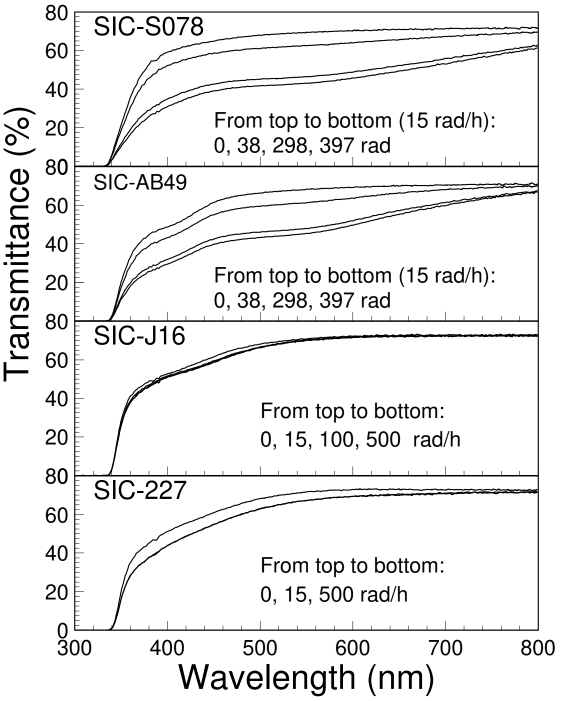

Figure 5.12: Longitudinal transmittance of four small size PbWO$_4$ samples as a function of wavelength measured before and after irradiation

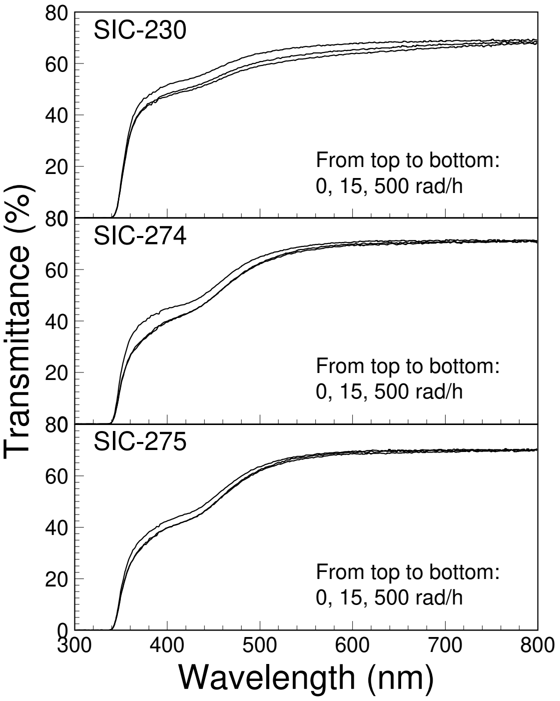

Figure 5.13: Longitudinal transmittance of three large size PbWO$_4$ samples as a function of wavelength measured before and after irradiation

the figure. For samples S078 and AB49, the irradiation was carried out at a dose rate of 15 rad/h with cumulated dosage of 38, 298 and 397 rad. The last two curves are close to each other, indicating that radiation damage in these two samples approach an equilibrium. It is clear that these two samples suffer from significant radiation damage. These absorption bands clearly overlap their scintillation spectra as show in Table 5.1, which has a negative consequence – lowering of light output in samples, i.e. the scintillation light emitted from the crystal was mostly absorbed by crystal itself. For samples J16 and 227, longitudinal transmittance was measured after these samples reached an equilibrium at dose rate of 15, 100 and 500 rad/h. As seen from the Figure 5.12, these two samples suffer much less radiation damage, there are no significant absorption bands overlap their scintillation spectra. Since samples S078 and AB49 were prepared without any annealing, while samples J16 and 227 were prepared with optimized oxygen compensation, this result indicates an improvement of radiation resistance for Sb doped samples with oxygen compensation.

Figure 5.13 shows longitudinal transmittance of samples 230, 274 and 275, measured before irradiation and in equilibrium at dose rate of 15 and 500 rad/h. The small difference in transmittance before and after irradiation indicates that Sb doped samples after oxygen compensation are radiation hard. One also notices that these Sb doped samples suffer from preexisting color centers before irradiation. The nature of these centers is yet to be understood. Very small difference in transmittance before and after irradiations is observed for all radiation hard samples(J16, 227, 230, 274 and 275) prepared with oxygen compensation, indicating Sb doping alone is not enough to make crystal radiation hard, and oxygen compensation is required.

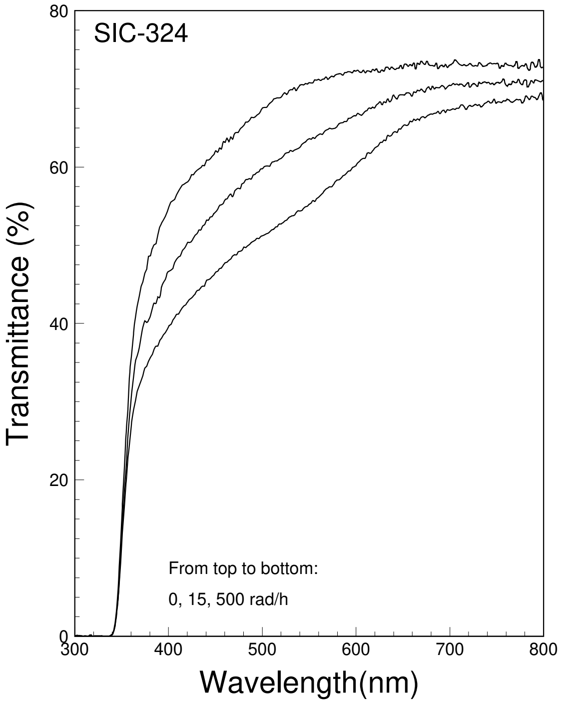

Figure 5.14: Longitudinal transmittance of $PbWO_4$ sample SIC-324 as a function of wavelength measured before and after irradiation

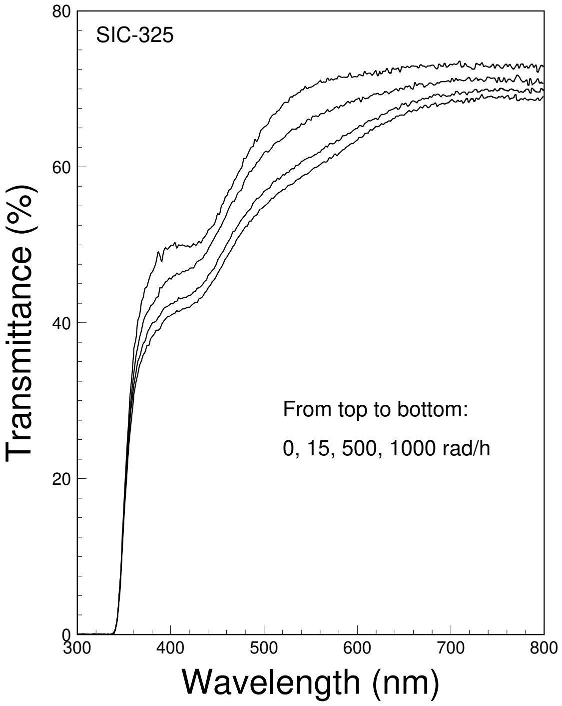

Figure 5.15: Longitudinal transmittance of $PbWO_4$ sample SIC-325 as a function of wavelength measured before and after irradiation

Figures 5.14 and 5.15 show longitudinal transmittance of large samples 324 and

325 (Sb and Y double doped), measured before irradiation and in equilibrium at dose rate of 15, 500, and 1000 rad/h. It is also noticed that they suffer from preexisting color centers before irradiation. Especially for 325, there is clearly a 420 nm absorption band in as grown crystal. These two Sb/Y double doped PbWO$_4$ samples also suffer from significant damage in their transmittance, show a broad radiation induced absorption band which can be decomposed to a sum of two radiation induced color center peaked at 380 and 510 nm respectively. There two absorption bands also overlap their scintillation spectra, thus decreasing the light output of the crystal significantly by self-absorption.

5.3.6 Radiation-induced color center

It is known that color centers are created in PbWO$_4$ crystals under irradiation, and may annihilate under room temperature. During irradiation, both annihilation and creation coexist, the color center density will reach an equilibrium at a level depending on the dose rate applied. Assuming the annihilation speed of color center i is proportional to a constant a_i and its creation speed is proportional to a constant b_i and the dose rate (R), the differential variation of color center density when both processes coexist can be written as [48]

$$dD = \sum_{i=1}^{n} \{-a_i D_i + (D_i^{all} - D_i)\ b_i R\} dt, \tag{5.5}$$

where D_i is the density of the color center i in the crystal and the summation goes through all centers. The solution of Equation 5.5 is

$$D = \sum_{i=1}^{n} \{\frac{b_i R D_i^{all}}{a_i + b_i R}\ [1 - e^{-(a_i + b_i R)t}] + D_i^0 e^{-(a_i + b_i R)t}\}, \tag{5.6}$$

where D_i^{all} is the total density of the trap related to the center i and D_i^0 is its initial density. The color center density in equilibrium (D_{eq}) thus depends on the dose rate

(R):

$$D_{eq} = \sum_{i=1}^{n} \frac{b_i R D_i^{all}}{a_i + b_i R}. \tag{5.7}$$

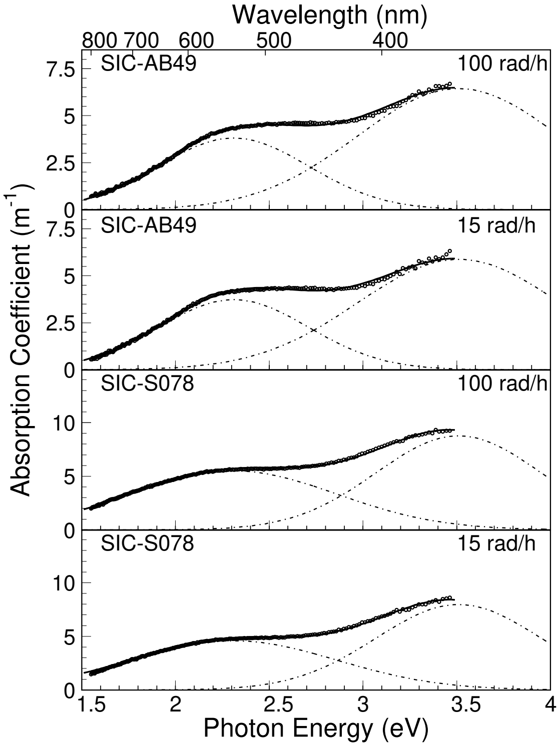

Figure 5.16: Radiation induced color center density for samples AB49 and S078

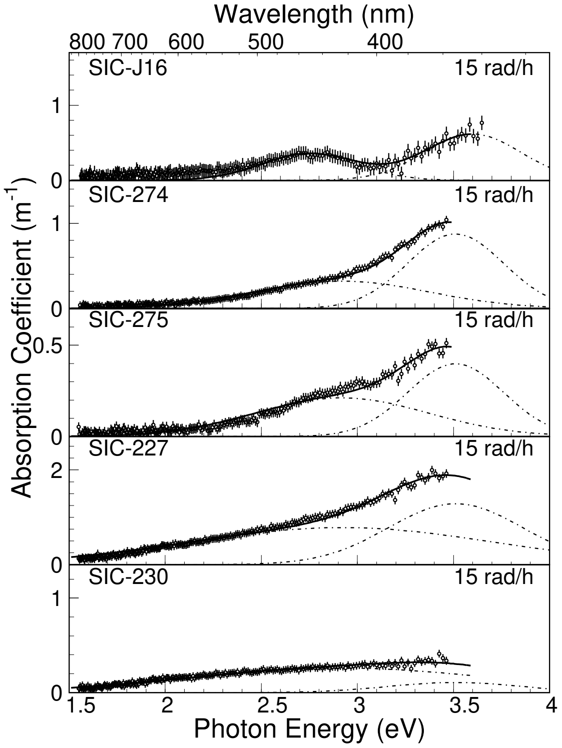

Figure 5.17: Radiation induced color center density for J16, 274, 275, 227 and 230

Figures 5.16 and 5.17 show radiation induced color center density as function of photon energy for sample AB49 and S078, and J16, 274, 275, 227 and 230, respectively. The points with error bars in these figures are radiation induced color center density (D), or absorption coefficient, measured in equilibrium under dose rates specified. They were calculated according to equation

$$D = 1/LAL_{equilibrium} - 1/LAL_{before}. \tag{5.8}$$

where LAL is light attenuation length calculated by using longitudinal transmittance according to Equation 1 of reference [60], and the subscript “equilibrium” and “before" refer to "in equilibrium" and "before irradiation" respectively. For all these samples, the radiation induced color center density was decomposed to a sum (solid line) of two color centers with Gaussian shape in photon energy (dashed lines):

$$D = \sum_{i=1}^{2} A_i e^{-\frac{(E-E_i)^2}{2\sigma_i^2}} \tag{5.9}$$

where E_i, σ_i and A_i denote the energy, width and amplitude of the color center i, and E is photon energy. As seen from these figures, the fit with two centers of Gaussian shape (dashed lines) provides a rather good description of the radiation induced color center data with good χ^2/DoF.

Table 5.5: Summary of radiation induced color centers for Sb doped $PbWO_4$

ID	E_1 eV	σ_1 eV	A_1^a 1/m	A_1^b 1/m	E_2 eV	σ_2 eV	A_2^a 1/m	A_2^b 1/m
J16	2.92	0.45	0.35	0.47	3.51	0.25	0.61	0.92
227	2.92	0.79	0.78	0.84	3.51	0.35	1.28	1.35
230	2.92	0.79	0.25	0.39	3.51	0.35	0.10	0.10
274	2.92	0.45	0.32	0.37	3.51	0.25	0.87	0.88
275	2.92	0.45	0.21	0.23	3.51	0.25	0.39	0.40
AB49	2.31	0.40	3.72	3.80	3.51	0.54	5.87	6.43
S078	2.31	0.55	4.58	5.50	3.51	0.44	7.96	8.76

^{a,b} represent dose rate of 15 and 100 or 500 rad/h respectively.

Table 5.5 lists fit result of radiation induced color centers for seven samples listed in Table 5.1. It is interesting to note that all these samples have a common center peaked at wavelength of 353 nm(3.51 eV) with a width from 0.25 to 0.54 eV. The other less energetic center, however, is peaked at 537 nm (2.31 eV) for samples with oxygen compensation. These centers are more deeper than radiation induced color centers (3.07 and 2.30 eV) in trivalent doped samples[118], indicating a slower recovery speed, or higher stability *in situ*.

5.3.7 Light response uniformity

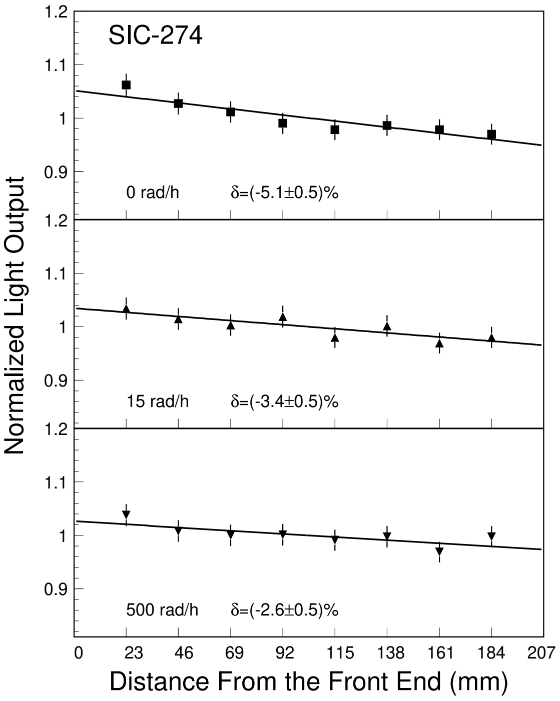

Figure 5.18: The light response uniformities are shown as a function of integrated dose for a large size $PbWO_4$ sample SIC-274

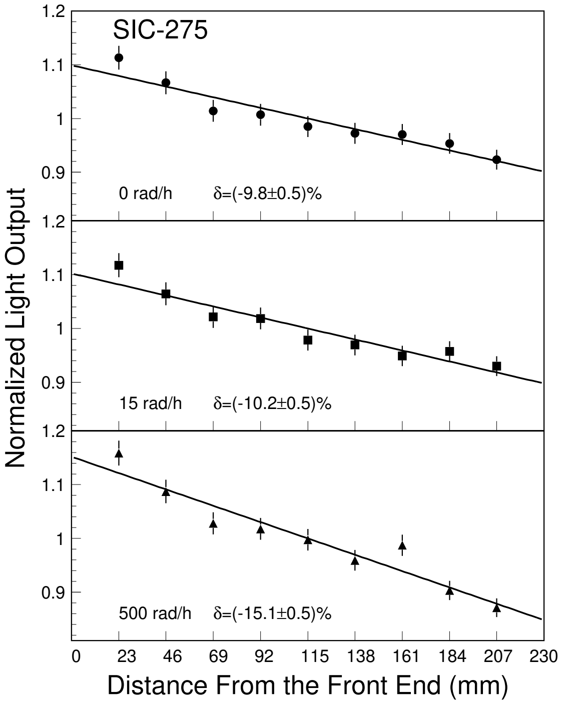

Figure 5.19: The light response uniformities are shown as a function of integrated dose for a full size $PbWO_4$ sample SIC-275

Figures 5.18 and 5.19 show the light response uniformity as a function of accumulated dose for $PbWO_4$ samples 274 and 275 respectively, where δ is a measure of the light response uniformity, as defined in Equation 4.18. The pulse heights measured in eight(274) or nine(275) points evenly distributed along the longitudinal axis of the crystal is fit to Eq. 4.18.

Although these two Sb doped $PbWO_4$ samples were subjected to a uniform irradiation, these two figures show clearly that the slope (δ) and the shape of the uniformity does not change very much during and after irradiations under different dose rate, confirming that the $PbWO_4$ scintillation mechanism is not damaged. The uniformity measurement results also revealed that the distribution of Sb ions in $PbWO_4$ crystals is very inhomogeneous. Other Sb doped small size samples also showed the similar shape of light response uniformity before, during and after irradiations under different dose rate.

5.3.8 Light output degradation and recovery

The most direct representation of crystal radiation hardness is degradation of its light output after irradiation. We use light output normalized to that before irradiation to represent crystal's radiation resistance. To reduce systematic uncertainties of this measurement, light output was defined by an average of several measurements with collimated ^{137}Cs source shooting at evenly distributed positions along the sample. We use 9 measurements for CMS size samples and 5 measurements for samples of ten cm long.

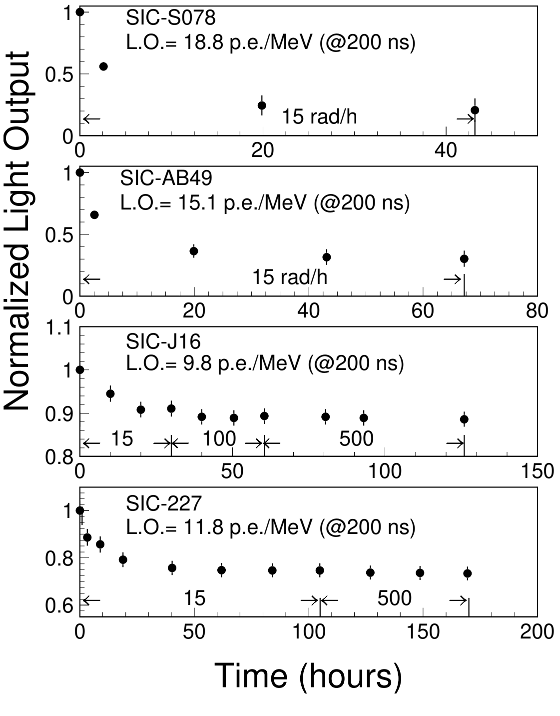

Figure 5.20: Normalized light output as a function of integration time after irradiation for four small size PbWO$_4$ samples

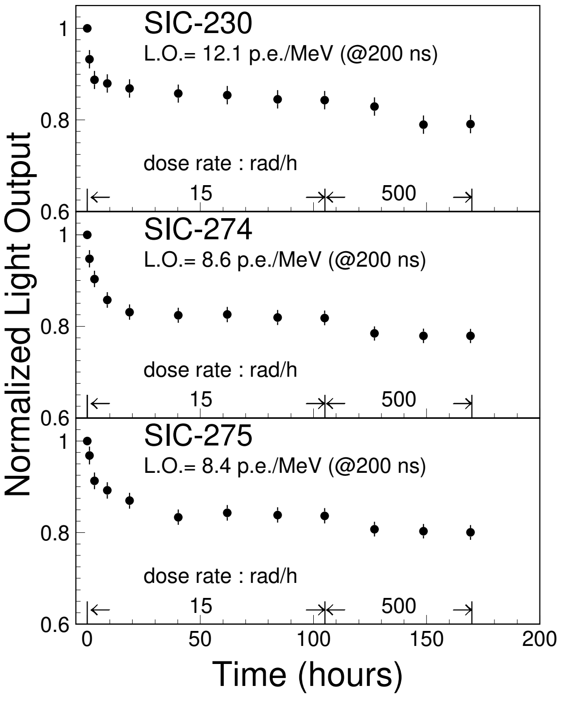

Figure 5.21: Normalized light output as a function of integration time after irradiation for three large size PbWO$_4$ samples

Figure 5.20 and 5.21 show light output degradation (solid dots with error bars) as a function of time for four small and three large samples respectively. Measurements were done step by step for two different dose rates: 15 and 500 rad/h as shown in the figures. The dose rate dependence of light output degradation and the improvement of radiation hardness by oxygen compensation are clearly observed. It is interesting to note that the radiation damage in Sb doped samples is less dose rate dependent that La doped samples[60]. This is consistent with the fact that Sb doped sample has deeper radiation induced color centers as compared to that of trivalent doped sample, as discussed in section 5.3.6. The numerical result of this measurement is listed in Table 5.6 which shows light output degradation in equilibrium under different dose rates. The improvement of radiation hardness by oxygen compensation is clearly seen in this table.

Table 5.6: Light output degradation in equilibrium under irradiation

rad/h	S078	AB49	J16	227	230	274	275
15	20.7	31.6	91.0	74.8	84.1	82.0	83.6
500	–	–	88.9	73.4	79.0	78.0	80.0

The radiation damage in $PbWO_4$ crystal may recovery at room temperature – a consequence of room temperature thermal annealing. The recovery speed, however, depends on the depth of the traps. A slow recovery would ease the calibration requirement, therefore it is preferred for crystals to be used in a radiation environment.

Figure 5.22 shows the consistent damage recovery for three large size Sb doped $PbWO_4$ samples. The plots show normalized light output as a function of time after irradiation. The solid lines in the light output plots are fits to an exponential with time constants of 70.75h, 145.62h and 110.45h for 230, 274 and 275 respectively. It shows that damage in Sb doped $PbWO_4$ samples recovers at a speed of few weeks, the recovery speed for all these three large size Sb doped $PbWO_4$ samples is less than 0.4% per day, which indicates that the radiation-induced color centers in Sb doped $PbWO_4$ are caused by deep traps.

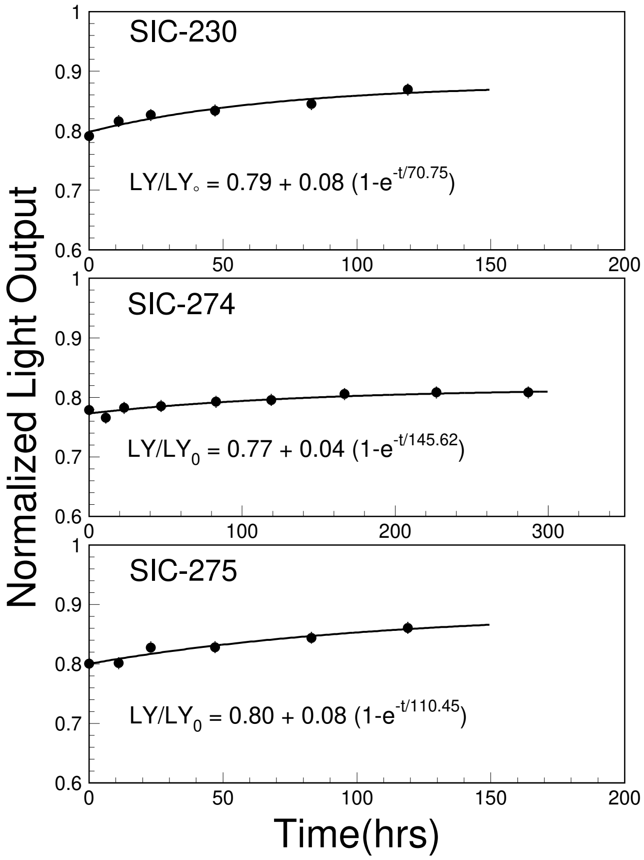

Figure 5.22: The recovery of radiation damage is shown for three large size Sb doped PbWO$_4$ samples

5.3.9 Dose rate dependence

During the radiation tests of PbWO$_4$ crystals, PbWO$_4$ crystals' light output degradations after irradiations are dose rate dependence, as clearly observed in Figures 5.20 and 5.21.

Fig. 5.22 shows fits to the recovery time constant. The light output as a function of time after irradiation was fit to a fast recovery component with a time constant of τ and an amplitude of A_f, and a slow recovery component with an amplitude of A_s.

$$LY/LY_0 = (1 - A_s - A_f) + A_f(1 - e^{-t/\tau}) \tag{5.10}$$

This analysis revealed that there is no fast recovery for radiation induced color centers in Sb doped $PbWO_4$ crystals. In addition, the analysis also revealed that the damage caused by the shallow center saturates at a level from 4% to 8% of the original light output, the damage caused by the deep center changes from 12% to 19% under dose rate of 0.48 krad/hr. For each fixed dose rate, the damage saturates when accumulated dose increases, as shown in Figures 5.20 and 5.21.

The damage phenomena shown in Fig. 5.20, Fig. 5.21 and Fig. 5.22 can be understood by the balance of two coexistence processes: the color center creation (irradiation) and annihilation (spontaneous room temperature annealing). Assuming the annihilation speed of color center i is proportional to a constant a_i and its creation speed is proportional to a constant b_i and the dose rate (R), The color center density in equilibrium (D_{eq}) can be expressed as equation 5.7. It indeed depends on the dose rate (R).

Equation 5.7 also explains why the damage level in equilibrium has no dose rate dependence for a shallow center (large b), while it does for a deep center (small b).

5.4 Improvement of Radiation Hardness

5.4.1 Raw materials improvement

Raw materials used to grow scintillation crystals are required to have high purity, preferable 5N or 6N. The high cost, however, prevents the use of material of extra high purity. Research is needed to find and selectively remove harmful impurities. Various means of material characterization are available to determine trace elements in raw materials as well as crystals. Among them Glow Discharge Mass Spectroscopy (GDMS) analysis is most commonly used. It surveys 77 elements in a sample with precision of sub ppm level for metallic contamination.

Previous GDMS analysis revealed that cation contamination, especially Mo, is responsible for slow scintillation component in $PbWO_4$, as reported by Zhu *et al.* [60]

and Kobayashi [57]. Since Mo is naturally contaminated in WO_3, special effort was made in SIC to remove Mo. After removing Mo and other cation contamination from the raw materials, $PbWO_4$ crystals produced at SIC have significantly reduced the slow component.

Table 2.1 lists the result of GDMS analysis, in ppm weight(ppmw) for trace elements in raw materials of different batches since 1998. Also listed the date of these raw materials produced. All detected impurities at a level greater than 1 ppm are listed, in addition to the sum of the transition metals (TM): Sc, Ti, V, Cr, Mn, Fe, Co, Ni, Cu and Zn, and the sum of detected rare earth elements (RE): Ce, Pr, Nd, Eu, Sm, Gd, Tb, Dy,Ho, Er, Tm, Yb and Lu. The Mo contamination is less than 1 ppm. The results showed that raw materials used at SIC have stable high quality, and thus allow scientists at SIC to study different doping effects in $PbWO_4$ crystals.

5.4.2 Oxygen compensation by high temperature annealing

In our previous study, we pointed out that the radiation resistance of $PbWO_4$ crystals may be improved by oxygen compensation through post-growth thermal annealing in an oxygen-rich atmosphere [64, 71]. Following this, a series of experiments was carried out, aiming to understand the dose rate dependence and optimizing the annealing conditions of oxygen compensation for Sb doped $PbWO_4$ crystals produced at SIC.

A total of seven $PbWO_4$ samples(J16, 274, 275, 227, 230, S078 and AB49) were studied in this investigation. Table 5.1 lists the dimension, date produced and the condition of the post-growth thermal annealing. Samples were prepared in two ways, i.e., with(J16, 274, 275, 227, 230) and without(S078 and AB49) oxygen compensation. The oxygen compensation was carried out in conditions optimized for temperature, duration and partial pressure of the oxygen. These optimized conditions were determined by a systematic experiment on pairs of samples cut from different ingots to make sure they are adequate for all crystals. The optical properties and light output of these samples are characterized at Caltech both before and after irradiation.

As shown in Figures 5.16 and 5.17 for radiation induced color centers, Figures 5.12 and 5.13 for transmittance, Figures 5.20 and 5.21 for light output degradation, samples treated with oxygen compensation have similar radiation hardness, and the improvement of radiation hardness by oxygen compensation is clearly seen. Samples (AB49 and S078) without oxygen compensation, have the worst radiation hardness. Samples J16, 227, 230, 274 and 275, which were annealed under the optimized oxygen conditions are the best. It was also clear that the effect of the post-growth thermal annealing to the radiation hardness of $PbWO_4$ crystals is reproducible, as evidenced by similar behavior of each pair of samples. Despite original hope that Sb doping alone does not improve crystal radiation hardness, oxygen compensation is required to make Sb doped crystals radiation hard. This indicates that Sb doping does not compensate intrinsic density of oxygen vacancies in $PbWO_4$ crystals.

5.5 Summary

As compared to undoped $PbWO_4$ crystal Sb doping is found to reduce slow scintillation components. Oxygen compensation is also found no effect on scintillation and decay kinetics for Sb doped $PbWO_4$ crystals. The concentration of Sb ions in $PbWO_4$ crystals is inhomogeneous. The segregation coefficient of Sb in $PbWO_4$ crystals is determined to be 0.052±0.004, indicating the difficulty of Sb ions to enter the $PbWO_4$ lattice. A broad radio luminescence peaked at the blue (430 to 450 nm) was observed for Sb doped $PbWO_4$ crystals, and it has a 50 to 60 nm blue shift as compared to that of photo luminescence. This shift is explained by not energetic enough photons of the UV excitation light.

The radiation induced absorption in all samples can be decomposed to two color centers with a common center peaked at wavelength of 353 nm (3.51 eV) of a width from 0.25 to 0.54 eV. The other less energetic center, however, is peaked at 537 nm (2.31 eV) for samples prepared with oxygen compensation. These centers are more deeper than radiation induced color centers in trivalent doped samples (307 and 2.30

eV)[118]. These explains a smaller dose rate dependence of radiation damage in Sb doped PbWO$_4$ crystals.

The Sb doping in PbWO$_4$ crystals alone is found not improving crystal radiation hardness. Oxygen compensation is required to make Sb doped crystals radiation hard. Because Sb ions function as pentavalent in high temperature, Sb doping does not make effective compensation for the intrinsic oxygen vacancies in PbWO$_4$ crystals. A more effective compensation of oxygen vacancies is achieved by trivalent doping, such as Y, which will be discussed in next chapter. Results similar to what presented here were also reported by H.F.Chen *et al.* [117].

Chapter 6

Y Doped $PbWO_4$ Crystals

6.1 Y Doped $PbWO_4$ Crystal Samples

Table 6.1: Y doped $PbWO_4$ crystal samples

ID	Dimension (cm)	Dopant	λ_{pho} (nm)	λ_{rad} (nm)	Date
SIC-S110	2.2×**23.0** × 2.5	Y	420	–	02/01/1999
SIC-S111	2.2×**23.0** × 2.6	Y	420	445	02/01/1999
SIC-S249	2.2×**23.0** × 2.6	Y	420	445	04/23/1999
SIC-S261	2.2×**23.0** × 2.6	Y	420	445	04/23/1999
SIC-S301	2.2×**23.0** × 2.6	Y/Sb	420	445	06/08/1999
SIC-S347	2.2×**23.0** × 2.6	Y/Sb	420	445	06/08/1999
SIC-S392	2.2×**23.0** × 2.6	Y	420	445	06/08/1999
SIC-S412	2.2×**23.0** × 2.6	Y	420	445	06/08/1999
SIC-S643	2.2×**23.0** × 2.6	Y	420	445	11/30/1999
SIC-S762	2.2×**23.0** × 2.6	Y	420	445	11/30/1999
SIC-606	2.2×**23.0** × 2.6	Y	420	445	11/30/1999
SIC-678	2.2×**23.0** × 2.6	Y	420	445	08/25/2000
SIC-679	2.2×**23.0** × 2.6	Y	420	445	08/25/2000
BTCP-2133	2.2×**22.9** × 2.5	Y/Nb	420	435	04/01/1999
BTCP-2162	2.2×**22.8** × 2.5	Y/Nb	420	435	04/01/1999
BTCP-5615	2.2×**23.0** × 2.5	Y/Nb	420	435	08/25/2000
BTCP-5618	2.2×**23.0** × 2.5	Y/Nb	420	435	08/25/2000
BTCP-5658	2.2×**23.0** × 2.5	Y/Nb	420	435	08/25/2000
BGRI-824	2.2×**23.0** × 2.6	Y	420	–	07/10/2000
BGRI-826	2.2×**23.0** × 2.6	Y	420	–	07/10/2000

A total of 20 Y doped $PbWO_4$ samples were studied in this investigation. The full size samples has tapered shape: 2.6 × 2.6 cm^2 at the large end, tapering to 2.2 × 2.2

cm^2 at the small end, and were 23.0 cm long. Table 6.1 lists the dimensions, dopant, peak wavelength of Photo (λ_{pho}) and Radio (λ_{pho}) luminescence and date received. Photo (λ_{pho}) and Radio (λ_{rad}) luminescence spectrum was measured by using the setup in section 4.1.1. Samples denoted with SIC were grown at Shanghai Institute of Ceramics, China, by modified Bridgman method. Samples denoted with BTCP were grown at Bogoroditsk Techno-Chemical Plant, Russia, by Czochralski method. Samples denoted with BGRI were grown at Beijing Glass Research Institute, China, also by modified Bridgman method. While the chinese crystals were produced during the R&D phase, the russian crystals were grown during the preproduction phase.

6.2 Y Distribution in $PbWO_4$ Crystals

One approach to reduce density of host structure defects is to optimize the stoichiometric ratio between two oxide raw materials and make a stringent control during crystal growth. This approach was taken by SIC as well as other groups[69, 59]. It is found that this optimization alone is not sufficient to reach required radiation hardness for CMS. Various approaches to suppress or compensate the remaining defects were tried. Oxygen compensation, referring to post growth annealing at high temperature in an oxygen rich atmosphere, was found to be effectively at SIC[60], indicating the main mechanism of radiation damage in $PbWO_4$ is oxygen vacancies, i.e. caused by electron centers.

As discussed in Section 5.2 of Chapter 5, doping during crystal growth is another common means to either artificially introduce local charge imbalance and thus compensate structure defects or function as scavenge to further eliminate unwanted impurities. Along the same direction, doping was extensively studied at SIC. An early attempt of lanthanum (La) doping revealed that it indeed improved transmittance and reduced slow scintillation component, but La doped $PbWO_4$ crystals suffered from large dose dependence caused by shallow radiation induced color centers[111]. The very large (>2) segregation coefficient of La in $PbWO_4$ crystals also makes it very difficult to produce a uniform La distribution in $PbWO_4$ crystals. Following that, doping with antimony (Sb) was tried. Since Sb ions exist in both trivalent and pentavalent forms it was hoped that both electron and hole centers might be compensated by using a single dopant. The result, however, showed that Sb doping alone was not sufficient to produce radiation hard $PbWO_4$ crystals, and post growth oxygen compensation is required to make Sb doped $PbWO_4$ crystals radiation hard. This indicates that Sb doping does not make effective compensation for the intrinsic oxygen vacancies in $PbWO_4$ crystals. The very small segregation coefficient (0.052±0.004) of Sb in $PbWO_4$ also makes it difficult to be implemented. Finally, yttrium (Y) doping was tried. The Y distribution in $PbWO_4$ crystals was found to be rather uniform with a segregation coefficient of 0.91±0.04. Y doped crystals were found to have fast scintillation light and adequate radiation hardness for CMS.

Table 6.2: Results of GDMS analysis (ppmw) for Y doped $PbWO_4$ ingots

Element	Seed/Tail 1	Seed/Tail 2	Seed/Tail 3	Seed/Tail 4	Tail 5
Na	0.2/0.8	0.2/1.0	0.4/0.8	0.2/1.8	0.8
Si	0.5/0.2	0.7/1.3	0.5/1.2	0.5/0.1	0.05
K	0.3/1.8	0.4/1.4	0.7/1.2	0.5/2.0	1.3
Ca	0.9/<0.05	0.6/0.08	0.12/0.15	0.6/0.2	0.15
Cu	0.04/0.2	0.04/0.4	0.3/0.35	0.08/0.54	0.23
As	0.15/0.35	0.1/0.6	0.5/0.5	0.2/0.6	0.54
Y	**40/45**	**40/50**	**30/35**	**40/60**	**50**
Mo	0.3/0.55	0.3/0.9	0.6/0.8	0.2/0.8	1.0
Nb	<.05/<.05	<.05/<.05	<.05/<.05	<.05/<.05	<.05/<.05
Sb	<.05/<.05	<.05/<.05	<.05/<.05	<.05/<.05	<.05
La	<.01/<.01	<.01/<.01	<.01/<.01	<.01/<.01	<.01

GDMS analysis were systematically performed for different position of Y doped $PbWO_4$ crystal samples after growth. A survey of 77 elements revealed impurities at few ppm to sub-ppm level in all samples. These measurements allowed us to determine the distribution uniformity of Y ions in $PbWO_4$ crystals, and the identification of impurities, defects and structural changes are crucial for $PbWO_4$ crystal development, since they are possibly responsible for the blue absorption, the slow decay components and the susceptibility to radiation damage.

Table 6.2 lists impurities (ppmw) found in several pairs of Y doped $PbWO_4$ samples cut from the seed and tail ends of the same ingot. It shows that impurities Na, K, Cu, As and Mo migrated to the tail end of ingots during the growth, indicating that their segregation coefficient in $PbWO_4$ crystals are less than one. The Ca, as well as La[111], are concentrated at the seed end with segregation coefficient of larger than one. The distribution of the yttrium, however, is rather uniform and is slightly less than 150 ppm mol of Y_2O_3 in melt, indicating that its segregation coefficient in $PbWO_4$ is less but close to 1.

6.2.1 Segregation coefficient of Y in $PbWO_4$

Table 6.3: GDMS analysis result of Y concentration (ppmw) in $PbWO_4$ Crystals

ID	Z	Melt	Na	Mg	Al	Si	K	Ca	Mo	**Y**	TM	RE
699	5.5	29.3	0.20	<0.01	0.05	0.18	0.55	0.16	0.47	**39**	<0.5	<1.0
699	29.0	29.3	1.40	0.05	0.34	0.41	0.73	0.60	0.38	**29**	<0.9	<1.0
723	3.0	29.3	1.30	0.06	0.28	0.50	2.50	0.57	0.33	**38**	<0.3	<0.9
723	26.5	29.3	0.92	0.05	0.36	0.30	1.60	0.89	0.28	**30**	<0.5	<0.8
727	4.0	29.3	0.11	<0.01	0.04	0.15	0.23	0.11	0.34	**30**	<0.6	<0.8
727	28.0	29.3	0.07	<0.01	0.04	0.06	0.13	0.56	0.25	**24**	<0.7	<1.0
743	4.5	29.3	0.11	0.06	0.07	0.15	0.24	0.19	0.44	**31**	<0.4	<0.6
743	28.0	29.3	0.06	<0.01	0.11	0.06	0.07	0.49	0.33	**20**	<0.5	<0.7

Z represents sample position from top of ingots, in cm.
Melt represents Y concentration in melts.
TM represents the sum of transition metals.
RE represents the sum of rare earths.

Table 6.3 lists GDMS results of Y concentration (ppmw) in additional four pairs of Y doped samples produced in the year of 2000, taken at positions Z (cm) from the top (the tail end) of ingot. Also listed is initial Y concentration (ppmw) in melt (Melt). As discussed in section 5.2.1, the data in Tables 6.3 and 6.3 are used to extract the segregation coefficient of Y in PbWO$_4$.

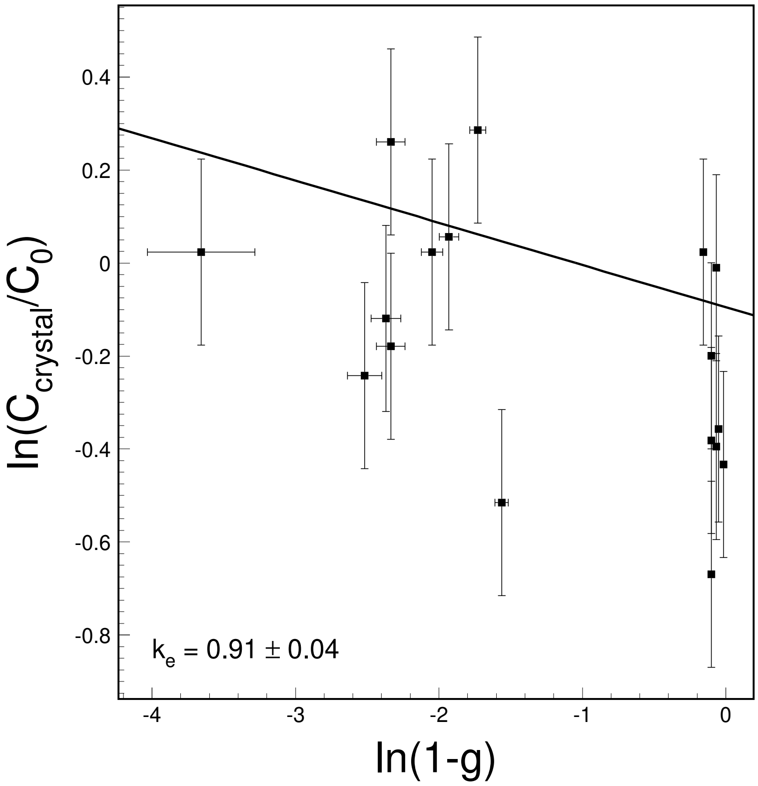

Figure 6.1: A linear fit to the logarithm of Y concentration in PbWO$_4$ crystals

Figure 6.1 shows a fit to the GDMS data. The numerical result of the effective segregation coefficient of Y ions in PbWO$_4$ crystal is found to be 0.91±0.04. The rather uniform distribution of the Y concentration in PbWO$_4$ crystals makes it a good dopant.

6.3 Properties of Y Doped PbWO$_4$ Crystals

6.3.1 Scintillation emission

All Y doped PbWO$_4$ samples' scintillation emission before and after irradiation and/or annealing were measured by using Hitachi F-4500 Fluorescence Spectrophotometer.

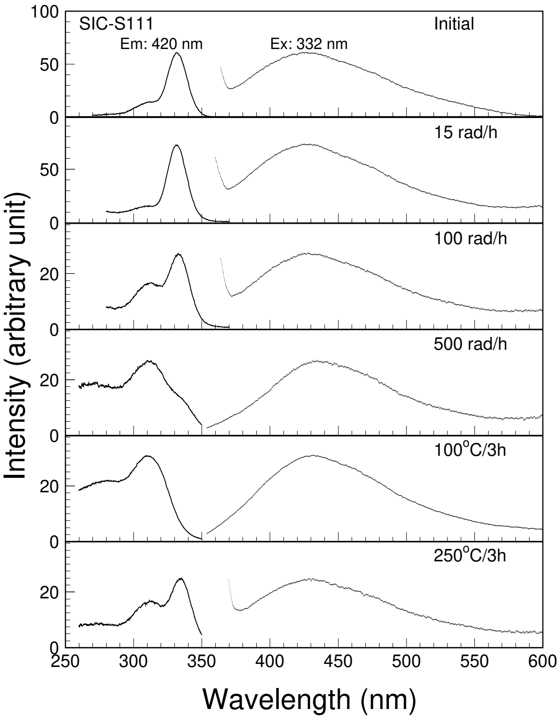

Figure 6.2: Photoluminescence before and after irradiations for Y doped PbWO$_4$ sample SIC-S111

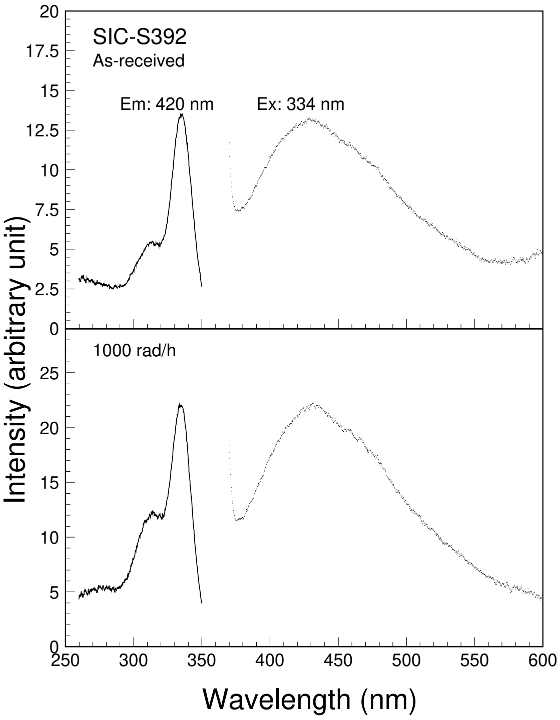

Figure 6.3: Photoluminescence before and after irradiations for Y doped PbWO$_4$ sample SIC-S392

It is interesting to note that the emission of PbWO$_4$ crystals is not affected by the γ-ray irradiation. Figure 6.2 and 6.3 show the photo luminescence spectra before and after irradiations/low temperature annealing for S111 and S392 respectively. Figures 6.4 and 6.5 show the excitation and photo luminescence spectra before and after irradiation for samples SIC-S762 and BTCP-2133 respectively. Within the measurement errors, the shape of these emission spectra are identical. It is clear that there is no significant change in the shape of the emission spectra before and after irradiation. It also shows that low temperature annealing does not change emission spectra for Y doped PbWO$_4$. Same as these two Y doped PbWO$_4$ crystals, all Y doped PbWO$_4$ samples have a broad emission peak around 420 nm, as shown in Table 6.1. They also kept the same emission shape before and after irradiations/low

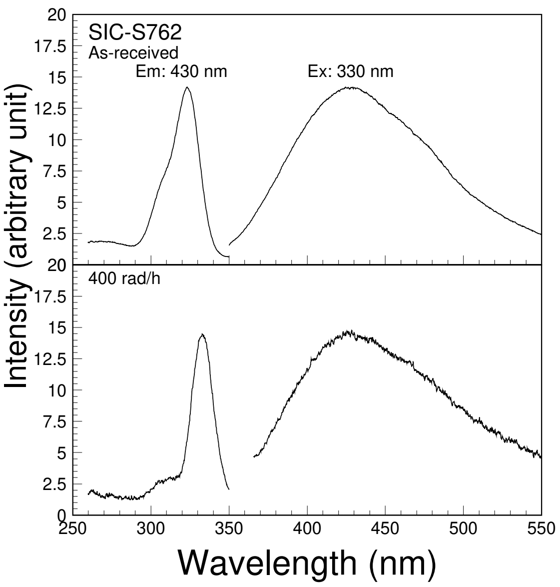

Figure 6.4: Excitation and photo luminescence spectra are shown before and after γ-ray irradiation for a sample SIC-S762

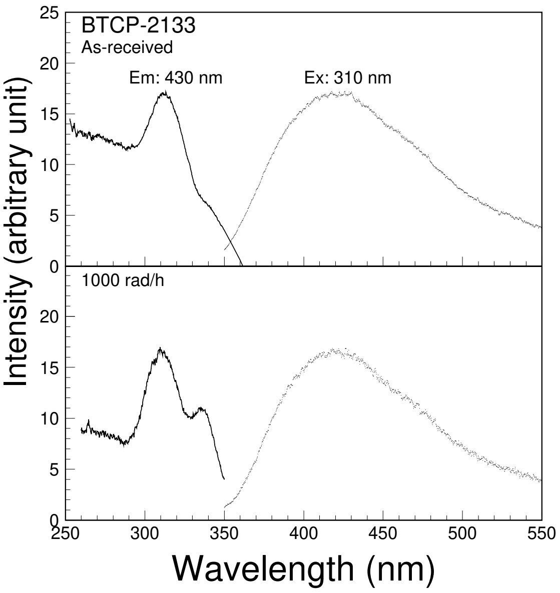

Figure 6.5: Excitation and photo luminescence spectra are shown before and after γ-ray irradiation for a sample BTCP-2133

temperature annealing. This indicates that the scintillation mechanism which gives rise to this spectral shape is not damaged by the radiation[60].

6.3.2 Photo and radio luminescence

Photo luminescence was measured by using a Hitachi F-4500 fluorescence spectrophotometer. A schematic of the measurement setup is shown in Figure 4.4 and Figure 4.5 in Section 4.1 in Chapter 4. Table 6.1 lists peak wavelength of Photo (λ_{pho}) and Radio λ_{rad} luminescence for Y doped PbWO$_4$ crystal samples obtained from different crystal producers. A comparison of photo (solid) and radio(dashed) luminescence spectra for four PbWO$_4$ samples is shown in Figure 6.6. These spectra were corrected for the wavelength dependence of light source intensity, the monochromator grating efficiency and the photo detector quantum efficiency. The vertical axis refers to photon numbers, and its scale is arbitrary.

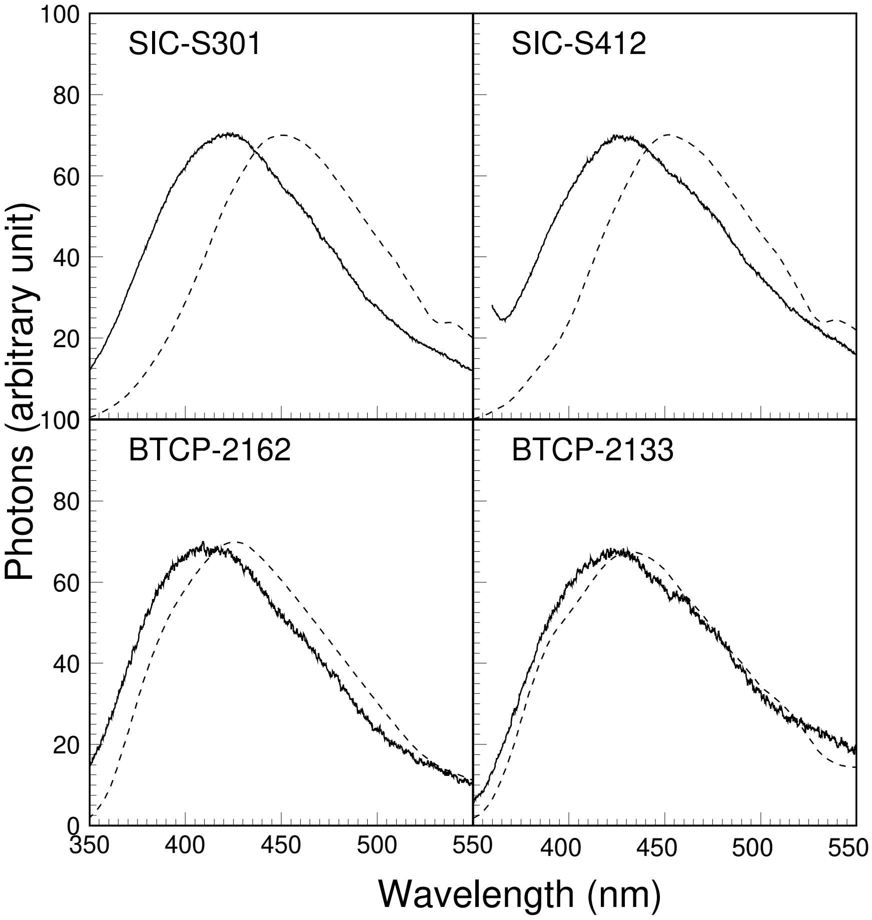

Figure 6.6: A comparison of photo(solid) and radio(dashed) luminescence spectra for six PbWO$_4$ samples

As seen from the figure the peak of radio luminescence is 15 to 25 nm red shifted as compared to the photo luminescence. This red shift can be explained by internal absorption since PbWO$_4$ transmittance at shorter wavelength is poorer than that at longer wavelength. A cross check of photo luminescence with a modified setup, where luminescence light passed through sample, showed similar red shift, and thus confirmed this explanation. Since the photo luminescence spectrum measured with setup in Figure 6.6 is not affected by internal absorption, it can be seen as the intrinsic emission spectrum in general, while the irradiation induced luminescence spectrum is a convolution of intrinsic emission and internal absorption with later depends on the light path. For $PbWO_4$ monitoring, however, the photo detector quantum efficiency weighted radio luminescence spectrum is more relevant since scintillation light propagates through the crystal then reaches the photo detector. Measurement on the other sample show that all Y doped $PbWO_4$ samples have a broad emission spectrum with a peak at about 420 nm.

Compared with emission spectra of Sb doped $PbWO_4$ samples, it is interesting to note that the peak of photo luminescence of Y doped samples is around 420 nm(blue emission), which is similar to La doped $PbWO_4$ samples, while Sb doped samples is similar to what of undoped $PbWO_4$ samples, i.e. around 500 nm(green emission).

6.3.3 Light output and decay kinetics

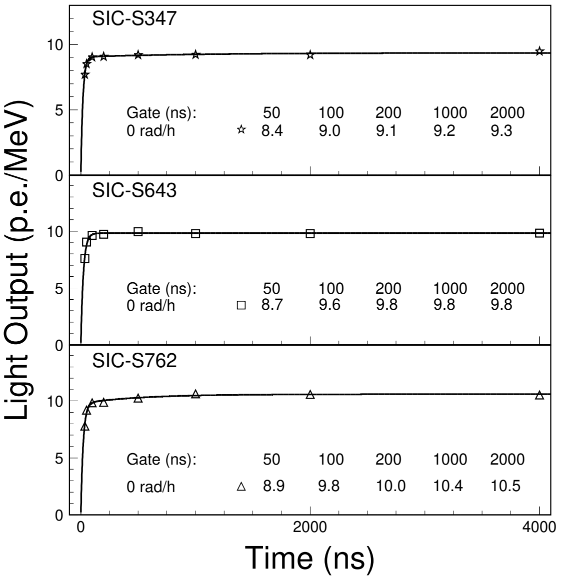

Figure 6.7: Light output of three SIC samples is shown as a function of integration time

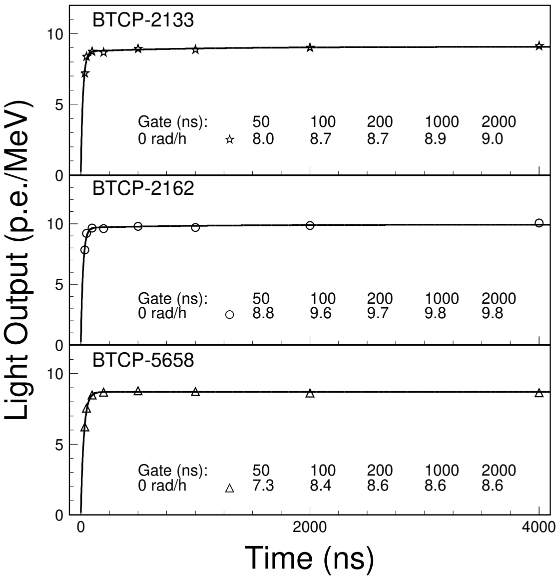

Figure 6.8: Light output of three BTCP samples is shown as a function of integration time

The scintillation light output and decay kinetics were measured using a Hamamatsu PMT R2059, as described in Section 5.3.2. Figures 6.7 and 6.8 show light output as a function of integrated time. The light output in these figures are in units of numbers of photo electrons per MeV of energy deposition (p.e./MeV). The ratio between light outputs integrated to 100 and 1,000 ns is about 95%, as compared to 90% and 85% for Sb doped and undoped $PbWO_4$ crystals respectively[119].

6.3.4 Longitudinal transmittance

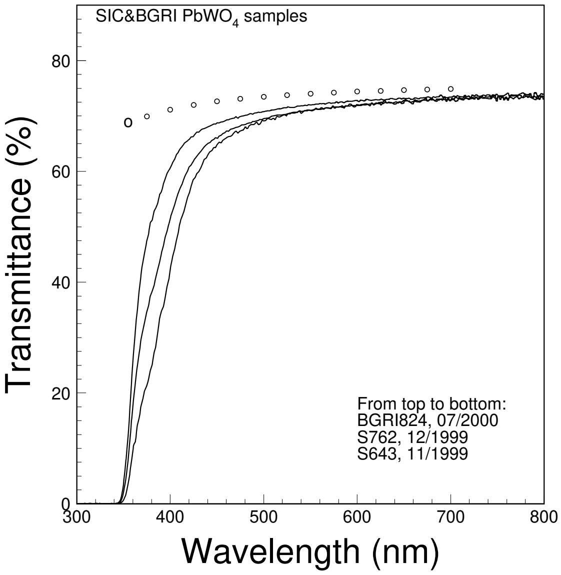

Figure 6.9: Longitudinal transmittance is shown as a function of wavelength for three chinese samples

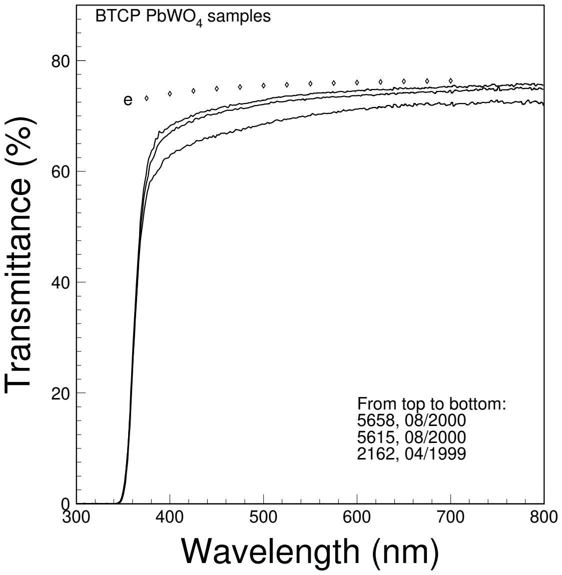

Figure 6.10: Longitudinal transmittance is shown as a function of wavelength for three russian samples

Longitudinal transmittance was measured by using a Hitachi U-3210 UV/visible spectrophotometer as shown in Section 4.2.1. Figures 6.9 and 6.10 show the longitudinal transmittance as a function of wavelength for three $PbWO_4$ samples each from China and Russia respectively. Also shown in these figures are the theoretical limit of the transmittance calculated by using the refractive index of the ordinary (o, circles) and the extraordinary (e, diamonds) light[60]. At the emission peak, 420 nm, the transmittance of the extraordinary light is about 3% higher than that of the ordinary light. Chinese crystals are grown along the c axis so should be compared to the theoretical limit of the ordinary component. Russian crystals are grown along the a axis so should be compared to that of the extraordinary component. Both Russian and Chinese crystals approach theoretical limits, indicating very low residual absorption. Improvements of longitudinal transmittance during the R&D phase for Chinese crystals and the preproduction phase for Russian crystals are observed. It is also noticed that early samples grown in China have a low transmittance at Short wavelength caused by scattering centers, and no direct correlations between transmittance and the radiation hardness were observed. A fine tuning of growth parameters improved transmittance at short wavelength, as shown in Figure 6.9.

6.4 Radiation Damage

6.4.1 Light output degradation and recovery

The most direct representation of crystal radiation hardness is degradation of its light output after irradiation. We use light output normalized to that before irradiation to represent crystal's radiation resistance. To reduce systematic uncertainties of the measurement, light output was defined by an average of several measurements with collimated ^{137}Cs source shooting at evenly distributed positions along the sample. Nine measurements were used for all CMS size (23 cm) samples investigated in this chapter.

It is known that radiation induced color centers are created in $PbWO_4$ crystals by irradiation, and may annihilate in room temperature, as described in Section 5.3.6.

Figures 6.11 and 6.12 show light output normalized to that before irradiation (solid dots with error bars) as a function of time under irradiation for samples SIC-S392 and BTCP-2162. Measurements were done step by step for different dose rates: 15, 100, 500 and 1,000 rad/h under lateral irradiation by a ^{60}Co γ-ray source, as shown in there figures. Note, lateral irradiation provides a uniform dose profile of entire body of the sample, so is more severe as compared to front irradiation[60]. The degradation

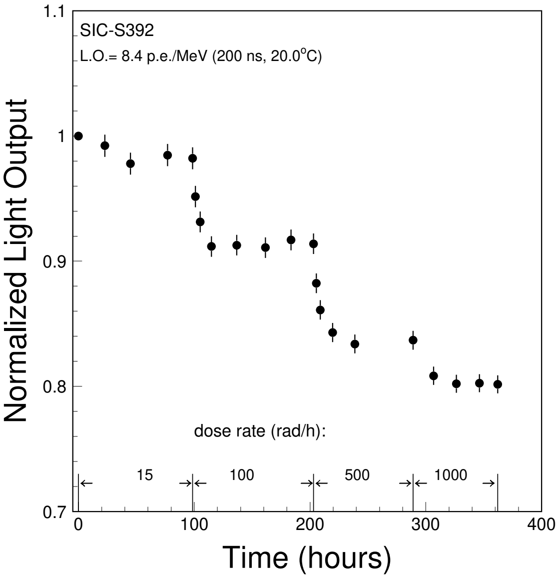

Figure 6.11: Normalized light output is shown as a function of time under irradiation for a sample SIC-S392

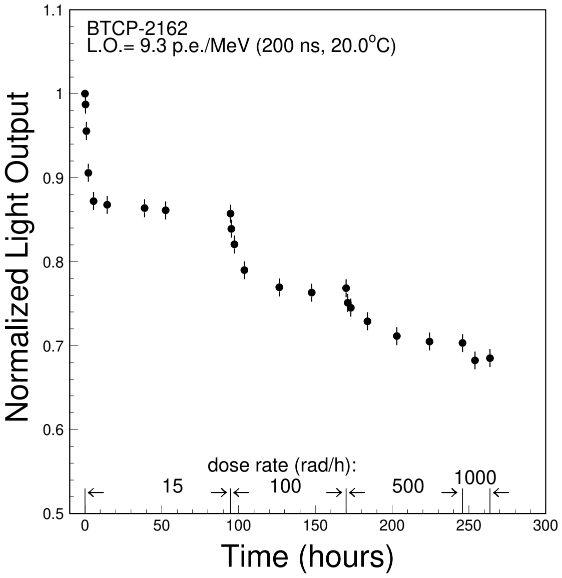

Figure 6.12: Normalized light output is shown as a function of time under irradiation for a PbWO$_4$ sample BTCP-2162

of the light output shows a clear dose rate dependence, as described by Equation 5.7.

Table 6.4 summarizes the numerical results of the light output before irradiation and the normalized light output (%) in equilibrium under certain dose rates. The light Output (L.O.), in units of number of photoelectrons per MeV energy deposition (p.e./MeV), is defined as the average of nine measurements with an integration time of 200 ns at 20.0°C. By using emission weighted quantum efficiencies of the R2059 PMT (14.8%), the measured light output was converted to the light yield in units of photons/MeV. It is clear that the loss of light output at the maximum dose rate at barrel (15 rad/h) is about 5 to 15%, which can be converted to 2 to 6% if irradiated were applied at the front (small) end of the PbWO$_4$ crystal. Also shown in the Table 6.4, low temperature annealing seems having no significant effect on the ratio of light output between 100 and 1,000 ns, indicating no decay kinetics changed for Y doped PbWO$_4$ samples(SIC-606 and SIC-S643).

The radiation damage in PbWO$_4$ crystal recovers at room temperature. Since

Table 6.4: Summary of light output measurements

Sample	L.O. (1/MeV)		Fraction(%)		L.O.(%)@R(rad/h)			
ID	p.e.	γ	$\frac{50\text{ns}}{1\mu\text{s}}$	$\frac{100\text{ns}}{1\mu\text{s}}$	15	100	500	1000
SIC-S249	9.1	61.5	90.6	99.1	94.5	85.7	78.0	74.7
SIC-S261	7.9	53.4	91.6	98.8	93.7	77.2	63.3	-
SIC-S301	9.4	63.5	92.0	96.6	96.6	87.3	79.5	74.3
SIC-S347	9.9	66.9	91.3	97.8	95.1	88.6	82.1	78.0
SIC-S392	8.4	56.8	92.0	97.3	98.2	91.3	83.6	80.2
SIC-S412	8.3	56.1	94.6	98.6	98.2	91.2	85.9	85.3
SIC-S643	8.9	60.1	88.8	98.9	88.3	79.8	–	–
SIC-S762	10.6	71.6	85.6	94.2	91.5	84.2	81.4	–
SIC-606	10.4	70.3	88.3	98.4	91.7	79.3	–	–
SIC-678	10.4	70.3	85.2	93.5	94.2	76.0	59.6	–
SIC-679	10.8	73.0	85.0	94.2	91.5	84.2	81.4	–
BGRI-824	11.4	77.0	83.5	95.5	89.0	78.7	–	–
BGRI-826	11.2	75.7	84.4	96.7	86.0	74.7	–	–
BTCP-2133	8.2	55.4	89.9	97.8	89.2	78.6	72.3	70.5
BTCP-2162	9.3	62.8	89.8	97.9	86.1	76.8	70.3	68.2
BTCP-5615	7.2	48.6	86.6	98.5	82.9	–	–	–
BTCP-5618	7.2	48.6	86.8	98.5	77.4	–	–	–
BTCP-5658	8.8	59.5	83.9	97.7	76.1	63.6	–	–
50°C/4h								
SIC-606	10.9	73.6	87.5	98.5	90.2	78.2	–	–
SIC-S643	9.4	63.5	87.0	98.0	86.2	80.0	–	–
200°C/4h								
SIC-606	10.4	70.3	88.3	98.4	91.7	79.3	–	–
SIC-S643	8.9	60.1	88.8	98.9	88.3	79.8	–	–

the light output of $PbWO_4$ crystals varies during both damage and recovery a precision calibration *in situ* is the key in maintaining the precision of crystal calorimetry. For CMS $PbWO_4$ calorimeter the calibration is achieved by using physics processes combined with the inter calibrations provided by a light monitoring system[10], which measures the variation of the transmittance to 0.1% at the peak wavelength of $PbWO_4$ emission[118, 120]. The goal of the monitoring system is to provide an inter calibration to a precision of 0.4%. Since a complete monitoring run for entire calorimeter takes about 37 minutes[121], the variation speed for the light output, either during damage or during recovery, is proffered to be less than 1%h.

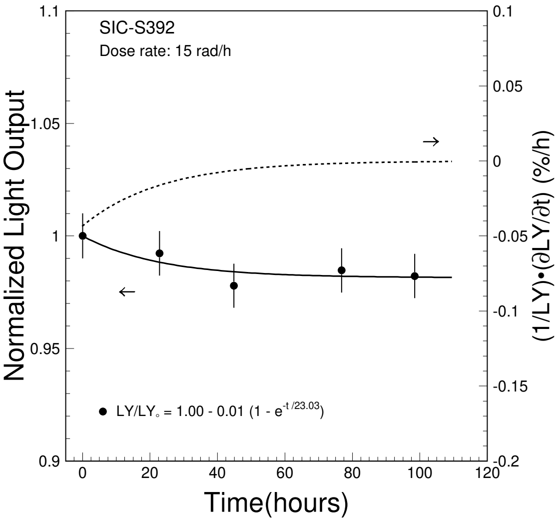

Figure 6.13: Damage speed of normalized light output for a sample SIC-S392

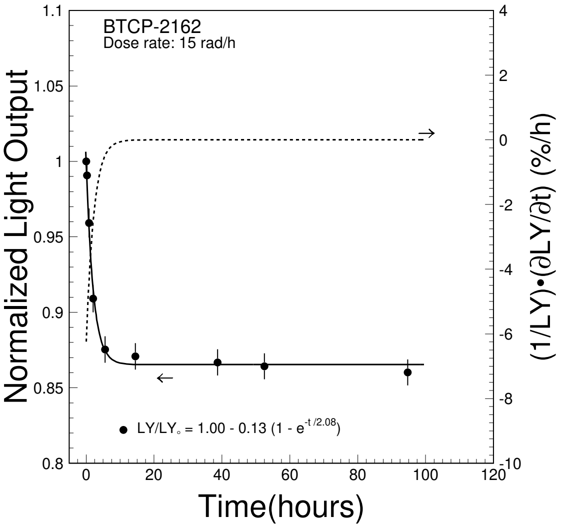

Figure 6.14: Damage speed of normalized light output for a sample BTCP-2162

Figures 6.13 and 6.14 show the damage (dots with error bars, left scale), corresponding exponential fit (solid lines) and damage speed (dashed lines, right scale) of normalized light output under irradiation at 15 rad/h for samples SIC-S392 and BTCP-2162 respectively. Figures 6.15 and 6.16 show the recovery (dots with error bars, left scale), corresponding exponential fit (solid line) and recovery speed (dashed lines, right scale) of normalized light output after an irradiation at 400 rad/h for samples SIC-S392 and BTCP-2162 respectively.

While the damage data were fit to

$$LY/LY_0 = 1 - b(1 - e^{-t/\tau}), \tag{6.1}$$

the recovery data were fit to

$$LY/LY_0 = 1 - a - be^{-t/\tau} = (1 - a - b) + b(1 - e^{-t/\tau}), \tag{6.2}$$

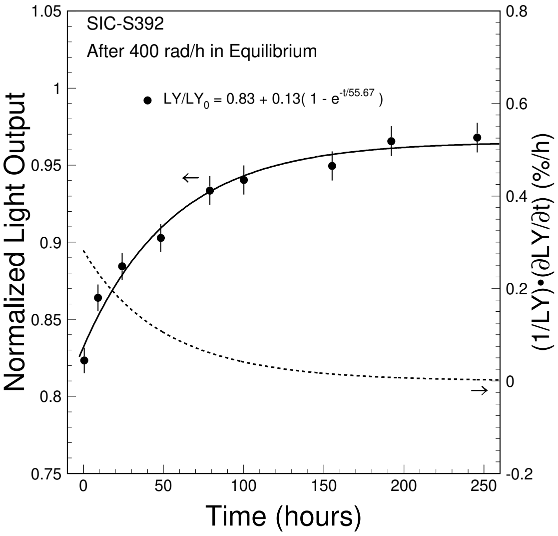

Figure 6.15: Recovery speed of normalized light output for a sample SIC-S392

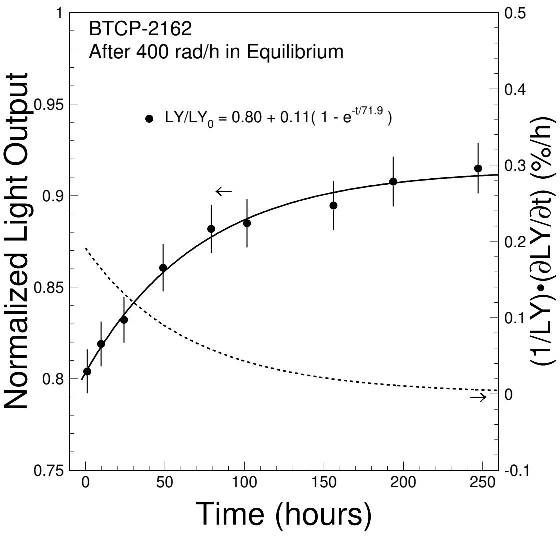

Figure 6.16: Recovery speed of normalized light output for a sample BTCP-2162

where a and b are two constants representing the amplitude of the slow and fast components respectively, and τ is the time constants of the fast component.

6.4.2 Damage and recovery speed

The precision of the calibration performed *in situ* is the key factor in maintaining the precision of crystal calorimetry. Calibration *in situ* is most commonly achieved by using physics processes produced by beam and energy of minimum ionizing particles with known path length. A light pulser system is a useful tool to monitor the light collection in a crystal and the readout response. CMS also uses a light monitoring system to catch change of light collection in $PbWO_4$ crystals *in situ.* The goal of CMS experiment is to calibrate $PbWO_4$ calorimeter to a level of 0.4% by using physics processes and light monitoring.

For a high-precision calorimeter, the scintillator's light output must remain unchanged under irradiation in order to prevent non-uniformities of the crystal response due to a non-uniform irradiation. Moreover, the variation of the crystal response cannot exceed a few per cent and must be slow in order for the monitoring system to correct for these variations with a precision of about 0.4%[121]. Thus a short-term instability of the scintillator parameters dependent on dose rate or accumulated dose is not acceptable for the design of a precise calorimeter. Typically, a complete monitoring run for entire calorimeter would require 37 minutes for Nd:YLF/Ti:Sapphire technology[121]. To reach 0.4% inter-calibration precision for CMS experiment by considering the run time needed for monitoring entire calorimeter, the variation speed for the light output under irradiation(damage)/or without irradiation(recovery) should be kept less than 1%/h.

In order to better understand damage and recovery speed for PbWO$_4$ samples, the normalized light output data as a function of integration time, as such shown in figures 6.13, 6.14, 6.15 and 6.16 were used for calculation. Figures 6.13and 6.14 show the damage speed of normalized light output under ^{60}Co irradiation at 15 rad/h for Y doped(SIC-S392) and Y/Nb double doped(BTCP-2162) respectively. Figures 6.15 and 6.16 show the recovery speed of normalized light output under ^{60}Co irradiation at 400 rad/h.

As shown in the figures, the normalized light outputs(solid dots with error bars) were fitted to an exponential function:

$$LY/LY_0 = a \pm b(1 - e^{-t/\tau}), \tag{6.3}$$

The fitting results are shown in the figures. By using the fitting results, the "Maximum speed" for damage and recovery are calculated as follows:

$$MaximumSpeed = Max\frac{1}{LY}\frac{dLY}{dt} = \pm\frac{b}{a\tau} \tag{6.4}$$

Table 6.5 lists the maximum speed (in the unit of %/h) of ligt output variation for the damage process under different dose rates and for the recovery process after reaching equilibrium at 400 rad/h. As shown in the table, some samples may have too

Table 6.5: Summary of the damage and recovery speed for $PbWO_4$ (%/h)

Sample	Damage under dose rate (rad/h)				Recovery from (rad/h)	
ID	15	100	400	1,000	400	1, 000
SIC-S249	-0.60	**-2.80**	-0.50	-1.10	–	**5.6**
SIC-S261	-0.90	**-3.10**	-1.00	–	–	**2.8**
SIC-S301	-0.21	**-2.30**	**-4.90**	-0.35	0.37	**4.7**
SIC-S347	-0.67	-0.54	**-3.90**	-0.28	0.27	**4.3**
SIC-S392	-0.04	-1.30	-1.60	-0.23	0.31	**4.8**
SIC-S412	-0.10	-0.82	-1.70	-0.81	0.19	**4.0**
SIC-S643	-1.00	-0.85	-1.40	–	0.41	–
SIC-S762	**-3.00**	-1.90	**-3.60**	–	0.04	–
SIC-606	-0.31	-0.53	**-3.10**	–	0.48	–
SIC-678	-1.10	**-5.30**	**-9.00**	–	0.59	–
SIC-679	-0.21	**-4.80**	**-5.80**	–	0.41	–
BGRI-824	**-6.80**	**-2.30**	**-3.20**	–	0.38	–
BGRI-826	**-6.50**	**-4.60**	**-5.10**	–	0.46	–
BTCP-2133	**-5.50**	**-2.80**	-0.75	-1.10	–	0.25
BTCP-2162	**-6.30**	-1.60	-0.51	-0.95	0.19	0.42
BTCP-5615	**-10.8**	–	–	–	–	–
BTCP-5618	**-22.0**	–	–	–	–	–
BTCP-5658	**-16.4**	-0.85	–	–	–	–

fast damage speed under irradiation, indicating possible less accurate calibration for a short time at the beginning. Depending on the initial conditions, Y/Nb double doped samples may have damage speed too fast, while some Y and Y/Sb doped samples may have recovery speed too fast. Further studies on damage/recovery speed *in situ* at LHC (temperature and dose rate) and consequence to monitoring frequency are needed.

6.4.3 Light response uniformity

While variations of the amplitude of the light output can be inter-calibrated, the loss of the energy resolution, caused by the degradation of light response uniformity is not recoverable[60]. To preserve crystal's intrinsic energy resolution the light response uniformity thus must be kept within tolerance. An adequate light response uniformity

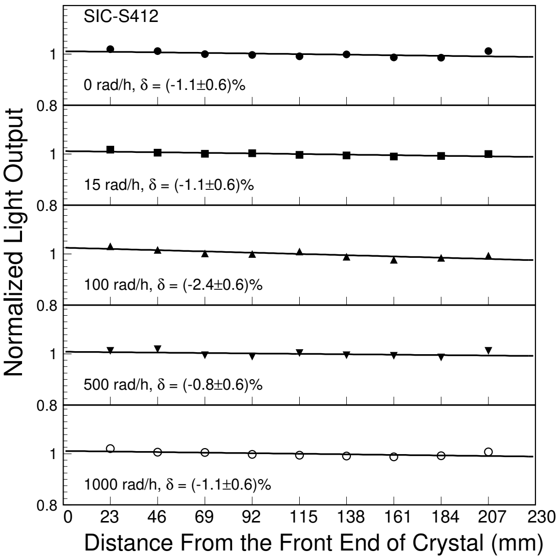

Figure 6.17: The light response uniformities are shown as a function of integrated dose for a full size PbWO$_4$ crystal SIC-S412

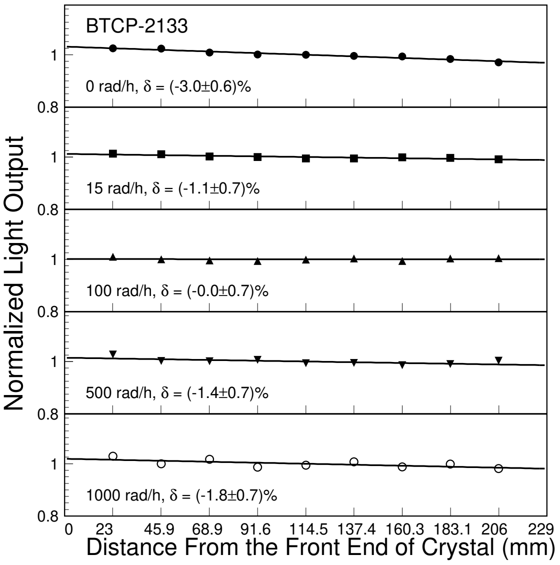

Figure 6.18: The light response uniformities are shown as a function of integrated dose for a full size PbWO$_4$ crystal BTCP-2133

profile is the key to the precision of a crystal calorimeter. According to the recent simulation for CMS PbWO$_4$ crystals[107], the δ value is required to be less than 5% so that its contribution to the constant term of the energy resolution is less than 0.5%. The light response uniformity was measured by moving a collimated γ-ray source along the longitudinal axis of a crystal sample at nine positions evenly distributed along the crystal and the response (y) was fit to a linear function,

$$LY/LY_{mid} = 1 + \delta(x - x_{mid})/x_{mid}, \tag{6.5}$$

where x is the distance from the small (front) end of a tapered crystal, LY_{mid} represents the light responses at the middle of the crystal, δ represents the deviation of the light response uniformity. Figure 3.6 shows light response uniformity definition.

Figures 6.17 and 6.18 show the light response uniformity as a function of accumulated dose for samples SIC-S412 and BTCP-2133 respectively, where δ is a measure of the light response uniformity, as defined in equation6.5. These figures show clearly that the slope (δ) and the shape of the uniformity does not change. The results confirm that the $PbWO_4$ scintillation mechanism is not damaged, all the δ value is less than 3%. This good uniformity can be attributed to the fact that the light attenuation length at the emission peak (420 nm) is long enough even after irradiation to provide adequate compensation between the attenuation and the focusing effect caused by crystal's tapered shape[17]. The uniformity measurement results also revealed that the distribution of Y ions in SIC $PbWO_4$ crystals is homogeneous.

6.4.4 Longitudinal transmittance

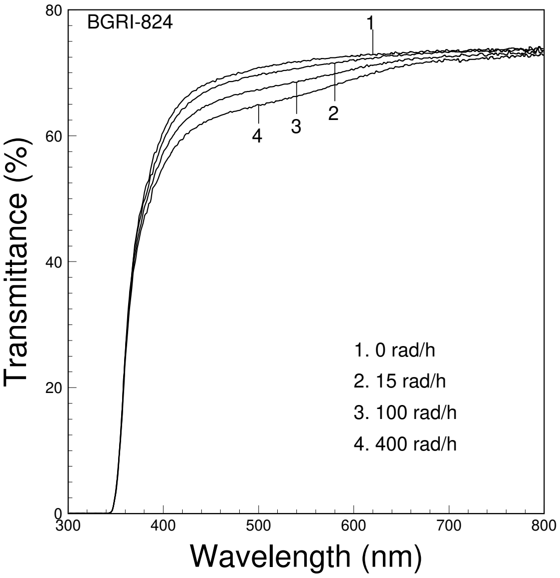

Figure 6.19: Longitudinal transmittance is shown as a function of wavelength for sample BGRI-824 before and after irradiation

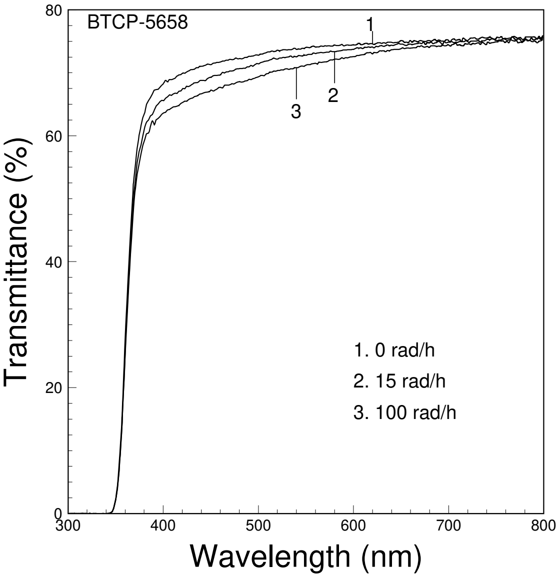

Figure 6.20: Longitudinal transmittance is shown as a function of wavelength for sample BTCP-5658 before and after irradiation

Figures 6.19 and 6.20 show the longitudinal transmittance as a function of wavelength measured before and after a series of irradiation for sample BGRI-824 and BTCP-5658 respectively. The curve in each plot in an order from the top to the bottom represent the transmittance before irradiation and that immediately after irradiation when they reached an equilibrium under specified dose rate. It is interesting to note that these two samples have very similar behavior under irradiation. As discussed before[118] and in Section 6.4.5 below, the radiation induced absorption in all Y doped samples can be decomposed to two common radiation induced color centers.

6.4.5 Radiation induced color center

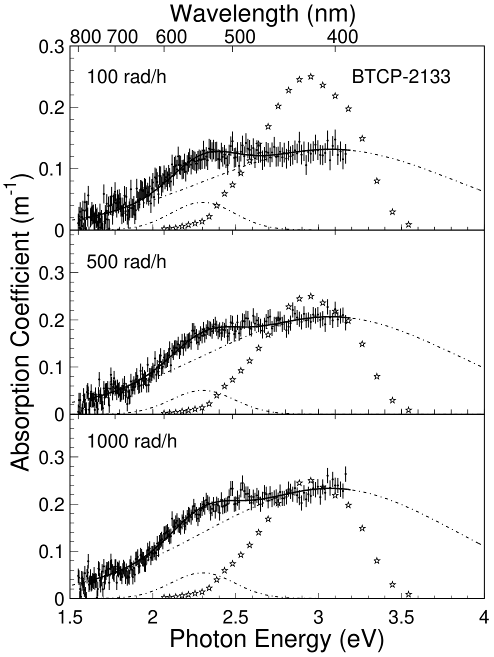

Figure 6.21: Radiation induced color center density for a Y/Nb doped BTCP-2133

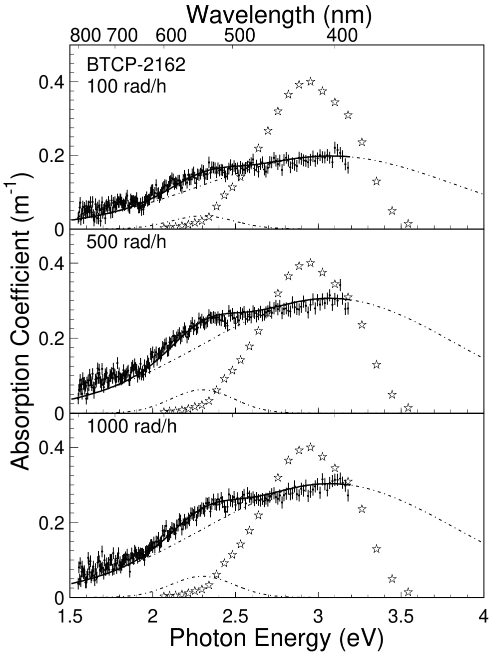

Figure 6.22: Radiation induced color center density for a Y/Nb doped sample BTCP-2162

By using longitudinal transmittance one can calculate radiation induced color center density. Figures 6.21, 6.22, 6.23 and 6.24 show radiation induced color center density as function of photon energy measured for six PbWO$_4$ crystals in equilibrium at different dose rates. The stars in these figures represent corresponding radio luminescence spectra weighted with quantum efficiency of the PMT. The points with

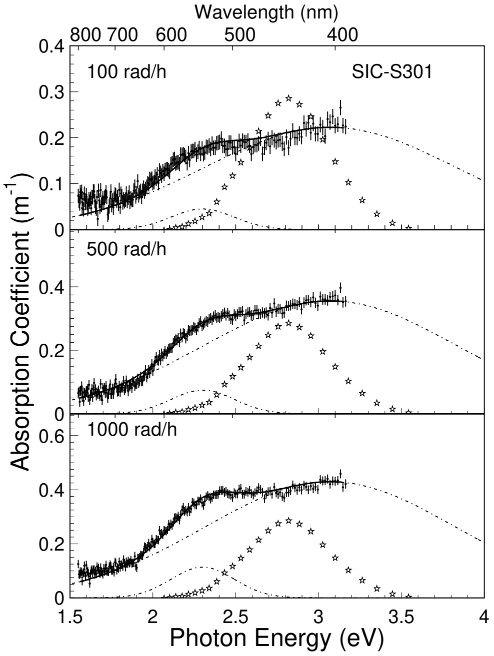

Figure 6.23: Radiation induced color center density for a Y/Sb doped sample SIC-S301

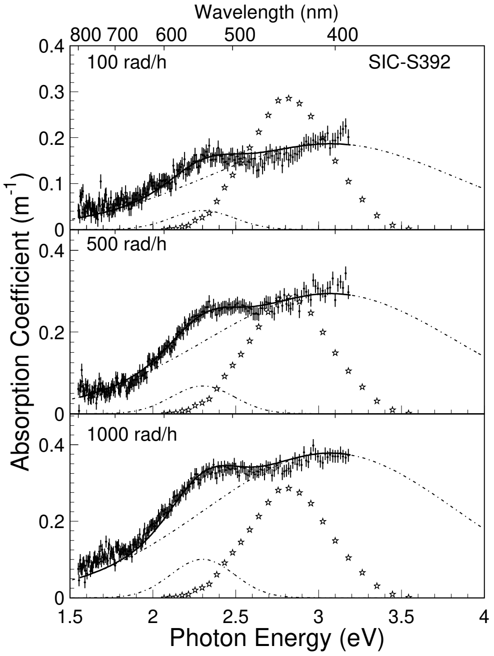

Figure 6.24: Radiation induced color center density for a Y doped sample SIC-S392

error bars in these figures are radiation induced color center density (D), or absorption coefficient, measured in equilibrium under dose rates specified. It was calculated according to equation 5.8. For all these samples, the radiation induced color center density was decomposed to a sum (solid line) of two color centers with Gaussian shape in photon energy (dashed lines):

$$D = \sum_{i=1}^{2} A_i e^{-\frac{(E-E_i)^2}{2\sigma_i^2}} \tag{6.6}$$

where E_i, σ_i and A_i denote the energy, width and amplitude of the color center i, and$E$ is photon energy. As seen from these figures, the two center Gaussian fit provides a rather good description of the radiation induced color center data with good χ^2/DoF.

Table 6.6 lists numerical result of fits for 16 samples listed in Table 6.1, where S, BG and B represent SIC, BGRI and BTCP respectively. Consistent fit with two

Table 6.6: Summary of radiation induced color centers for PbWO$_4$

ID	E_1/σ_1 eV/eV	A_1^a m^{-1}	A_1^b m^{-1}	A_1^c m^{-1}	A_1^d m^{-1}	E_2/σ_2 eV/eV	A_2^a m^{-1}	A_2^b m^{-1}	A_2^c m^{-1}	A_2^d m^{-1}
S-S301	2.30/0.19	0.00	0.04	0.07	0.11	3.07/0.76	0.10	0.22	0.35	0.42
S-S347	2.30/0.19	0.00	0.00	0.03	0.07	3.07/0.76	0.10	0.13	0.14	0.38
S-S392	2.30/0.19	0.00	0.04	0.06	0.10	3.07/0.76	0.10	0.18	0.29	0.37
S-S412	2.30/0.19	0.00	0.03	0.04	0.06	3.07/0.76	0.10	0.15	0.19	0.24
S-S643	2.30/0.19	0.02	0.05	0.08	–	3.07/0.76	0.14	0.22	0.25	–
S-S762	2.30/0.19	0.00	0.00	0.00	–	3.07/0.76	0.11	0.21	0.24	–
S-606	2.30/0.19	0.00	0.07	0.14	–	3.07/0.76	0.10	0.26	0.54	–
S-678	2.30/0.19	0.03	0.11	0.23	–	3.07/0.76	0.10	0.38	0.78	–
S-679	2.30/0.19	0.05	0.14	0.26	–	3.07/0.76	0.10	0.39	0.77	–
BG-824	2.30/0.19	0.00	0.04	0.09	–	3.07/0.76	0.10	0.25	0.42	–
BG-826	2.30/0.19	0.01	0.07	0.16	–	3.07/0.76	0.15	0.36	0.65	–
B-2133	2.30/0.19	0.00	0.04	0.05	0.05	3.07/0.76	0.10	0.13	0.20	0.23
B-2162	2.30/0.19	0.01	0.03	0.06	0.06	3.07/0.76	0.10	0.19	0.30	0.30
B-5615	2.30/0.19	0.00	–	–	–	3.07/0.76	0.10	–	–	–
B-5618	2.30/0.19	0.00	–	–	–	3.07/0.76	0.12	–	–	–
B-5658	2.30/0.19	0.00	0.00	–	–	3.07/0.76	0.12	0.27	–	–

^{a,b,c,d} represent 15, 100, 500, 1000 rad/h respectively.

common radiation induced color centers at the same energy and with the same width was found for all samples. One broad center is at wavelength of 400 nm (3.07 eV) with a width of 0.76 eV, and other narrow centers is at a longer wavelength of 540 nm (2.30 eV) with a width of 0.19 eV. This indicates that the radiation induced color centers are crystal structure related. This conclusion consists with oxygen vacancy assumption. It is also interesting to note that these two color centers are peaked well apart at two sides of the peak of radio luminescence, and they have different damage and annihilation constants. This indicates that PbWO$_4$ monitoring light wavelength must be carefully chosen so that variations of crystal light output may be adequately estimated by using variations of transmittance.

6.5 "Instability" Under Room Temperature

6.5.1 Low temperature thermal annealing

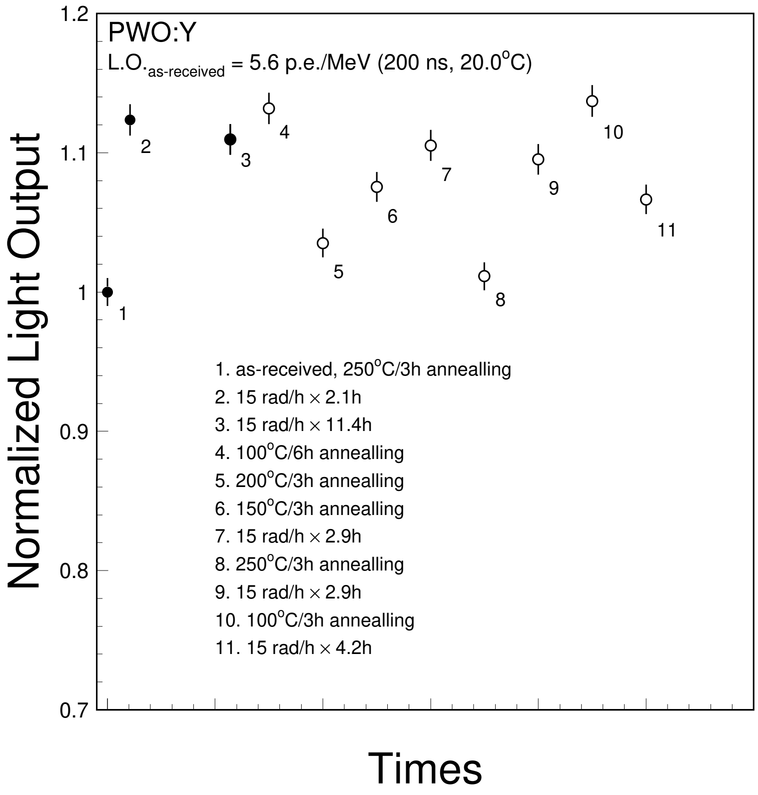

Figure 6.25: Normalized light output after various irradiation and annealing processes for an early Y doped $PbWO_4$ sample

One peculiar property was found in Y doped $PbWO_4$ samples grown at SIC in early development stage. The light output of some Y doped samples was found to increase under irradiation. Figure 6.25 shows the variation of an early sample after various irradiation and annealing processes. As shown in the figure, its light output was increased by 12% under an irradiation at 15 rad/h, and was increased further after a thermal annealing of 100°C. It was decreased by 10% after a thermal annealing at 200°C. While showing good light output under irradiation, crystals of this type are not conventional since it is difficult to define their nominal light output.

This peculiarity was understood as an effect of the optical bleaching pre-existing color centers by the scintillation light. Scintillation light was produced when a sample is under irradiation by ^{60}Co γ-rays. If the annihilation speed of a pre-existing color center, caused by the bleaching effect of the scintillation light, is larger than the creation speed of a radiation-induced color center under low dose irradiation, the total density of color centers would decrease, not increase, under irradiation. High temperature annealing also creates such pre-existing centers. A study of optical bleaching by using light of different wavelengths confirmed that the optical bleaching is indeed effective in removing pre-existing color centers, as will be discussed in next section 6.5.3.

6.5.2 Hunting for the origin of "instability"

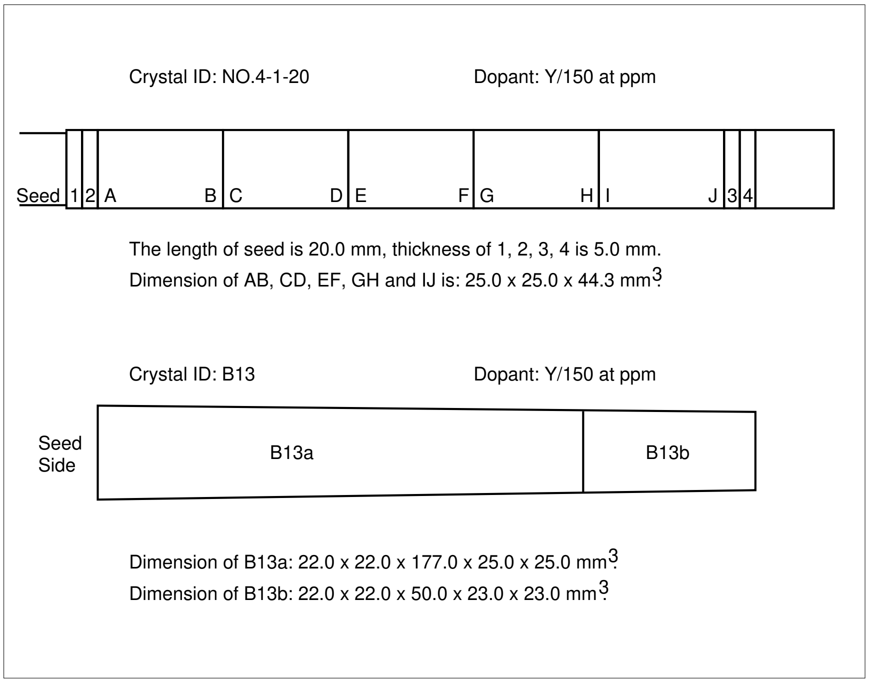

Figure 6.26: $PbWO_4$ samples investigated for the origin of "instability"

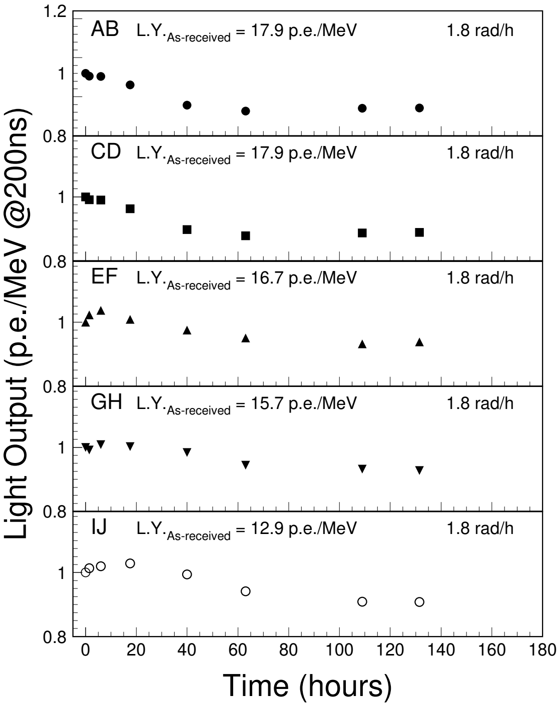

Figure 6.27: Light output degradation for five 4.4 cm samples cut from 4-1-20

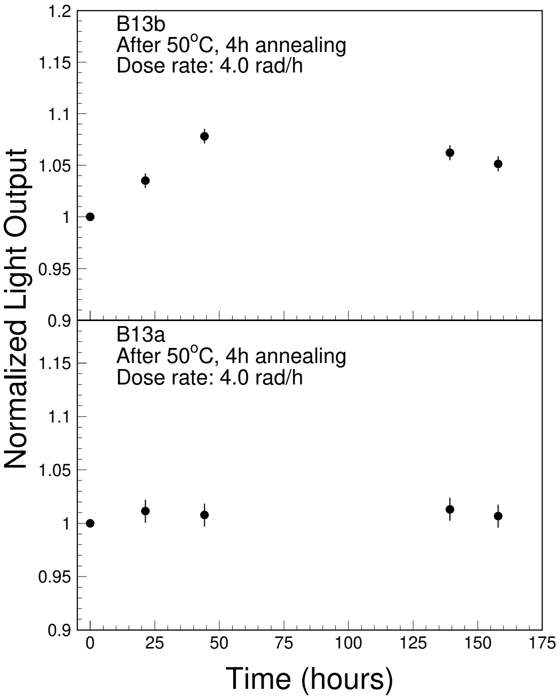

Figure 6.28: Light output degradation for 18 and 5 cm samples cut from B13

Although an initial thermal annealing at a lower temperature would solve this problem, R&D was carried out to hunt for the origin of these pre-existing color centers. In this investigation, full size $PbWO_4$ ingots were cut into short pieces. As shown in Figure 6.26, five 2.5×2.5×4.4 cm samples were cut from ingot 4-1-20, and an 18 and a 5 cm long samples were cut from another full size tapered sample B13.

All these samples went through standard radiation test at Caltech. It was found that only the sample at the tail end have this problem. Figure 6.27 and 6.28 show normalized light output of these short samples under irradiations at low dose rate. No "instability" was found for samples cut from the seed side of Y doped $PbWO_4$ ingots. GDMS analysis results carried out for these samples are shown in Table 6.2, and the impurities of Na, K, Cu, As and Mo were found to be concentrated at the tail end. This information was fed back to SIC, and the parameters of crystal growth

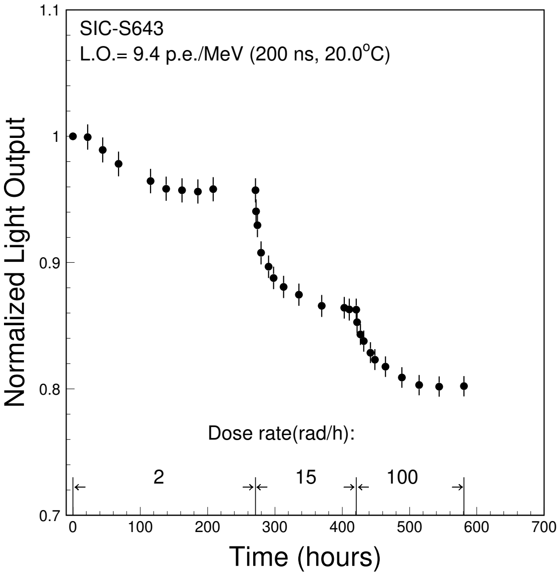

Figure 6.29: Normalized light output is shown as a function of time under irradiations at 2, 15 and 100 rad/h for sample SIC-S643

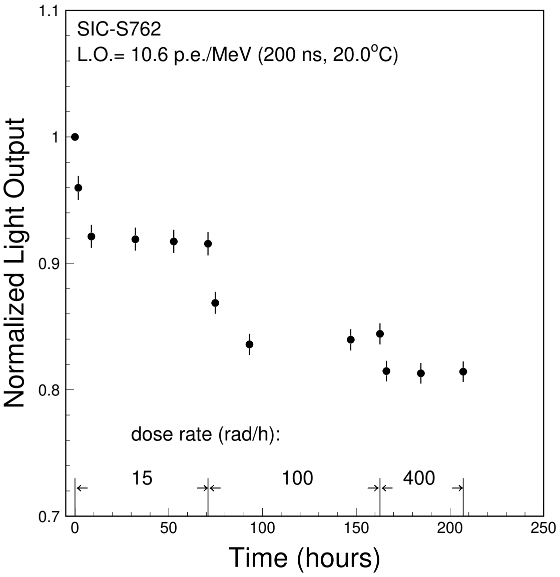

Figure 6.30: Normalized light output is shown as a function of time under irradiations at 15, 100 and 400 rad/h for sample SIC-S762

were modified accordingly, and Y doped samples grown at SIC since then are free from this“instability”. Figures 6.29 and 6.30 show the normalized light output under irradiation at different dose rate for Y doped $PbWO_4$ samples SIC-S643 and SIC-S762. There was no light output increase observed under irradiation.

6.5.3 Optical bleaching

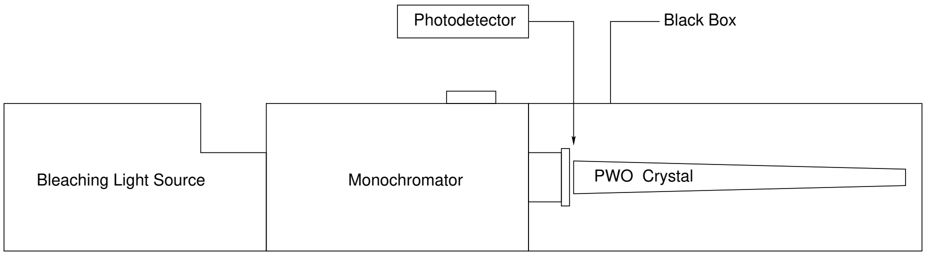

Figure 6.31: Schematic view of a bleaching setup used at Caltech, where light was shot through a monochromator to the back face of the $PbWO_4$ crystal

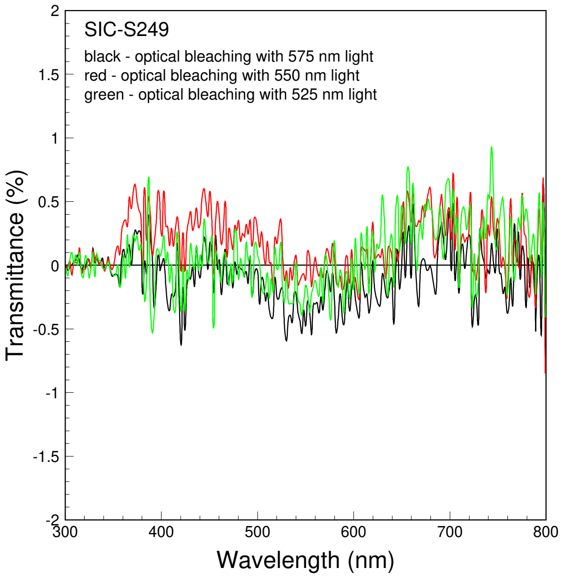

Figure 6.32: Transmittance difference (T_{ob}-T_{max}) of SIC-S249 are plotted as a function of wavelength under optical bleaching by light of different wavelength

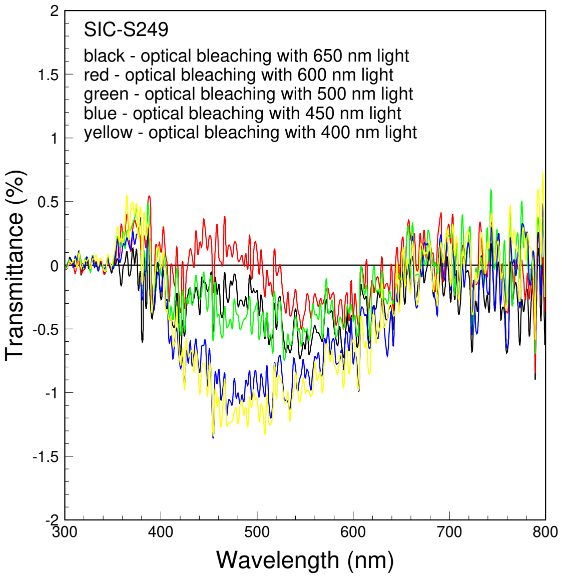

Figure 6.33: Transmittance difference (T_{ob}-T_{max}) of SIC-S249 are plotted as a function of wavelength under optical bleaching by light of different wavelength

Three full size $PbWO_4$ crystals(S249, S301 and S412) produced by SIC were tested. For each run of the optical bleaching, the crystal was irradiated first by using a ^{60}Co source under 1,000 rad/h dose rate at Caltech over 10 hours and then optical bleached under particular wavelength. After over 10 krad ^{60}Coγ-ray irradiation, the transmittance of $PbWO_4$ crystal samples was measured by using a Hitachi U-3210 UV/Visible spectrophotometer. Figure 6.31 shows the setup used for optical bleaching experiment. The light from a monochromator (Baush & Lomb, Grating 1200 Grove/mm) was shot through the large end of a tapered 23 cm long $PbWO_4$ crystal.

To investigated the optical bleaching cross-section, no reflector was placed at any surface of the crystal. The entire bleaching setup was kept in dark. The monochromator was set to have a bandwidth around 10 nm with a rectangular light spot. The crystal was placed in a light sealing black box. Bleaching light from the monochromator (Baush & Lomb, Grating 1200 Grove/mm, 10 nm bandwidth) was shot to the large end of the sample. Typical intensity was determined to be mW/cm^2, depending on the wavelength.

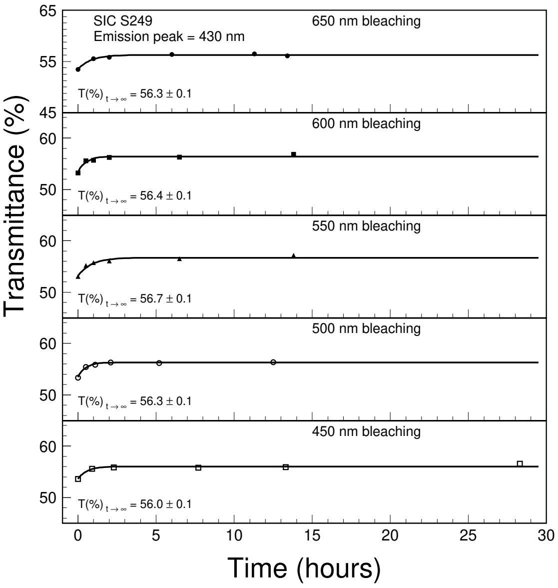

Figure 6.34: 430 nm transmittance under optical bleaching for $PbWO_4$ SIC-S249

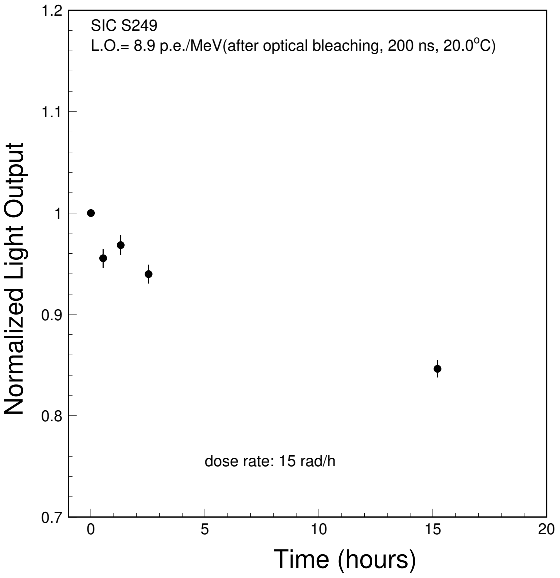

Figure 6.35: Light output after optical bleaching for $PbWO_4$ SIC-S249

Light with different wavelength was used in this experiment. The crystal was illuminated with the light, and transmittance of the crystal was measured frequently until a saturated value was reached. In the measurement, the same procedure was repeated for lights with different wavelengths. The calibration of the light intensity was carried out by using a Hamamatsu Si diode of 1×1 cm^2 with know quantum efficiency. It was found that the photo-current within the light spot at the position where the light entering the crystal is within 5%. This indicates that the light intensity in the light spot has a good uniformity.

Figures 6.32 and 6.33 show the optical bleaching results for the Y doped $PbWO_4$ crystal SIC-S249. In the Figures, T_{ob} represents the transmittance measured after the crystal reached saturation by optical bleaching with a certain wavelength of light. T_{max} represents the "best" transmittance ever been measured for crystals. As shown in Figures 6.32 and 6.33, good wavelength gives a positive result, 550 nm is an effective light for optical bleaching for SIC-S249. Figure 6.34 shows the history of 430 nm transmittance for SIC-S249 under the optical bleaching. It also shows that 550 nm is an effective wavelength for optical bleaching. After optical bleaching, the crystal was irradiated under 15 rad/h dose rate again by using the ^{60}Co source under 15 rad/h dose rate, Figure 6.35 shows the irradiation history. As can be seen, there is no light output increase under irradiation after optimized optical bleaching.

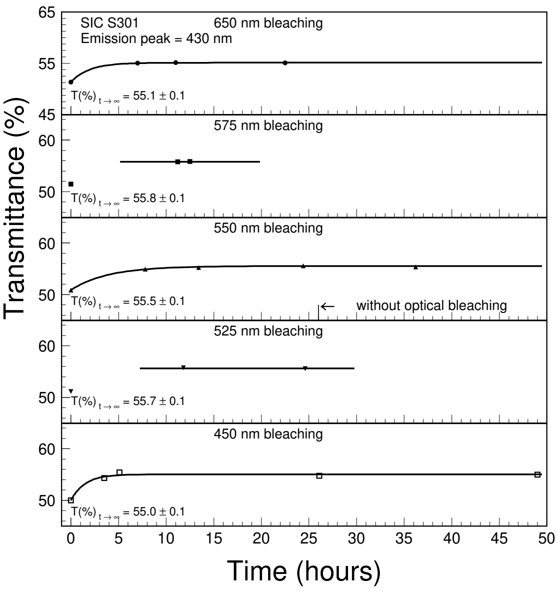

Figure 6.36: 430 nm transmittance for SIC-S301 under optical bleaching

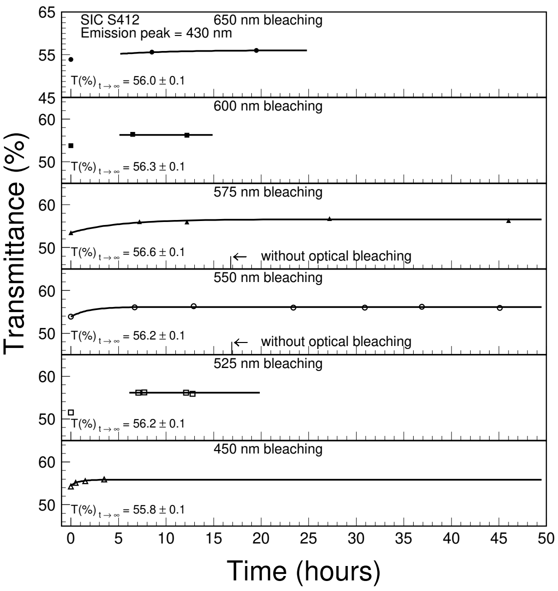

Figure 6.37: 430 nm transmittance for SIC-S412 under optical bleaching

Same optical bleaching test was carried out on the latest $PbWO_4$ samples, S301 and S412, which was delivered in June 1999, produced a similar result, as shown in Figures 6.36 and 6.37. Figures 6.36 and 6.37 show the history of transmittance at 430 nm for S301 and S412 under optical bleaching. In summary, both S301 and S412 have been bleached to a saturated transmittance in around 10h. For these two Y doped $PbWO_4$, it is observed that 575 nm is the effective light for optical bleaching.

6.6 Long Term Stability of PbWO$_4$ Crystals

6.6.1 Long term stability of light output and transmittance

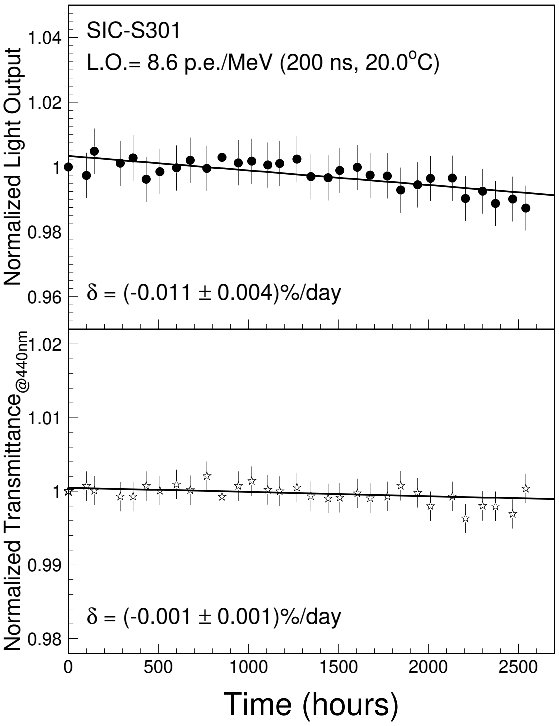

Figure 6.38: Stability of normalized light output and transmittance for Y/Sb doped PbWO$_4$ sample SIC-S301

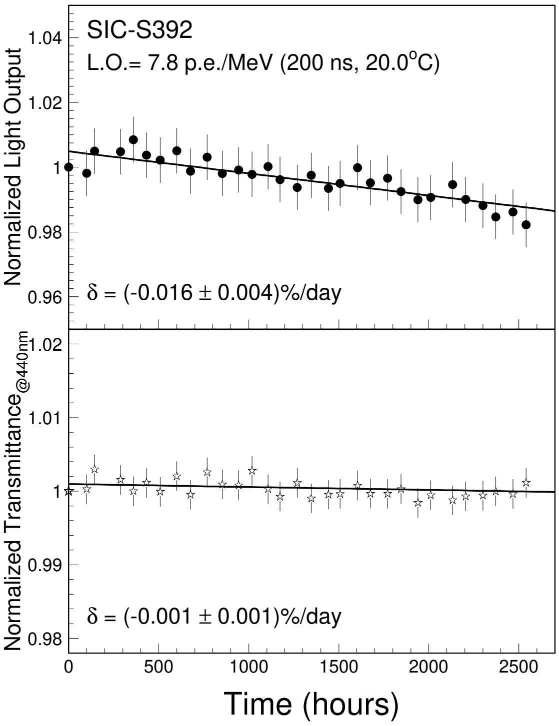

Figure 6.39: Stability of normalized light output and transmittance for Y doped PbWO$_4$ sample SIC-S392

The CMS calorimeter response will need to be stable over long periods of time to avoid repeated calibrations. Since the calorimeter response can be compromised by any one of many elements in a long chain, it is necessary to monitor the stability of response continuously, starting at different points in the chain to distinguish between different effects. One needs to distinguish between degradation of the scintillator or the optical transmission elements, such as may be produced by aging or by radiation damage, and changes in the electronic amplification and digitization system.

After finishing all the routine measurements, an extensive experiment was carried out for six CMS full size PbWO$_4$ samples, i.e. four crystals from SIC(S301, S347, S392 and S412), and two from BTCP(2133 and 2162), to test crystals' long term stability. In a whole period of more than three months, we tested crystals' light output and transmittance without any irradiation, annealing or bleaching, to see their long term stability.

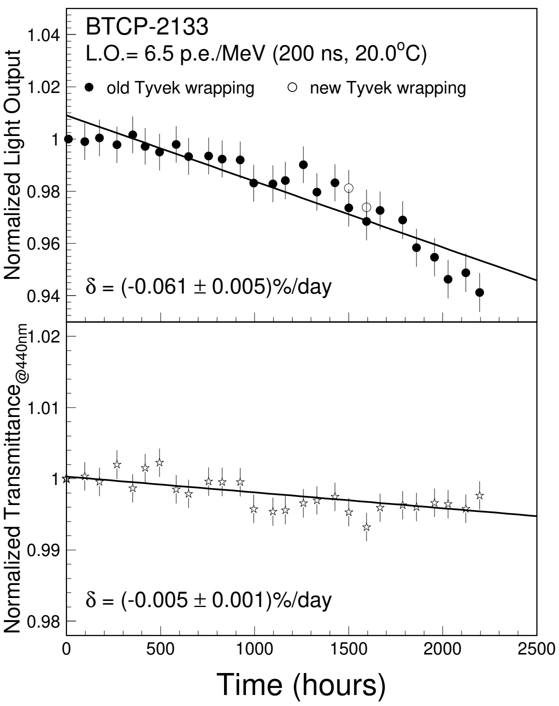

Figure 6.40: Stability of normalized light output and transmittance for Y/Nb doped PbWO$_4$ sample BTCP-2133

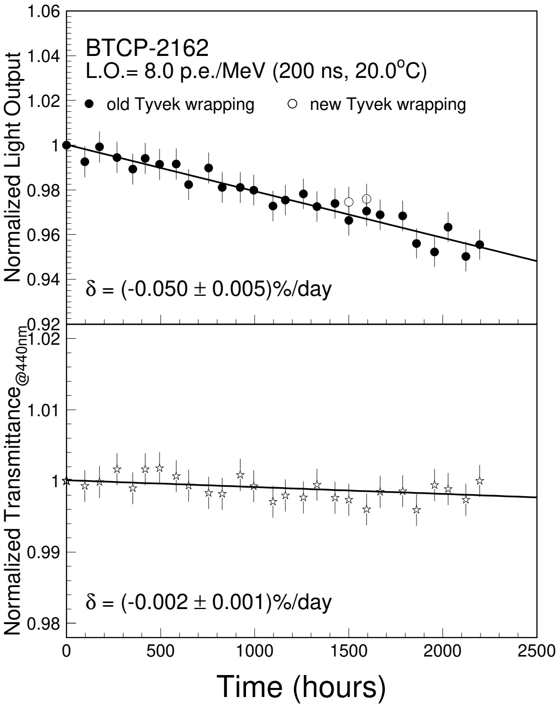

Figure 6.41: Stability of normalized light output and transmittance for Y/Nb doped PbWO$_4$ sample BTCP-2162

Figures 6.38, 6.39, 6.40 and 6.41 show the stability of light output, transmittance at 440 nm and linear fits for Y/Sb doped(SIC-S301), Y doped(SIC-S392) and Y/Nb doped(BTCP-2133 and BTCP-2162) PbWO$_4$ crystal samples from two main PbWO$_4$ producers. The linear fitting slope(δ) represents the variations of light output and transmittance at 440 nm. As seen from figures, the slope for normalized light output for SIC samples is around -0.02%/day, while for BTCP samples, it is less than -0.5%/day. A long term(3 months) stability test indicates possible degradation of both light output and transmittance for Y doped PbWO$_4$ samples. But a further study is needed to understand the origin of this degradation.

6.7 Summary

Yttrium doping is found to shift the emission spectrum to blue with a broad spectrum peaked at 420 nm. It is also effective in reducing slow scintillation component, and leading to PbWO$_4$ crystals with adequate radiation hardness for the CMS experiment. With Y doping it is not necessary to implement oxygen compensation, which is a tedious process and is difficult to control. The concentration of Y ions in PbWO$_4$ crystals is rather uniform. The segregation coefficient of Y in PbWO$_4$ crystals is determined to be 0.91 ± 0.04.

The radiation induced absorption in all samples can be decomposed to two color centers with two common centers peaked at wavelength of 400 nm (3.07 eV) and 540 nm (2.30 eV) with widths of 0.76 and 0.19 eV respectively. These centers are not as deep as that in Sb doped samples[119]. This explains a relatively large dose rate dependence of radiation damage and relatively large damage speed in Y doped PbWO$_4$ crystals.

Light output of early Y doped PbWO$_4$ crystals is sensitive to the temperature of thermal annealing. Pre-existing color centers was formed by inappropriate thermal annealing, was bleach-able by scintillation light, and led to the "instability", i.e. the light output increase under irradiations. These pre-existing color centers were found to be caused by impurities and defects at the tail end of ingots. With refined growth parameters, these pre-existing color centers were eliminated, so that samples grown have no "instability". It was found bleaching light at wavelengths of 550 or 575 nm seem most effective in removing color centers and resetting Y & Y/Sb doped samples to the highest light output. Further study is needed to find a practical solution.

Chapter 7

$PbWO_4$ Light Monitoring

7.1 Introduction

There are two crucial issues for maintaining $PbWO_4$ resolution *in situ* at LHC: the stability of $PbWO_4$ crystals in the LHC radiation environment, and precision calibration *in situ*. After $PbWO_4$ crystals with adequate quality are produced, calibration is the key to the precision of a $PbWO_4$ ECAL *in situ* at LHC. Scientists at CERN will use electron pairs from Z^0 decay and single electrons from W decay to determine the ECAL calibration during LHC operation. The residual damage and recovery of $PbWO_4$ crystals, however, have to be taken care of by light monitoring.

Since the loss of transmittance, or the increase of radiation induced color center density, can be measured by a light monitoring system, we can use variations of transmittance data to estimate variations of light output. This makes possible to use a light monitoring system as inter calibration *in situ* at LHC, and thus makes a precision calorimeter possible by using $PbWO_4$ crystals which suffer from some radiation damage. In this chapter, we report result of a study on correlations between variations of light output and transmittance for the CMS choice of Y doped $PbWO_4$ crystals. The monitoring linearity and sensitivity as a function of wavelength were investigated, and were used to determine the monitoring wavelength so that the best linearity and an adequate sensitivity are achieved.

To cope with the time-dependent performance of CMS $PbWO_4$ crystals, frequent inter-calibration *in situ* at LHC is provided by a light monitoring system, which is

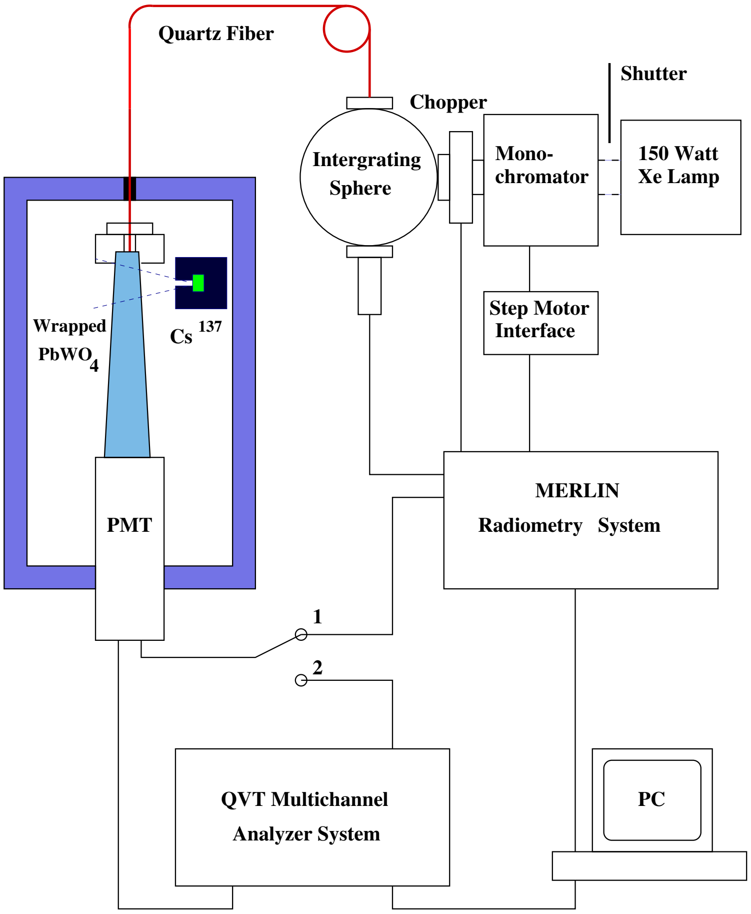

Figure 7.1: The monitoring test bench for the transmittance (position 1) and light output measurement (position 2)

designed to inject light pulses into each individual $PbWO_4$ crystals to measure its optical transmission change and use that to predict its light output change[10]. Monitoring light pulsed are produced by a laser system, and are distributed via an optical fiber system organized into three level: an optical switch[122] which sends pulses to one of 80 calorimeter elements (72 1/2 super module in the barrel and 8 groups of supercrystals in two endcaps), and a two-level distribution system mounted on each calorimeter element which delivers monitoring pulsed to $PbWO_4$ crystals. The monitoring system will measure the variation of the crystals' transmittance continuously, and thus provide inter-calibration continuously. Combined with physics events, such as electron pairs from the Z^0 decays and single electrons from the W decays, the monitoring system is expected to provide calibrations with a precision of 0.4%.

The laser system is required to be able to produce light pulse at two wavelengths[10], one at the emission peak of doped crystals ($\sim$ 440 nm) and other close to emission peak of undoped crystals ($\sim$ 500 nm). The choice of wavelength directly affects monitoring sensitivity and linearity[118]. To provide a continuous monitoring *in situ*, a fraction of the 3.17 μs beam gap in every 88.924 μs[123] during data taking will be used to inject laser light pulse to crystals. The monitoring system will run continuously during data taking to provide inter-calibration.

As discussed above, the crucial inter calibration *in situ* at LHC for CMS ECAL is to be provided by a light monitoring system [10], which uses relative variations of transmittance to estimate relative variations of light output for each individual crystal. Figure 7.1 is a schematic showing a monitoring test bench at Caltech. Monitoring light from a Xenon lamp went through a monochromator and injected to an integrating sphere. The light from one output of the sphere was coupled to the front end of sample through a quartz fiber and an air gap. The light from other output of the sphere was measured by a photo detector as reference. The sample was wrapped with two layers of Tyvek paper and optically coupled to a PMT. The output of the PMT is coupled to either a Merlin from ORIEL through a lock-in amplifier for transmittance measurement (position 1), or a LeCroy QVT multichannel analyzer for light output measurement (position 2).

When the switch is on the position 1, the transmittance as a function of wavelength was measured by using the PMT out out normalize to that of reference detector. The reference detector was thermo electrically cooled to reduce systematic uncertainties caused by fluctuations of the intensity of the light source. The PMT source was chopped and went through a lock-in amplifier to suppress the noise. Figure 7.2 shows a distribution of PMT readout normalized to reference detector on sphere, taken for

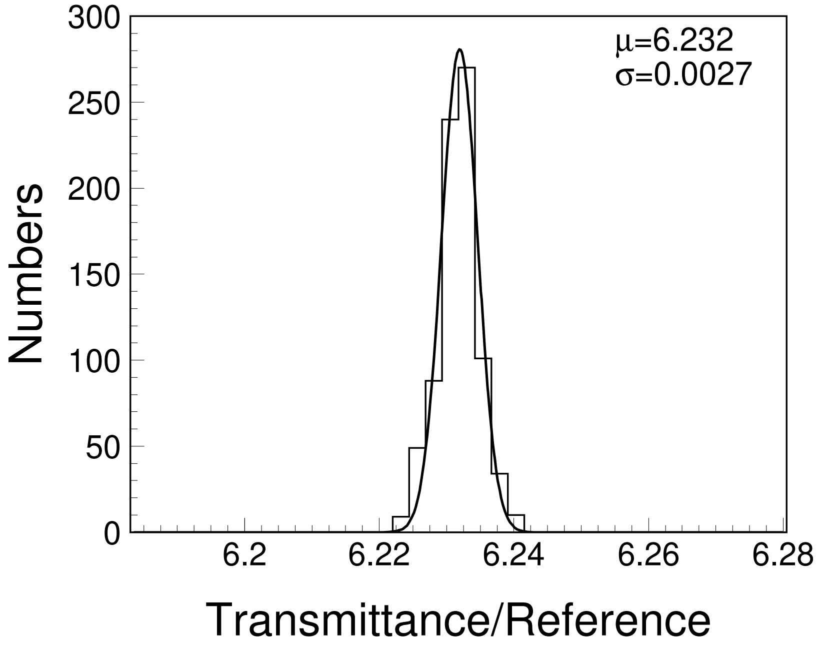

Figure 7.2: Distribution of PMT readout (position 1) normalized to reference detector on sphere, taken in 8 hours

a sample in 8 hours. A Gaussian fit is also shows in the figure together with the fit result of average (μ) and width (σ). The stability, defined as σ/μ of the fit, was found to be better than 0.1%. A similar stability was obtained by level 1 splitter in CMS ECAL monitoring system during beam test for a period of a few weeks[120].

When the switch is in position 2, the shutter at the input of monochromator is closed so that there is no interference between scintillation light and monitoring light source. The scintillation light output of the sample was measured by suing a small ^{137}Cs source and a LeCroy 3001 QVT in the Q mode. The Cs spectrum was fit to a simple Gaussian to determine eh peak position which then be converted to the light output in p.e./MeV by using a calibration of the single photoelectron peak. A precision of 0.6% were achieved for the light output measurement.

To simulate expected radiation environment *in situ* at LHC, the sample was either irradiated by a ^{60}Co source under 15 to 1,000 rad/h or under recovery after irradiation.

This setup simulates what to be used *in situ* at LHC except that the readout detector is a PMT which covers entire back face of the sample, while photo detector used in CMS ECAL is Si avalanche photo diode(APD), which covers only a small fraction of sample back face.

7.2 Correlations between Variations of Transmittance and Light Output

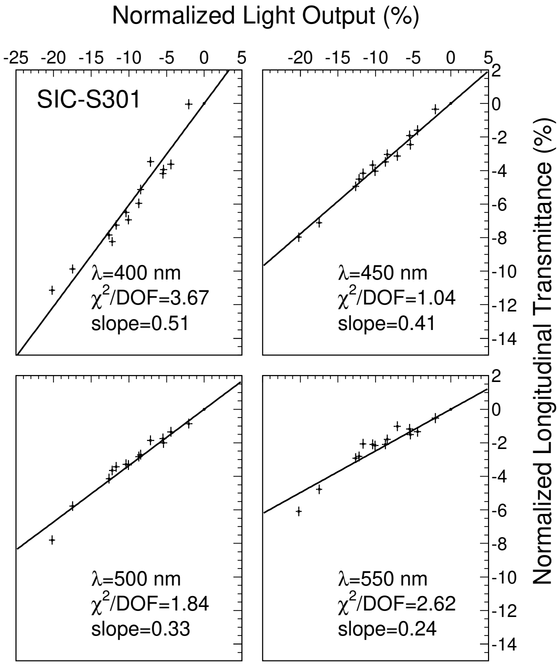

Figure 7.3: Correlations between relative variations of transmittance and light output are shown for four monitoring wavelengths for a Y/Sb double doped sample SIC-S301

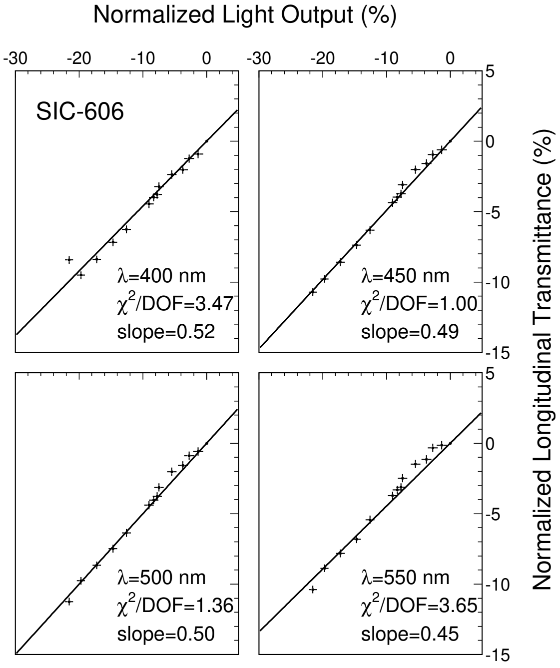

Figure 7.4: Correlations between relative variations of transmittance and light output are shown for four monitoring wavelengths for a Y doped sample SIC-606

Figure 7.3 and 7.4 show correlations between relative variations of transmittance (ΔT/T) and light output (ΔLY/LY) for monitoring light at four different wavelengths: 400, 450, 500 and 550 nm for a Y/Sb double doped sample SIC-S301 and Y doped sample SIC-606. The correlation was fit to a linear function:

$$\frac{\Delta \mathrm{T}}{\mathrm{T}} = slope \times \frac{\Delta \mathrm{LY}}{\mathrm{LY}} \tag{7.1}$$

The result of the fit, including the χ^2/DoF and the slope, is also listed in the figure. The error on the slope is about 2 to 3%, dominated by the statistical error of the fit. While the slope represents the sensitivity for PbWO$_4$ monitoring, the χ^2/DoF represents the linearity of the fit. From the figure it is clear that the linearity is generally good when light output loss is less than 15%, and some systematic deviations exist for monitoring light of 400, 500 and 500 nm, as compared to 450 nm, since not all wavelengths are adequate for the monitoring.

7.3 Monitoring Sensitivity, Linearity and Wavelength Determination for PbWO$_4$ Light Monitoring

Figure 7.5 and 7.6 show monitoring sensitivity (solid dots, left scale), or slope, defined as $\frac{\Delta \mathrm{T}}{\mathrm{T}}/\frac{\Delta \mathrm{LY}}{\mathrm{LY}}$, and linearity (open dots, right scale), defined as χ^2/DoF, as function of monitoring wavelength for undoped(SIC-210), Y doped(SIC-S412), Sb doped(SIC-274), Y/Sb double doped(SIC-S301), La doped(BTCP-1971) and Y/Nb double doped(BTCP-2133) PbWO$_4$ samples. Also shown in the figure is the PMT quantum efficiency weighted radio luminescence (dashed line). While a shorter monitoring wavelength is preferred for a better sensitivity, the best linearity is achieved at around 445 nm which coincides with the peak of radio luminescence.

All these samples have a better monitoring sensitivity at shorter wavelength and the best linearity around the peak of PMT quantum efficiency weighted radio luminescence. The better monitoring sensitivity at shorter wavelength is understood because of the poorer initial transmittance as compared to that at longer wavelength.

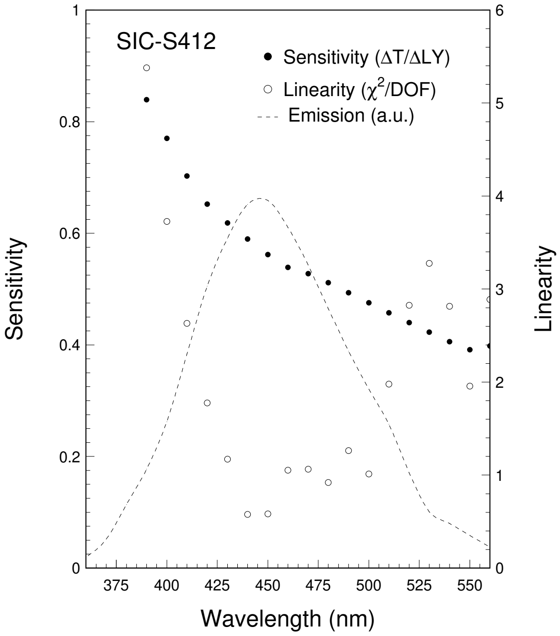

Figure 7.5: Monitoring sensitivity and linearity are shown as function of wavelength together with radio luminescence for SIC-S412

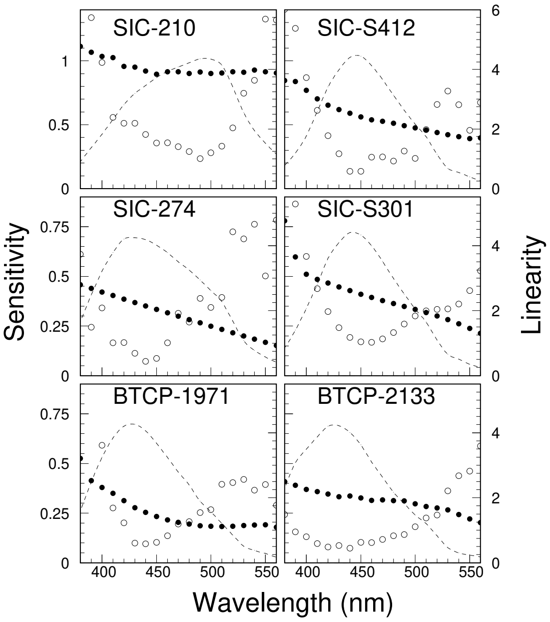

Figure 7.6: Monitoring sensitivity and linearity are shown as function of wavelength for six $PbWO_4$ samples

The best linearity around the peak of radio luminescence is caused by two radiation induced color centers as shown in figures 6.21, 6.22, 6.23 and 6.24 discussed in Section 6.4.5. Since the two color centers are peaked well apart at two sides of the peak of radio luminescence(stars) and with different damage and annihilation constants, 440 nm was chosen as monitoring light wavelength so that adequate sensitivity and best linearity is achieved.

The evident correlation between the linearity and the emission spectrum can be explained by the radiation induced color centers. Since the radio luminescence peak is located between two radiation induced color centers only monitoring wavelength in the vicinity of emission peak can properly sample different kinetics of these two centers. The choice of CMS $PbWO_4$ ECAL monitoring wavelength thus will be aiming for the best linearity, i.e. in the vicinity of the radio luminescence emission peak.

Table 7.1: Monitoring test bench result

Sample ID	Dopant	Sensitivity(ΔT/ΔLY) 440 nm	490 nm	Linearity (χ^2/DOF) 440 nm	490 nm
SIC-S301	Y/Sb	0.43±0.01	0.35±0.01	1.17	1.59
SIC-S347	Y/Sb	0.60±0.01	0.55±0.01	0.63	0.99
SIC-S392	Y	0.51±0.01	0.44±0.01	0.94	1.11
SIC-S412	Y	0.59±0.03	0.49±0.03	0.58	1.26
SIC-S762	Y	0.50±0.01	0.48±0.01	0.92	1.14
BGRI-824	Y	0.48±0.01	0.49±0.01	0.42	0.76
BGRI-826	Y	0.42±0.01	0.42±0.01	0.71	0.96
BTCP-2133	Y/Nb	0.33±0.01	0.31±0.01	0.45	0.87
BTCP-2162	Y/Nb	0.28±0.01	0.25±0.01	0.62	1.29
BTCP-5615	Y/Nb	0.33±0.01	0.30±0.01	0.78	1.42
BTCP-5618	Y/Nb	0.29±0.01	0.27±0.01	0.48	0.92
BTCP-5658	Y/Nb	0.32±0.01	0.32±0.01	1.04	2.68

Table 7.1 lists result of our monitoring test bench for seven R&D $PbWO_4$ samples produced in China: SIC or Beijing Glass Research Institute (BGRI), and five preproduction samples produced in BTCP. Note, all are CMS full size samples of 25 radiation length, or 23 cm long, with dimension of 2.3 × 2.3 cm^2 tapered to 2.6 × 2.3 cm^2. The sample ID, with SIC, BGRI and BTCP representing SIC, BGRI and BTCP respectively, the dopant in the melt and sensitivity and linearity at 440 nm and 490 nm are listed. All samples are mainly Y doped and have similar emission spectrum peaked at 420 nm. We, therefore, choose 440 nm as the monitoring wavelength[118]. Since CMS uses only Y doped $PbWO_4$ crystals which has an emission pealed at 420 nm, this wavelength is now used as a cross-check wavelength.

7.4 Summary

A key issue of wavelength choice was resolved by a monitoring test bench. Seven Y doped R&D $PbWO_4$ samples grown by the Bridgman method in China and five Y/Nb double doped preproduction samples grown by the Czochralski method in Russia were measured. Consistent sensitivity and linearity were found for crystals grown by the same technology. Because it is less transparent at short wavelengths, the monitoring sensitivity for $PbWO_4$ crystal is better at short wavelength. The best linearity, around emission peak is understood to be caused by two color centers peaked at two sides of emission and with different damage/recover speed. To achieve the best linearity and adequate sensitivity, 440 nm is chose as the monitoring wavelength.

Since $PbWO_4$ photo detector used in CMS ECAL is Si avalanche photo diode, which has a flat quantum efficiency as compared to that of the PMT with bi-alkali photo cathode used in this investigation, it is expected that the monitoring wavelength of choice is around 440 nm for all tri-valent or Sb doped $PbWO_4$ crystals. The undoped crystal, however, would require a monitoring wavelength around 510 nm. And thus the variations of transmission due to irradiation/recovery for $PbWO_4$ crystals will be monitored by a light injection system in the calorimeter, and a correction can be established and applied.

Chapter 8

Conclusion

In this thesis, I present a study of lead tungstate crystals and improvement of radiation hardness. Detailed measurements of properties for mainly Sb and Y doped $PbWO_4$ crystals, radiation damage and analysis on the radiation damage mechanisms for $PbWO_4$ crystals have been presented. Most $PbWO_4$ samples were produced at SIC, BGRI and BTCP during 1998, 1999 and 2000.

A study on Sb doping in lead tungstate crystals is presented in the thesis. As compared to undoped $PbWO_4$ crystal Sb doping is found to reduce slow scintillation components. Result of GDMS trace analysis on raw materials and crystals shows that the concentration of Sb ions in $PbWO_4$ crystals is inhomogeneous. The segregation coefficient of Sb in $PbWO_4$ crystals is determined to be 0.052 ± 0.004, indicating the difficulty of Sb ions to enter the $PbWO_4$ lattice.

The scintillation emission and longitudinal transmittance spectra, light output, decay kinetics and radiation damage were measured for Sb doped $PbWO_4$ crystals. A broad radio luminescence peaked at the blue (430 to 450 nm) was observed for Sb doped $PbWO_4$ crystals, and it has a 50 to 60 nm blue shift as compared to that of photo luminescence. This shift is explained by not energetic enough photons of the UV excitation light.

The radiation induced absorption in all Sb doped $PbWO_4$ samples can be decomposed to two color centers with a common center peaked at wavelength of 353 nm (3.51 eV) of a width from 0.25 to 0.54 eV. The other less energetic center, however, is peaked at 537 nm (2.31 eV) for samples prepared with oxygen compensation. These centers are more deeper than radiation induced color centers in trivalent doped samples (3.07 and 2.30 eV). These explains a smaller dose rate dependence of radiation damage in Sb doped $PbWO_4$ crystals.

It is found that Sb doping alone is not sufficient to produce radiation hard lead tungstate crystals, and post growth oxygen compensation is required. Oxygen compensation is also found no effect on scintillation and decay kinetics for Sb doped $PbWO_4$ crystals. Because Sb ions function as pentavalent in high temperature, Sb doping does not make effective compensation for the intrinsic oxygen vacancies in $PbWO_4$ crystals. The work of this thesis confirmed that post annealing treatment under oxygen-rich atmosphere is proved effective for improving the radiation resistance of Sb doped $PbWO_4$ crystal.

Yttrium doping is found to shift the emission spectrum to blue with a broad spectrum peaked at 420 nm. It is also effective in reducing slow scintillation component, and leading to $PbWO_4$ crystals with adequate radiation hardness for the CMS experiment. With Y doping it is not necessary to implement oxygen compensation, which is a tedious process and is difficult to control. The concentration of Y ions in $PbWO_4$ crystals is rather uniform. The segregation coefficient of Y in $PbWO_4$ crystals is determined to be 0.91±0.04.

The radiation induced absorption in all samples can be decomposed to two color centers with two common centers peaked at wavelength of 400 nm (3.07 eV) and 540 nm (2.30 eV) with widths of 0.76 and 0.19 eV respectively. These centers are not as deep as that in Sb doped samples[119]. This explains a relatively large dose rate dependence of radiation damage and relatively large damage speed in Y doped $PbWO_4$ crystals.

Light output of early 1999 Y doped $PbWO_4$ crystals is sensitive to the temperature of thermal annealing. Pre-existing color centers was formed by inappropriate thermal annealing, was bleach-able by scintillation light, and led to the "instability", i.e. the light output increase under irradiations. These pre-existing color centers were found to be caused by impurities and defects at the tail end of ingots. With refined growth parameters, these pre-existing color centers were eliminated, so that samples grown have no "instability". New samples grown in the year of 2000 with revised parameters at SIC do not have "instability". Latest samples from SIC have light yield comparable with the latest Nb/Y doped samples from BTCP, but a better radiation hardness. It was found bleaching light at wavelengths of 550 or 575 nm seem most effective in removing color centers and resetting Y & Y/Sb doped samples to the highest light output. Further study is needed to find a practical solution.

Depending on initial conditions, BTCP Y/Nb doped samples may have damage speed too fast, while some SIC Y and Y/Sb doped samples may have recovery speed too fast. Further studies needed to find damage/recovery speed *in situ* at LHC (temperature and dose rate) and consequence to monitoring frequency. A long term(3 months) stability test indicates possible degradation of both light output and transmittance for Y and Y/Nb doped $PbWO_4$ samples. But a further study is needed to understand the origin of this degradation.

The variations of transmission due to irradiation/recovery will be monitored by a light injection system in the calorimeter, and a correction can be established and applied. Because it is less transparent at short wavelengths, the monitoring sensitivity for $PbWO_4$ crystal is better at short wavelength. The best linearity, however, can only be achieved with monitoring light wavelength around the peak of radio luminescence weighted with quantum efficiency of photo detector. Since $PbWO_4$ photo detector used in CMS ECAL is Si avalanche photo diode, which has a flat quantum efficiency as compared to that of the PMT with bi-alkali photo cathode used in this investigation, it is expected that the monitoring wavelength of choice is around 440 nm for all trivalent or Sb doped $PbWO_4$ crystals. The undoped crystal, however, would require a monitoring wavelength around 510 nm.

References

[1] M. Oreglia *et al.*, *Phys. Rev. D***25** 2295 (1982).

[2] E. Bloom and C, Peck, *Ann. Rev. Nucl. Part. Sci.* **33** 143-197 (1983).

[3] T. Böringer *et al.*, *Phys. Rev. Lett.* **44**: 1111 (1980); G. Mageras *et al.*, *Phys. Rev. Lett.* **46**: 1115 (1981).

[4] L3 Collaboration, *Nucl. Instr. and Meth.* **A289** 35 (1990).

[5] Y. Kubota *et al.*, *Nucl. Instr. and Meth.* **A320** 66 (1992).

[6] E. Aker *et al.*, *Nucl. Instr. and Meth.* **A321** 69 (1992).

[7] K. Arisaka *et al.*, *KTeV Design Report*, **FN-580**, January (1992).

[8] *BaBar* Collaboration, *Technical Design Report*, **SLAC-R-95-457** (1995).

[9] BELLE Collaboration, *Technical Design Report*, **KEK Report 95-1** (1995).

[10] CMS Collaboration, *The Electromagnetic Calorimeter Technical Design Report*, CERN/LHCC 97-33 (1997).

[11] S. Mrenna *et al.*, **C**ALT 68-1856, June 1993.

[12] R.Y. Zhu and H. Yamammoto, **C**ALT 68-1802, July 1992.

[13] R.Y. Zhu, **C**ALT 68-1777, November 1991.

[14] R.Y. Zhu *et al.*, *Nuclear Physics B (Proc. Suppl.)* **44** 88-108 (1995).

[15] *GEM Letter of Intent*, **SSCL SR-1184**, November (1991).

[16] *L3P Letter of Intent*, CERN/LHCC 92-5, LHCC/I3 (1992).

[17] G. Gratta, H. Newman and R.Y. Zhu, *Annu. Rev. Nucl. Part. Sci.* **44** 453 (1994).

[18] CMS Collaboration, *The Compact Muon Solenoid - Technical Proposal*, CERN/LHCC 94-38 LHCC/P1, Dec. (1994).

[19] C. Seez *et al.*, **CMS TN/92-056** (1992).

[20] Y. Kubota *et al.*, *The CLEO II detector*, **CLNS 91/1122**, 1991.

[21] Harshaw-QS, *Scintillation Detectors*, (March 1992).

[22] BDH Limited, *BDH Crystran — Monocrystal Products for Optics*, (January 1990).

[23] C. Woody *et al.*, *IEEE Trans.* **NS-37** 492 (1990).

[24] C. Woody *et al.*, *IEEE Trans.* **NS-39** 524 (1992).

[25] Z.Y. Wei and R.Y. Zhu, *Nucl. Instr. and Meth.* **A326** 508 (1993).

[26] P. Schotanus, *SCIONIX Internal Report* **93002**, May 1993. **A326** 508 (1993).

[27] P. Schotanus *et al.*, *Nucl. Instr. and Meth.* **A238** 564 (1985).

[28] M. Kobayashi *et al.*, *Nucl. Instr. and Meth.* **A270** 106 (1988).

[29] R.Y. Zhu, *Nucl. Instr. and Meth.* **A340** 442 (1994).

[30] D. Anderson, *IEEE Trans.* **NS-36** 137 (1989).

[31] W. Moses and S. Derenzo, *IEEE Trans.* **NS-36** 173 (1989).

[32] Crystal Clear Collaboration, *Nucl. Instr. and Meth.* **A332** 373 (1993).

[33] There are many literatures dicussing color centers in solids, for example, J.H. Crawford and L.M. Slifkin, *Point Defects in Solids*, Plenum Press, New York (1972).

[34] L. Dafinei *et al.*, in *Scintillator and Phosphor Materials*, MRS Symposium 348, ed. M Weber *et al.*, 99 (1994).

[35] V.A. Kachanov *et al.*, in *Calorimetry in High Energy Physics*, World Scientific, ed. A. Menzione and A. Scribano, 292 (1993).

[36] M. Kobayashi *et al.*, *Nucl. Instr. and Meth.* **A335** 509 (1993).

[37] E. Dally and R. Hofstadter, *Rev. Sci. Instr.* **39** 658 (1968).

[38] D. Anderson *et al.*, *Nucl. Instr. and Meth.* **A290** 385 (1990).

[39] C. Woody *et al.*, *IEEE Trans.* **NS-40** 546 (1993).

[40] C. Melcher and J. Schweitzer, *Nucl. Instr. and Meth.* **A314** 212 (1992).

[41] C. Melcher and J. Schweitzer, *IEEE Trans.* **NS-39** 502 (1992).

[42] D. Anderson *et al.*, *Nucl. Instr. and Meth.* **A342** 473 (1994).

[43] C. Wuest *et al.*, *talk in Crystal Clear Collaboration Meeting* (December 1993).

[44] M. Kobayashi *et al.*, *Nucl. Instr. and Meth.* **A333** 429 (1993).

[45] H. Suzuki, Ph. D. Thesis, Caltech (1994).

[46] M. Kobayashi and S. Sakuragi, *Nucl. Instr. and Meth.* **A254** 275 (1987); C. Bieler *et al.*, *Nucl. Instr. and Meth.* **A234** 435 (1985); H. Grassmann *et al.*, *Nucl. Instr. and Meth.* **A228** 323 (1985); S. Schlogl *et al.*, *Nucl. Instr. and Meth.* **A242** 89 (1985); D. Hitlin and G. Eigen, in reference [124] p.467. C. Woody *et al.*, *IEEE Trans.* **NS-37** 492 (1990) and **NS-39** 524 (1992); and Z.Y. Wei and R.Y. Zhu, *Nucl. Instr. and Meth.* **A326** 508 (1993).

[47] S. Majewski and D. Anderson, *Nucl. Instr. and Meth.* **A241** 76 (1985); S. Majewski and M. Bently, *Nucl. Instr. and Meth.* **A260** 373 (1987); A. Caffreay *et al.*, *IEEE Trans.* **NS-33** 230 (1986); M. Murashita *et al.*, *Nucl. Instr. and Meth.* **A243** 67 (1986); A. Marakami *et al.*, *Nucl. Instr. and Meth.* **A253** 163 (1986) and **A301** 435 (1991); C. Woody *et al.*, *IEEE Trans.* **NS-36** 536 (1989) and **NS-39** 123 (1992); and Z.Y. Wei *et al.*, *Nucl. Instr. and Meth.* **B61** 61 (1991).

[48] D.A. Ma and R.Y. Zhu, *Nucl. Instr. and Meth.* **A332** 113 (1993).

[49] M. Kobayashi *et al.*, *Nucl. Instr. and Meth.* **A335** 509 (1993); Crystal Clear Collaboration, **CERN-DRDC-93-31** (1993); C. Woody *et al.*, in *Scintillator and Phosphor Materials*, ed. M. Weber *et al.*, MRS Symposium Proceedings Volume 348, 475 (1994); and R.Y. Zhu *et al.*, *Report to CMS ECAL Institute Board*, December 1994.

[50] M. Kobayashi *et al.*, *Nucl. Instr. and Meth.* **A206** 107 (1983); C. Laviron and P. Lecoq, *Nucl. Instr. and Meth.* **A227** 45 (1984); G. Bobbink *et al.*, *Nucl. Instr. and Meth.* **A227** 470 (1984); and C. Bieler *et al.*, *Nucl. Instr. and Meth.* **A234** 435 (1985).

[51] R.Y. Zhu *et al.*, *Nucl. Instr. and Meth.* **A302** 69 (1991).

[52] Z.Y. Wei *et al.*, *Nucl. Instr. and Meth.* **A297** 163 (1990).

[53] E. Auffray *et al.*, paper in *Proceedings of SCINT97 Int'l Conf.*, Shanghai, September 1997.

[54] Z.W. Yin *et al.*, paper in *Proceedings of SCINT97 Int'l Conf.*, Shanghai, September 1997.

[55] H.F. Chen *et al.*, *Nucl. Instr. and Meth.* **A414** (1998) 149.

[56] P. Lecoq *et al.*, *Nucl. Instr. and Meth.* **A403** (1998) 302, *Nucl. Instr. and Meth.* **A402** (1998) 75 *Nucl. Instr. and Meth.* **A365** (1995) 291.

[57] M. Kobayashi *et al.*, *Nucl. Instr. and Meth.* **A406** (1998) 442, *Nucl. Instr. and Meth.* **A404** (1998) 149, *Nucl. Instr. and Meth.* **A399** (1997) 261, *Nucl. Instr. and Meth.* **A373** (1996) 333.

[58] M. Korzhik *et al.*, *Rad. Meas.* **29**(1) (1998) 27, *J. Allo. & Comp*, **238** (1996) 46, *Phys. Stat. Sol.* **a156** (1996) 493 and *Phys. Stat. Sol.* **a154** (1996) 779.

[59] M. Nikl *et al.*, *Phys. Stat. Sol.* **a164** (1997) R9, *J. Appl. Phys. Lett.* **82**(11) (1997) 5758, *J. Appl. Phys. Lett.* **71**(26) (1997) 3755, *Phys. Stat. Sol.* **b196** (1996) K7 and *Phys. Stat. Sol.* **b195** (1996) 311.

[60] R.Y. Zhu *et al.*, *Nucl. Instr. and Meth.* **A413** (1998) 297, *IEEE Trans. Nucl. Sci.* **NS-45** (1998) 686, *IEEE Trans. Nucl. Sci.* **NS-44** (1997) 468, *Nucl. Instr. and Meth.* **A376** (1996) 319, *IEEE-NUCL-S* **V43** (1996) 1585.

[61] E. Auffray *et al.*, *Nucl. Instr. and Meth.* **A385** (1997) 425.

[62] E. Auffray *et al.*, *Nucl. Instr. and Meth.* **A412** (1998) 223.

[63] L. Leciejewicz, *Z. fur. Krist.*, **121** (1965) 158; P.W. Richter *et al.*, *Acta Cryst.*, **B32** (1976) 928; T. Fujita *et al.*, *Acta Cryst.*, **B33** (1977) 162.

[64] R.Y. Zhu *et al.*, in *Proc. of the 6th Int. Conf. on Calorimetry in High Energy Physics*, ed. A. Antonelli *et al.*, Frascati Physics Series (1996) 577.

[65] E. Auffray *et al.*, in *Proceedings of SCINT95 Int'l Conf.* Delft, August 1995, p.282.

[66] R.Y. Zhu *et al.*, *Nucl. Instr. and Meth.* **A376** 319 (1996); C. Woody *et al.*, in *Proceedings of SCINT95 Int'l Conf.* Delft, August 1995 and *IEEE-NUCL-S* **V43** (1996) 1585.

[67] C. Lazik of Charles Evans and Associates, private communications.

[68] Shiva Technologies West, Inc., 16305 Caputo Drive Suite C, Morgan Hill, CA 95037.

[69] A. Annenkov *et al.*, **CMS Note 1997/009** (1997); **CMS Note 1997/055** (1997).

[70] E. Auffray *et al.*, **CMS Note 1997/054** (1997).

[71] R.Y. Zhu, *IEEE Trans. Nucl. Sci.* **NS-44** 468 (1997).

[72] H.F. Chen *et al.*, *Proc. Int. Workshop on Lead Tungstate Crystals*, Rome (Italy, October 1998), **ETH Preprint ETHZ-IPP PR-98-07** (Zürich, Switzerland).

[73] R. Shaw *et al.*, *Am. Mineral.* **40** 993 (1995).

[74] F. A. Kröger, *Some Aspects of the Luminescence of Solids* (Elsevier, New York, 1948).

[75] D. A. Pinnow *et al.*, *Appl. Phys. Lett.* **15** 83 (1969).

[76] J. Czochralski, *Z. Phys. Chem.*, **92**, 219 (1918).

[77] K.Nassau *et al.*, *J. Amer. Ceram.Soc.*, **45**, 474 (1962b)

[78] J. C. Lewis *et al.*, *Sol. State Elect.*,**6**,251 (1969).

[79] W. Bardsley *et al.*, *J. Cryst. Growth*, **16**, 277 (1972).

[80] T.R.Kyle *et al.*, *Mat. Res. Bull.*, **8**,443, (1973).

[81] W.C.Dash *et al.*, *J. Appl. Phys.*, **30**, 459, (1959).

[82] T.Arizumi *et al.*, *Japan J. Appl. Phys.*, **8**, 1091 (1969).

[83] J.R.Carruthers *et al.*, *J. Electronics Soc.*, **114**,959 (1967); *J. Appl. Phys.*, **39**, 5205 (1968).

[84] D.S. Robertson *et al.*, *Brit. J.Appl.Phys.*,**17**, 1047 (1966).

[85] B.M.Turovsky *et al.*, *Sov. Phys. (Cryst.)*, **6**, 606 (1962).

[86] J.C.Brice *et al.*, *J. Cryst. Growth*, **11**, 133 (1971).

[87] P.W.Bridgman, *Proc. Amer. Acad. Arts. Sci.*,**60**,305 (1925).

[88] A.J.Ansley, *Temperature Control*, **Chapman and Hall, London**, 1942.

[89] M.Ishii *et al.*, *Nucl. Instr. and Meth.*, **A376**, 203 (1996).

[90] M.Lebeau *et al.*, in: H.J.Scheel(Ed.), *Lecture Notes on 1st Int. School on Crstal Growth Tech.*, Beatenberg, p.672 (1998).

[91] Z.W. Yin *et al.*, “Research and Development Works On $PbWO_4$Crystals in Shanghai Institute of Ceramics”, *Proc. SCINT99* held in Moscow, 1999.

[92] S.Baccaro *et al.*, *Phys. Stat. Sol.* **A164** (1997) R9.

[93] J.A.Burton *et al.*, *J. Chem. Phys.*, **21**, 1987 (1953).

[94] E. Auffray *et al.*, *Nucl. Instr. and Meth.* **A402** (1998) 75.

[95] S. Baccaro *et al.*, *Proc. SCINT97*, Shanghai (1997) 203.

[96] M.Kobayashi *et al.*, *Nucl. Instr. and Meth.* **A373** 333 (1996).

[97] R.Y. Zhu *et al.*, *Nucl. Instr. and Meth.* **A413** (1998) 297.

[98] R.Y. Zhu *et al.*, *IEEE Trans. Nucl. Sci.* **NS-45** (1998) 686.

[99] R.Y. Zhu *et al.*, *IEEE Trans. Nucl. Sci.* **NS-44** (1997) 468.

[100] R.Y. Zhu *et al.*, *Nucl. Instr. and Meth.* **A376** (1996) 319.

[101] R.Y. Zhu *et al.*, *IEEE-NUCL-S* **V43** (1996) 1585.

[102] J.C.Brice, *The Growth of Crystals from the Melt*, North Holland, Amsterdam (1973).

[103] *International Series of Monographs on the Science of the Solid State, v.6*, **Crystal Growth**, ed. B.R.Pamplin, 1975.

[104] R.Y. Zhu *et al.*, in *Proc. of the 6th Int. Conf. on Calorimetry in High Energy Physics*, ed. A. Antonelli *et al.*, Frascati Physics Series (1996) 589.

[105] K. Shmakov, **GEM TN-92-143**, August (1992).

[106] M. Oreglia, Ph.D. Thesis, Stanford University, SLAC Report 236 (1980).

[107] D.Graham and C. Seez, **CMS Note 1996-002.**

[108] C.D.Ambrosio *et al.*, Nucl. Instr. and Meth. A388 (1997) 119.

[109] H.Hofer *et al.*, Nucl. Instr. and Meth. A433 (1999) 630.

[110] Qun Deng, The study of Radiation Hardness of CsI(Tl) and $PbWO_4$ crystals, Ph.D. thesis at SIC, June (1998).

[111] Q.Deng *et al.*, Nucl. Instr. and Meth. A438 (1999) 415.

[112] G. Bakhshiva & A. Morozov, Sov.J.Opt.Technol. **44**(9), Sept, 1977.

[113] Piotr A. Rodnyi, **Physical Process in Inorganic Scintillators**, CRC Press LLC, (1997) 37.

[114] G.Basti *et al.*, **CMS IN 1997/033**.

[115] G. Drobychev *et al.*, **CMS Note 1997/036**.

[116] J.D. Valentine *et al.*, *IEEE Trans. Nucl. Sci.*, **40** (1993) 1267.

[117] H.F. Chen *et al.*, *Proc.SCINT99*, Moscow(1999).

[118] X.D.Qu *et al.*, **CMS NOTE 1999/069**, in *Proc. SCINT99*, Moscow (1999), accepted by *IEEE Trans. Nucl. Sci.*

[119] X.D.Qu *et al.*, *A Study on Sb Doping in Lead Tungstate Crystals*, to be published in *Nucl. Instr. and Meth.*

[120] J.Rander *et al.*, in *in Proceedings fo the Eighth International Conference on Calorimetry in High Energy Physics*, Ed. G. Barreira *et al.*, World Scientific (2000) 423.

[121] L.Y.Zhang *et al.*,**CMS Internal Note 1999/014** (1999).

[122] L.Y.Zhang and R.Y.Zhu, **CMS Internal Note 1998/031** (1998).

[123] The LHC Study Group, *The LHC Conceptual Design Report*, **CERN/AC/95-05 46** (1995).

[124] *Heavy Scintillators for Scientific and Industrial Applications*, Editions Frontieres Volume C58, ed. F. Nataristefani *et al.*, September 1992.

Publications

1. X.D.Qu *et al.*, *Radiation Induced Color Centers and Light Monitoring for Lead Tungstate Crystals* **CMS NOTE 1999/069**, in *Proc. SCINT99*, Moscow (1999), accepted by *IEEE Trans. Nucl. Sci.*;in *Proceedings of the Fifth International Conference on Inorganic Scintillators and Their Applications*, Ed. V. Mikhailin, Moscow State University (2000) 206.
2. X.D.Qu *et al.*, *A Study on Sb Doping in Lead Tungstate Crystals*, to be published in *Nucl. Instr. and Meth.*
3. X.D.Qu *et al.*, *Radiation Induced Color Centers in Lead Tungstate Crystals*, accepted by *Journal of Inorganic Materials* (Chinese).
4. X.D.Qu *et al.*, *A Study on Y doping in Lead Tungstate Crystals*, to be submitted to *Nucl. Instr. and Meth.*
5. R.H.Mao, X.D.Qu *et al.*, *New Types of Lead Tungstate Crystals with High Light Yield* **Frascati Physics Series**, Vol.nnn (2001), pp.000-000, *IX Int. Conf. on Calorimetry in Part.Phys.*, Annecy, Oct. 9-14, 2000.